SMALL, DUAL BAND, PLACEMENT INSENSITIVE ANTENNAS

BY

JESSICA E. RUYLE

DISSERTATION

Submitted in partial fulfillment of the requirements
for the degree of Doctor of Philosophy in Electrical and Computer Engineering
in the Graduate College of the
University of Illinois at Urbana-Champaign, 2011

Urbana, Illinois

Doctoral Committee:

Professor Jennifer T. Bernhard, Chair
Professor Andreas C. Cangellaris
Professor Steven J. Franke
Professor Erhan Kudeki

ABSTRACT

RFID systems with "peel-and-stick" labels are currently limited to tracking items with nearly electromagnetically transparent material properties. This limitation stems from the antenna choice for these labels - a dipole variant. The slot antenna, the effective inverse of the dipole, is shown to be an effective RFID antenna for environment-independent peel-and-stick applications. A miniaturization and multi-band design technique is shown for a placement insensitive RFID antenna. With the significant advance in functionality over existing RFID antennas that is demonstrated by the antenna discussed in this dissertation, the purview of peel-and-stick RFID systems can expand to track all object types (metal, liquid, etc.), overcoming a fundamental limitation in current RFID deployments.

A traditional straight half-wavelength slot antenna would be too large for an RFID antenna at commonly used RFID frequencies. We investigate loading the slot antenna to reduce its size. By end-loading the slot, the total size of the slot can be greatly reduced. If the slot antenna is correctly loaded for a particular frequency, the input impedance seen at the feed point is the same for the full-sized or loaded slot. If an effective length of less than a half-wavelength is desired for the slot, the loads should be inductive. A slotline inductor provides an easily integratable inductance for the slot antenna and is used for the present antenna design. Loading the slot with a slotline inductor also provides the ability to make the antenna multi-band since the impedance of the inductor changes with frequency.

To ensure that the performance of the miniaturized slot antenna is independent of the material to which it is attached, a reflecting plane is added to

the design. However, slot antennas with closely spaced reflectors often couple energy into a parallel plate mode between the ground plane and the reflecting plane. The parallel plate becomes a cavity with the walls appearing as reactive loads to the slot antenna. In this work, we show that edge serrations can reduce the cavity effect in a parallel plate configuration, making a slot antenna with edge treatments a viable design for environment-independent peel-and-stick applications.

For this research to be broadly applicable, transmission line models are pursued to aid in the design process. Transmission line models for a rectangular and circular slotline inductor are presented as well as a model describing edge serrations on the ground plane in a parallel plate configuration. Each of these models is useful in and of itself, and they are combined in this research to present a design methodology for placement insensitive peel-and-stick RFID antennas. This methodology is used for the design of an antenna with a "peel-and-stick" form factor, and the antenna is shown through measurements to be placement insensitive - displaying no observable change in input impedance for different backing objects. With the discussed design methodology, different antennas can be designed for many different frequency bands and applications within RFID and any other application that requires an antenna that fits within a thin form-factor.

TABLE OF CONTENTS

CHAPTER 1

INTRODUCTION

1.1 Motivation for Investigation of Placement Insensitive RFID Antennas

Most RFID antennas are "dipole-like" meander lines, loops, or folded dipoles. These antennas perform poorly near ground planes or any material that is not electromagnetically transparent [1, 2]. The authors in [2] measured a quantity that they define as the "gain penalty" when standard RFID antennas were attached to various materials. The average "gain penalty" (defined as the decrease in RF tag antenna gain from its free space value when attached to a material) was greater than 10 dB when multiple RFID antennas were attached to an aluminum slab. For RFID systems, where the radius of operation is small, 10 dB of "gain penalty" renders the system unusable.

Figure 1.1 shows the explanation of why wire antennas near a ground plane perform so poorly. The figure shows how the effects of a ground plane can be approximated by placing a second horizontal electric current in the opposite direction of the driven element below the ground plane at the same distance from the ground plane. As the driven element moves closer to the ground plane, the image current moves closer to the driven element. Since the image current is in the opposite direction as the driven element, these currents cancel as the distance above the ground plane becomes small. The authors in [3] investigated this effect by studying the radiation efficiency of a straight-wire copper dipole above a ground plane. The results of their study are shown in Figure 1.2. As can be seen in the figure, for the thickness required for a

peel-and-stick antenna, the behavior of wire antennas in unacceptably poor.

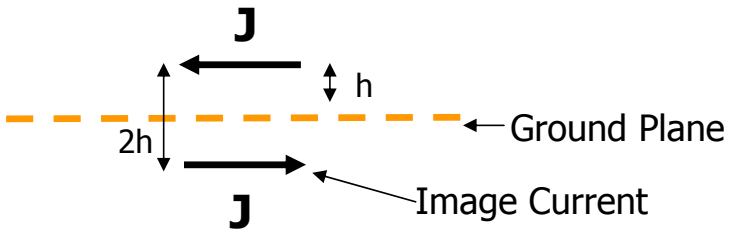

Figure 1.1: The effects of the placement of an electric current parallel to a ground plane through image theory.

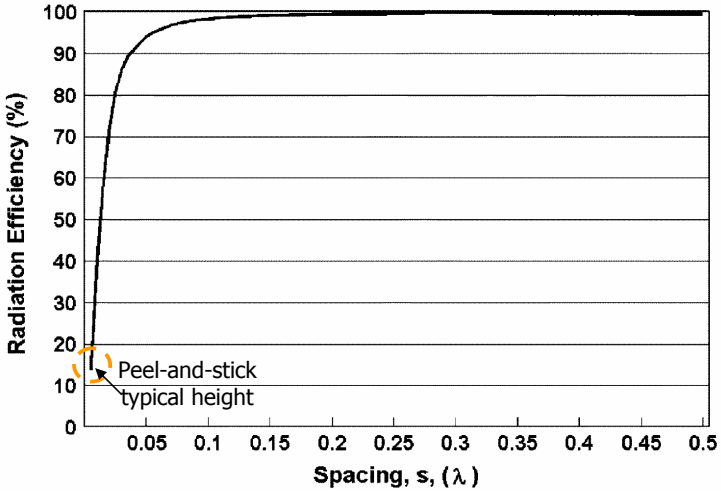

Figure 1.2: Radiation efficiency of a straight-wire copper dipole as a function of spacing above a PEC ground plane [3].

As discussed earlier, the impedance and gain of a straight wire antenna decrease drastically when the wire antenna is placed over a ground plane. The graph in Figure 1.3 shows how these behavior changes would affect the performance of the RFID system if a wire antenna were used as a tag antenna. The graph shows the power received in a monostatic radar system in which the radar cross section of the antenna is approximated as

$$\sigma = \frac{G_{tag}^2 \lambda_0 (1 - |\Gamma|^2)^2}{4\pi} \tag{1.1}$$

which is similar to the expression in [2] where G_{tag} is the gain of the tag antenna, λ_0 is the operating wavelength, and $|\Gamma|$ is the magnitude of the voltage reflection coefficient between the RFID chip and tag antenna. For the graph, the radius of operation was assumed to be 40 m, the power transmitted by the reader was 1 W, the operating frequency was 433 MHz, and the reader antenna was assumed to be a dipole with a gain of 2.15 dBi. As can be seen in the figure, a 10 dB "gain penalty" results in a 20 dB loss in received power at the reader assuming no change in impedance behavior for the tag antenna. Therefore, given the use of a wire antenna for the tag and both metal and non-metal objects to be tagged, when the inevitable impedance changes of the tag antenna are accounted for, there could be an approximately 60 dB dynamic range for the received power for an RFID system.

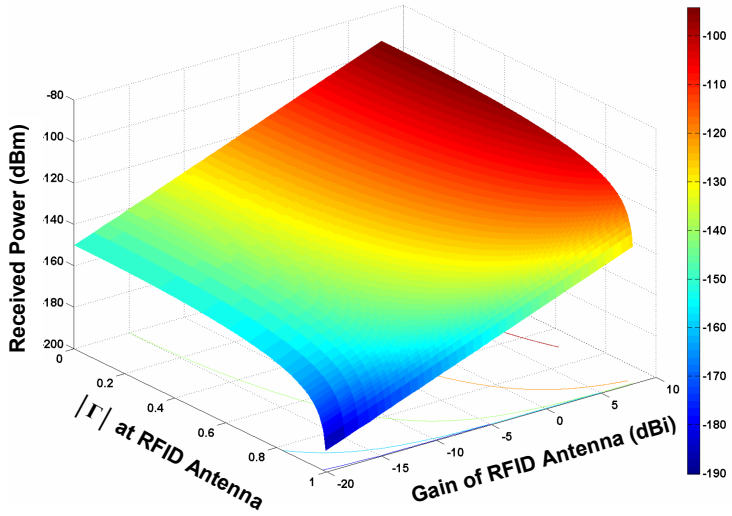

Figure 1.3: Graph showing received power for a monostatic radar system in which the radar cross section is characterized as in [2]. The radius of operation was assumed to be 40 m, the power transmitted was 1 W, the frequency of operation was 433 MHz, and a dipole antenna was assumed for the reader with a gain of 2.15 dBi.

While there are RFID antennas designed to be attached to metallic objects [4, 5], these antennas are generally complicated, difficult to manufacture, and bulky compared to the traditional "peel-and-stick" antennas used in RFID.

The antennas described in [4, 5] are shown in Figure 1.4. As can be seen in the figure, both antennas have a height of 3 mm and the antenna shown in Figure 1.4(b) is very complicated to manufacture. Peel-and-stick antennas generally have a form-factor with a thickness of less than a millimeter.

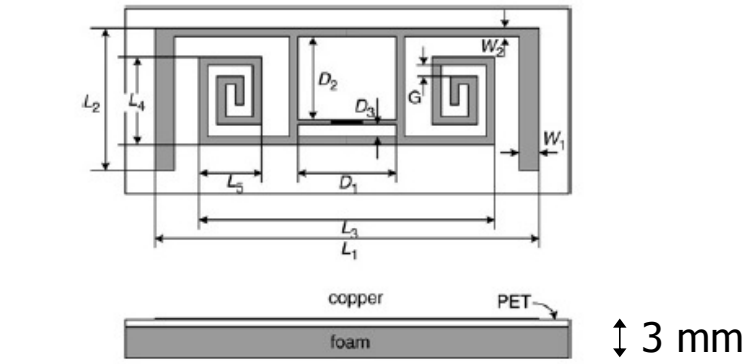

(a)

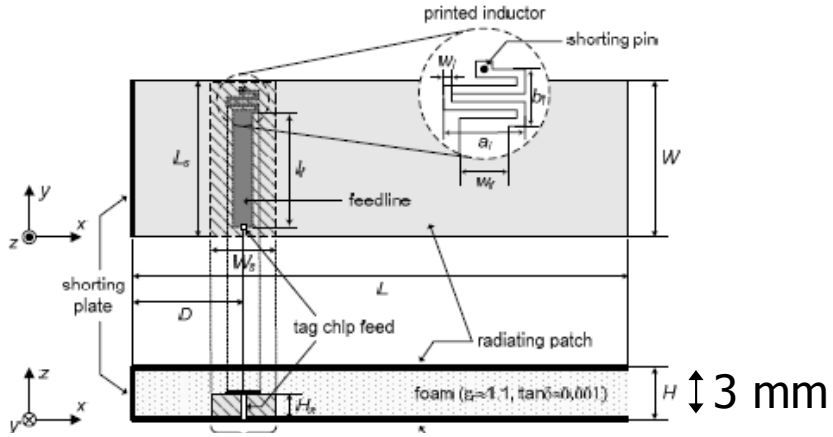

(b)

Figure 1.4: Depiction of two RFID antennas designed to be attached to metallic objects from the papers (a) [4] and (b)[5]. Both antennas have a height of 3 mm.

The present work details the investigation of the slot antenna, the inverse of the dipole, as a viable alternative for "peel-and-stick" RFID systems for non-electromagnetically transparent objects. Dual or multi-band operation is possible with the pursued antenna structure so that a final design will provide a flexible sensing option in a range of application areas. The present work

focuses on the development of a design model that can be used to enable both single and dual-band behavior.

1.2 Dissertation Outline

Chapter 2 discusses parametric studies that were performed to probe the general behavior of slot antennas. Chapter 3 details an investigation into the effectiveness of serrations as an edge treatment to reduce the cavity effect in parallel plate configurations. The dissertation continues with a derivation of the transmission line model for the slot antenna in Chapter 4 and a generalization of this model for higher order modes in Chapter 5. For the design of the miniaturized antenna, transmission line models of rectangular and circular spiral slotline inductors were derived. These models are discussed in Chapters 6 and 7, respectively. All of the components of the miniaturized and dual-band RFID antenna are incorporated into an antenna design and are discussed in Chapters 8 and 9. The antenna discussed in Chapter 8 is shown to be truly placement insensitive, with no observable change in input impedance with altered backplane environment. Finally, conclusions about the work and plans for future work are discussed in Chapter 10.

CHAPTER 2

PRELIMINARY INVESTIGATION OF RADIATING SLOTS

2.1 Introduction

As a preliminary investigation, many parametric studies were undertaken in order to supplement theoretical treatments and acquire fundamental knowledge about how slot antennas function with and without a backing ground plane. The studies were performed in HFSS [6]. The slot antenna used for these studies was a simple rectangular slot. Two depictions of the slot antenna simulated are shown in Figure 2.1. Figure 2.1(a) shows a top view of the slot antenna. The dimensions of the slot and ground plane will be given for each parametric study. The blue box indicates the lumped port used to feed the antenna in HFSS. Figure 2.1(b) shows an isometric view of the slot antenna. The presence of the second ground plane, a reflecting plane, depicted in Figure 2.1(b), was a variable for the parametric studies. It will be stated for each study whether or not it was included.

2.2 Parametric Studies

The first parametric study undertaken varied the feed point on a $\lambda/2$ slot (at 800 MHz) without a reflecting plane underneath. For this study, the dimensions of the slot were as follows: $L_{gp} = 440$ mm, $W_{gp} = 300$ mm, $w_s = 6$ mm, $L = 175$ mm. C is the feed-point offset and was varied from 0 to 87.5 mm. The results of this study are shown in Figure 2.2. As one would expect, the impedance shrinks as the feed point is moved from the center to the edge

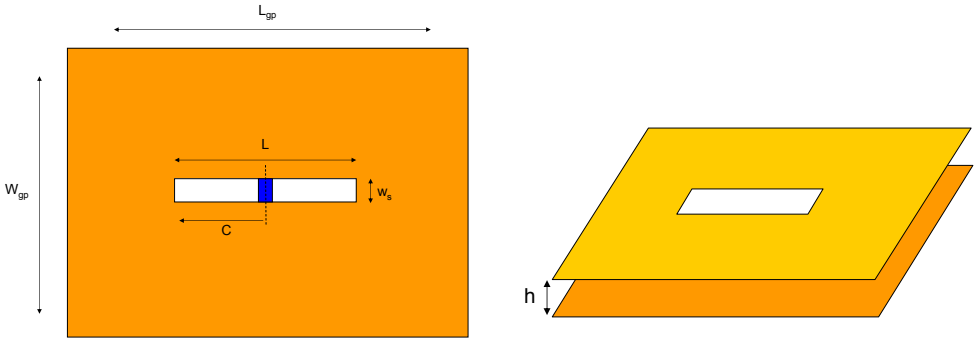

(a) (b)

Figure 2.1: Two depictions of simulated slot antenna, including (a) Top view of slot antenna, (b) Side view of slot antenna with depiction of optional reflecting plane.

(theoretical short) since the first mode of the slot is excited. The first mode has a co-sinusoidal electric field distribution with a maximum at the center of the slot and equal to zero at the edges.

The next parametric study undertaken varied the length of the slot, again without a ground plane. For this study the dimensions of the slot were as follows: $L_{gp} = 440$ mm, $W_{gp} = 300$ mm, $w_s = 6$ mm, and $C = 0$. L was varied from 40 mm to 175 mm. The results of this study are shown in Figure 2.3. As expected, the resonance shifts downward with increasing length of the slot.

The next parametric study undertaken varied the distance between the slot antenna and a second ground plane placed underneath this antenna. For this study the dimensions of the slot were as follows: $L_{gp} = 440$ mm, $W_{gp} = 300$ mm, $w_s = 6$ mm, $L = 175$ mm, and $C = 0$. The distance between the ground plane and reflecting plane, h, was varied from 1 mm to 59 mm. The results of this study are shown in Figure 2.4. Interestingly, the reflecting plane does not drastically affect the impedance seen at the feed point. The smallest impedance seen at the feed point, for the heights studied, results when the ground plane is 1 mm from the slot antenna. This 1 mm distance still results in a real part of the impedance on the order of 100 Ω.

The next parametric study undertaken varied the length of the slot when

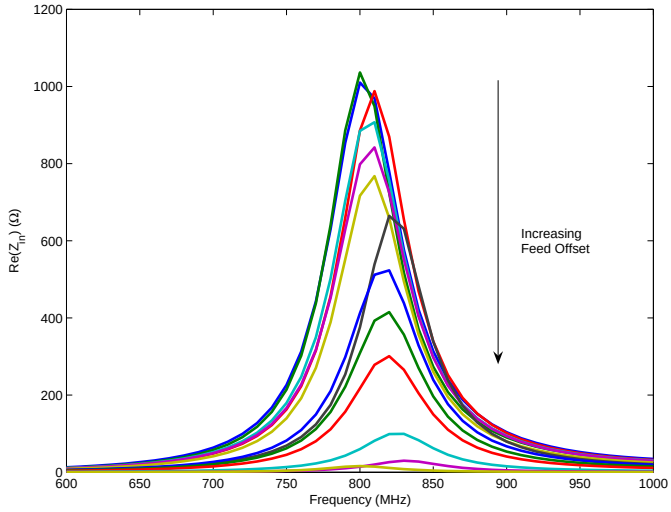

(a)

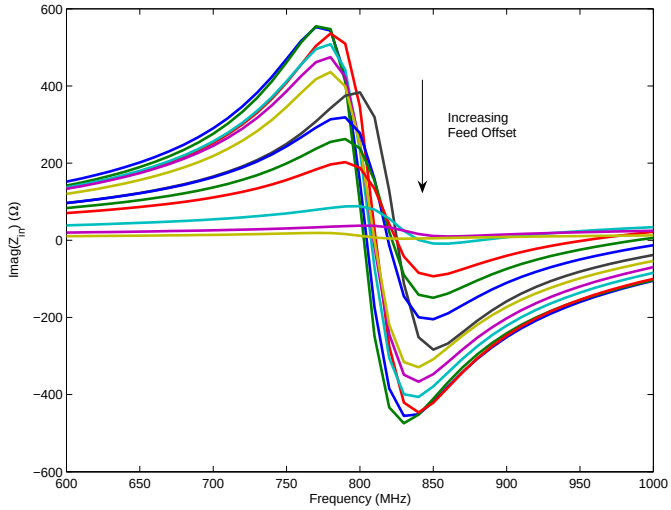

(b)

Figure 2.2: Input impedance for changing feed point: (a) Real part of input impedance, (b) Imaginary part of input impedance. For this study the dimensions of the slot were as follows: $L_{gp} = 440$ mm, $W_{gp} = 300$ mm, $w_s = 6$ mm, $L = 175$ mm. C is the feed-point offset and was varied from 0 to 87.5 mm. The results of this study are shown in Figure 2.2. As expected, the impedance shrinks as the feed point is moved from the center to the edge (theoretical short).

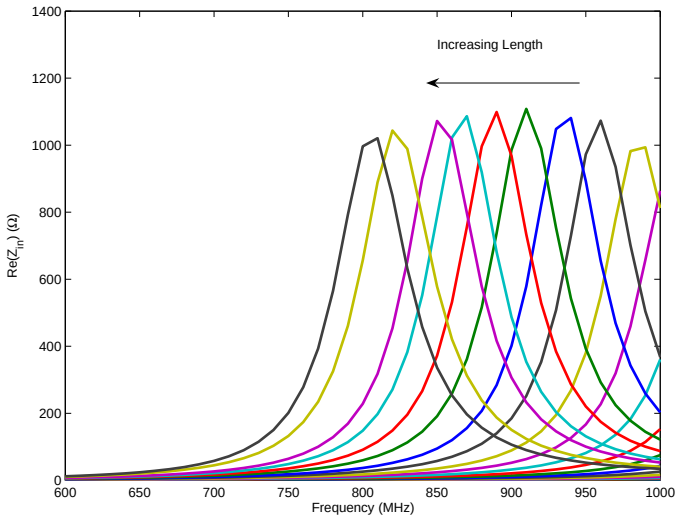

(a)

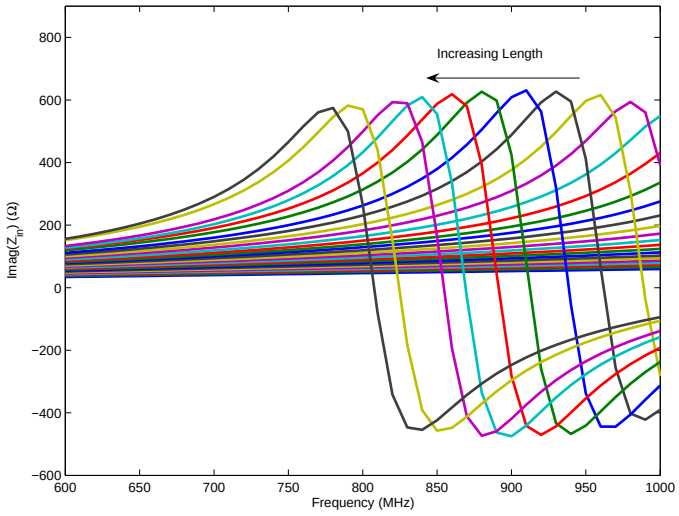

(b)

Figure 2.3: Input impedance for changing length of slot: (a) Real part of input impedance, (b) Imaginary part of input impedance. For this study the dimensions of the slot were as follows: $L_{gp} = 440$ mm, $W_{gp} = 300$ mm, $w_s = 6$ mm, and $C = 0$. L was varied from 40 mm to 175 mm. The resonance shifts downward with an increasing length of the slot.

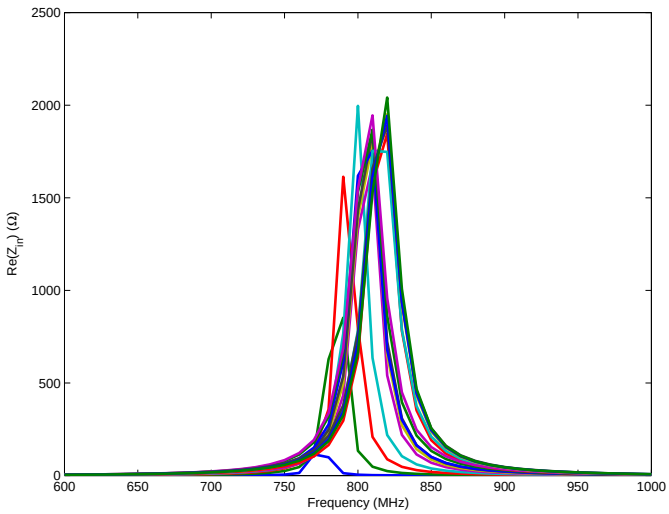

(a)

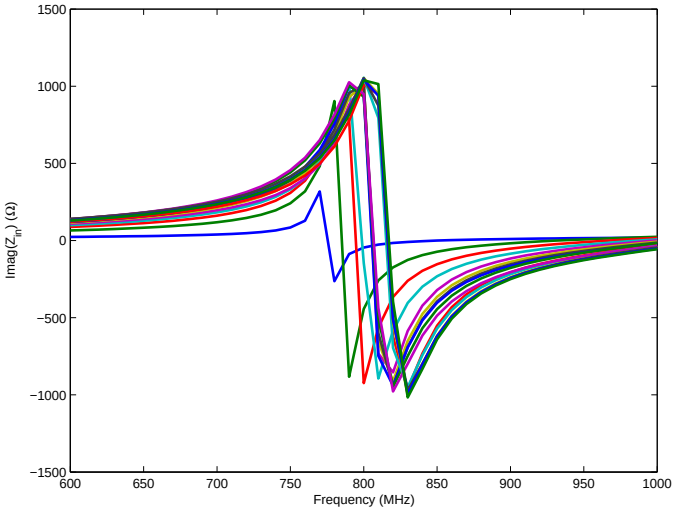

(b)

Figure 2.4: Input impedance for changing distance between reflecting plane and slot antenna: (a) Real part of input impedance, (b) Imaginary part of input impedance. For this study the dimensions of the slot were as follows: $L_{gp} = 440$ mm, $W_{gp} = 300$ mm, $w_s = 6$ mm, $L = 175$ mm, and $C = 0$. The distance between the ground and reflecting planes, h, was varied from 1 mm to 59 mm. The reflecting plane does not drastically affect the impedance seen at the feed point for any of the separations except for the smallest plate separation of 1 mm.

the reflecting plane underneath the slot antenna was included. For this study the dimensions of the slot antenna were as follows: $L_{gp} = 440$ mm, $W_{gp} = 300$ mm, $w_s = 6$ mm, $h = 1$ mm, and $C = 0$. The length of the slot was varied from 10 mm to 175 mm. The results of this study are shown in Figure 2.5. As before, the resonance shifts downward with increasing length. The length of 175 mm results in a resonance at a slightly lower frequency than without the reflecting plane. The reflecting plane adds a capacitance and thus shifts the resonance down in frequency. The bandwidth of the slot antenna is also reduced when the reflecting plane is included. The diagram in Figure 2.6 explains why the bandwidth is reduced. When an antenna is placed in the presence of a reflecting plane, it couples to the image antenna that is created by the reflecting plane. This image antenna has the same input impedance as the driven antenna since it has the same current magnitude; however, it reflects all incident power since it is not terminated in a load and is left open, giving a reflection coefficient of +1. The resulting reflection seen at the terminals of the driven antenna will then be

$$\Gamma_{in} = \Gamma_A + \frac{C_{Coupling}^2}{1 - \Gamma_A} \tag{2.1}$$

where Γ_A is the reflection coeffecient at the terminals of the antenna in isolation and $C_{Coupling}$ is the coupling coefficient between the antenna and its image. The formula in Equation 2.1 can be found by applying Mason's gain rule to the signal flow graph shown in Figure 2.4. The formula shown in Equation 2.1 results in a greater reflection seen at the input terminals of the driven antenna when it is placed in the presence of a reflecting plane.

The next parametric study undertaken varied the feed point of the slot antenna without a ground plane underneath when the antenna was electrically small. For this study the dimensions of the slot antenna were as follows: $L_{gp} = 440$ mm, $W_{gp} = 300$ mm, $w_s = 6$ mm, and $L = 17.5$ mm. C, the feed-point offset, was varied from 0 mm to 7 mm. The results of this study are shown in Figure 2.7. The real part of the impedance is small. The imaginary part of the impedance is not negligible; however, it should be noted that the

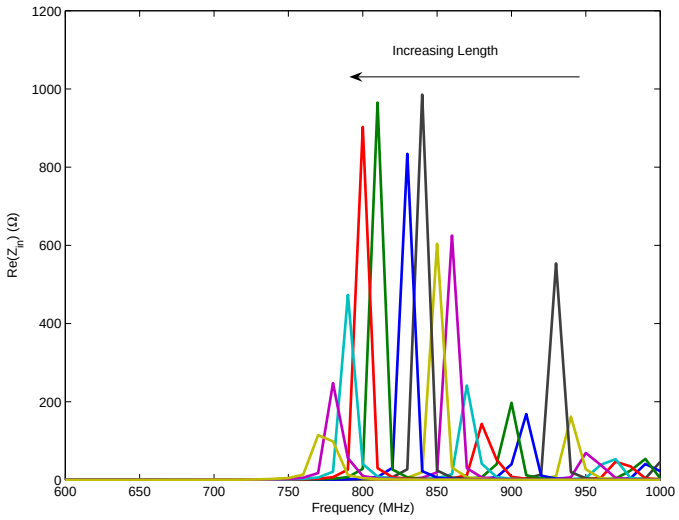

(a)

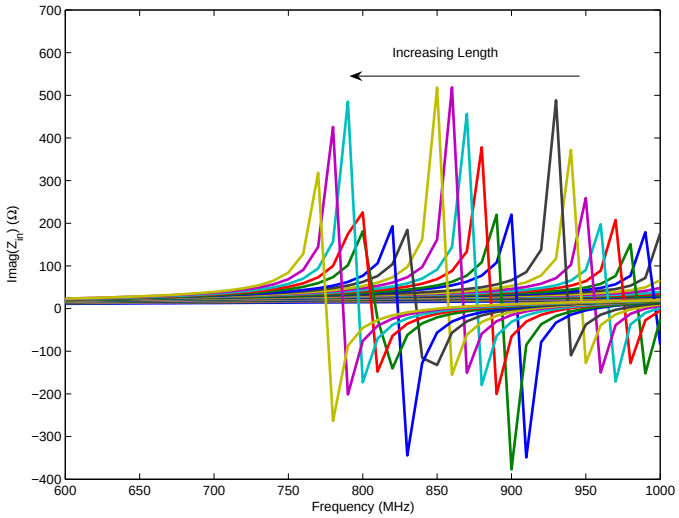

(b)

Figure 2.5: Input impedance for changing length of slot when ground plane exists behind slot antenna: (a) Real part of input impedance, (b) Imaginary part of input impedance. For this study the dimensions of the slot antenna were as follows: $L_{gp} = 440$ mm, $W_{gp} = 300$ mm, $w_s = 6$ mm, $h = 1$ mm, and $C = 0$. The length of the slot was varied from 10 mm to 175 mm. The resonance shifts downward with increasing length.

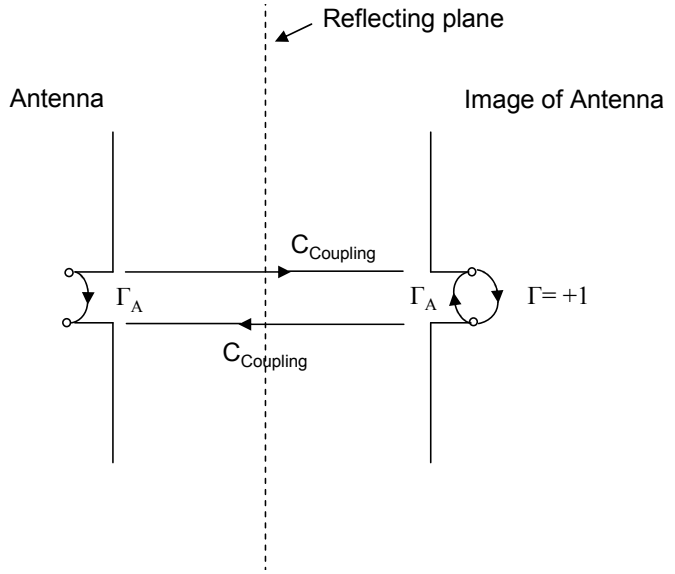

Figure 2.6: Depiction of an antenna above a reflecting plane with a simplified signal flow graph to explain the reduced bandwidth observed when a reflecting plane is included in the system.

reactance decreases when the feed-point offset is increased. This behavior presents tuning opportunities.

The next parametric study undertaken was to repeat the previous study (varying the feed point of the slot antenna when the antenna was electrically small) with a reflecting plane underneath the slot antenna. For this study the dimensions of the slot antenna were as follows: $L_{gp} = 440$ mm, $W_{gp} = 300$ mm, $w_s = 6$ mm, $h = 1$ mm, and $L = 17.5$ mm. OS, the feed-point offset, was varied from 0 mm to 7 mm. The results of this study are shown in Figure 2.8. Unfortunately, the real part of the impedance is still small. It is expected that the impedance will be much larger when the slot antenna is serpentined or resonated. The imaginary part of the impedance is lower when the ground plane is included. This is likely due to the added capacitance between the ground plane and the reflecting plane, canceling out a portion of the inductive reactance of the slot antenna. This phenomenon also presents tuning opportunities.

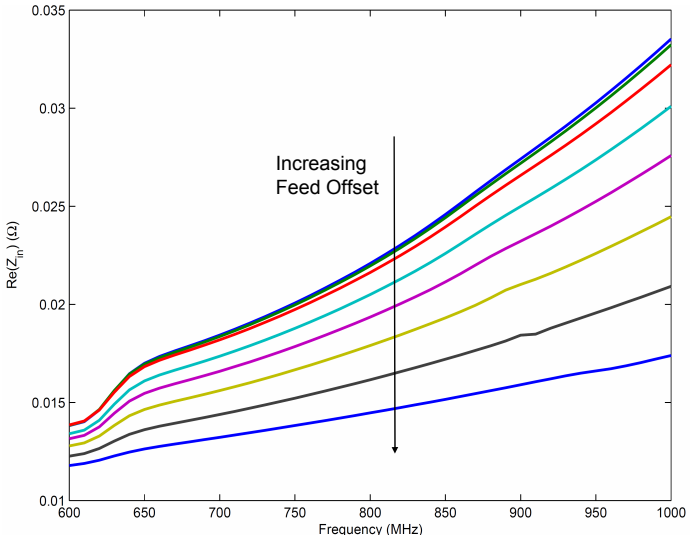

(a)

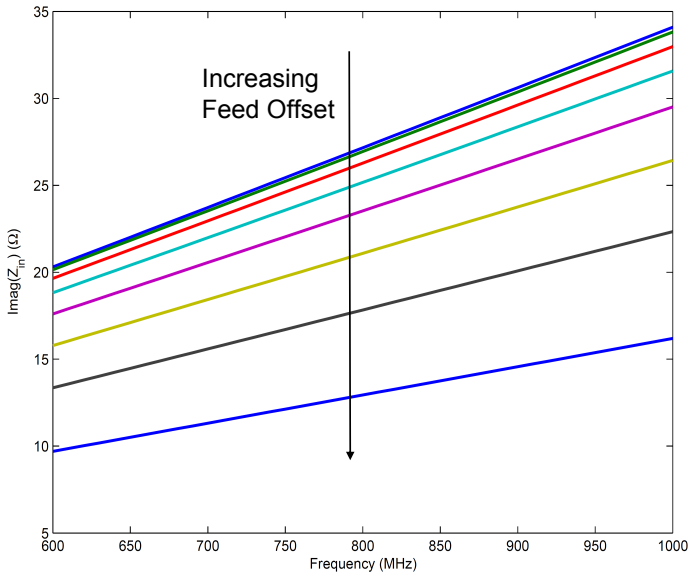

(b)

Figure 2.7: Input impedance for changing feed point when slot antenna is electrically small ($\frac{\lambda}{10}$ at 800 MHz): (a) Real part of input impedance, (b) Imaginary part of input impedance. For this study the dimensions of the slot antenna were as follows: $L_{gp} = 440$ mm, $W_{gp} = 300$ mm, $w_s = 6$ mm, and $L = 17.5$ mm. OS was varied from 0 mm to 7 mm.

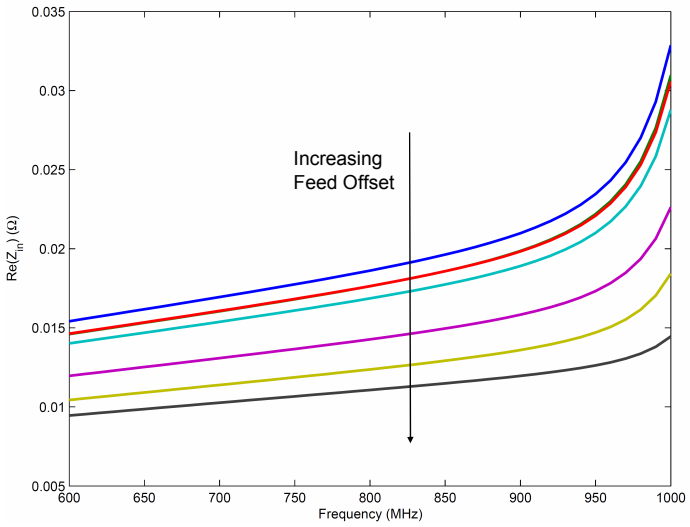

(a)

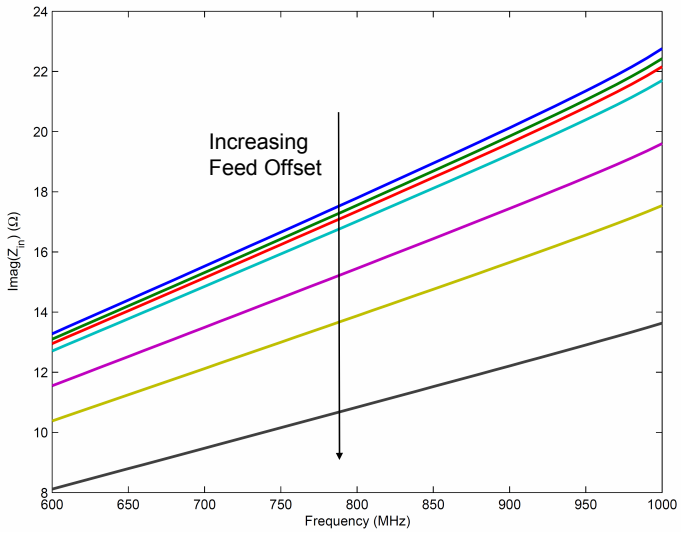

(b)

Figure 2.8: Input impedance for changing feed point when slot antenna is electrically small ($\frac{\lambda}{10}$ at 800 MHz) with ground plane underneath slot antenna: (a) Real part of input impedance, (b) Imaginary part of input impedance. For this study the dimensions of the slot antenna were as follows: $L_{gp} = 440$ mm, $W_{gp} = 300$ mm, $w_s = 6$ mm, $h = 1$ mm, and $L = 17.5$ mm. OS was varied from 0 mm to 7 mm. The real part of the impedance is still small. It is expected that the impedance will be much larger when the slot antenna is serpentined or resonated.

2.3 Conclusions

The parametric studies provided insight into the behavior of slot antennas. They were shown to behave in a predictable manner and should be able to be modeled effectively. The magnitude of the input impedance shrinks as the feed point is shifted off-center and the resonant frequency decreases as the length of the slot increases. The addition of a reflecting plane to the slot antenna reduces the bandwidth of the antenna but does not greatly shift the resonant frequency. When the slot antenna has a reflecting plane and the length of the slot is increased, the resonant frequency still decreases as expected. When a slot antenna is electrically small, the magnitude of the impedance is still small and the reactance is positive. Also, when a reflecting plane is added to an electrically small slot antenna, the magnitude of the real part of the impedance is still small but the reactive part of the impedance decreases toward zero with the addition of the reflecting plane. This is likely due to the added capacitance between the ground and reflecting plane. These results present unique tuning opportunities.

CHAPTER 3

GROUND PLANE SERRATIONS

3.1 Introduction

Serrated and rolled edges have long been used in parabolic dish antennas to reduce diffraction due to the abrupt end of the reflector antenna [7]. Ground plane serrations were used in [8] to improve the performance of microstrip patch antennas on finite ground planes. The design goal behind the serrations in both of these instances is to make the ground plane or reflector look infinite.

A slot antenna over a reflecting plane can excite a parallel plate mode in between the ground and reflecting planes. Serrations on the edge of the ground plane, in the case of the slot antenna over a reflecting plane, can reduce reflections at the termination of the parallel plate. This reduced reflection diminishes the cavity effect of the parallel plate on the slot antenna, thus reducing the reactive loads that the edges of the parallel plate can present at the input of the slot.

The effect of serrating the edge of a parallel plate configuration was investigated in simulation as shown in Figure 3.1. A parallel plate that was longer than two wavelengths for the entire frequency band of interest was analyzed in HFSS. A waveport with the dimensions of the parallel plate was used as an excitation and impedance reference on one end of the parallel plate. The air box was a quarter wavelength away from all edges. Serrations were only added to the top plate in the configuration. After the serrations were analyzed in HFSS, a transmission line model was derived that describes the behavior of the serrations. The HFSS simulations are compared to the results from the transmission line model.

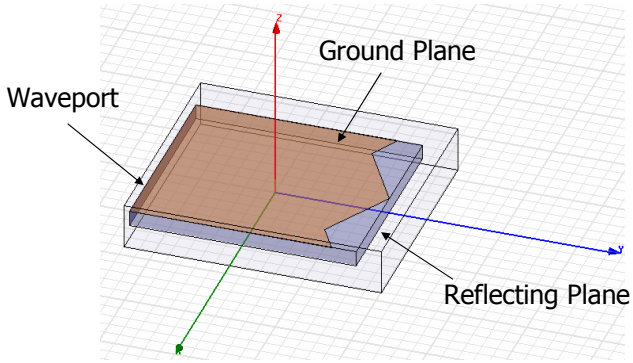

Figure 3.1: Simulation setup for serrated parallel plate waveguide.

3.2 Investigation of Behavior of Ground Plane Serrations

To start the study, a parallel plate configuration with no serrations was analyzed in HFSS. For this configuration the separation between the two parallel plates was varied from approximately 0.05λ to 0.6λ. The width and length of the plates analyzed were 4.4λ and 5.0λ, respectively, at the center frequency of the frequency band of interest. The results of this study are shown in Figure 3.2. The effect of the height on percent impedance bandwidth (VSWR<2) looking into the waveport is shown in the figure. When the height is less than a quarter of a wavelength, the impedance mismatch between free-space and the parallel plate waveguide becomes large. Therefore, most of the energy is trapped within the parallel plate waveguide.

The effect of the width of a triangular serration was investigated in simulation. The height of the separation between the two plates was set at 0.08λ and the depth of the serration was set at 0.9λ. The width of the serration was varied from approximately 0.2λ to 9λ. The effect of the width on the VSWR<2 impedance bandwidth is shown in Figure 3.3. It is clear in the figure that one width presents the broadest impedance bandwidth for the given height and depth.

The effect of the depth of a triangular serration on the VSWR<2 impedance bandwidth was investigated in simulation. The height of the separation be-

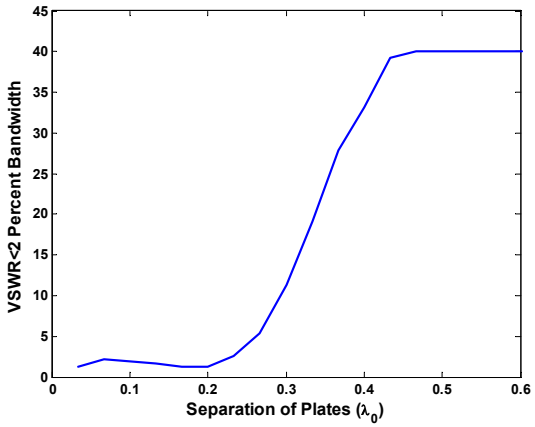

Figure 3.2: Results of parametric study of the effect of the separation between parallel plates on the percent bandwidth seen at a port looking into the parallel plate configuration.

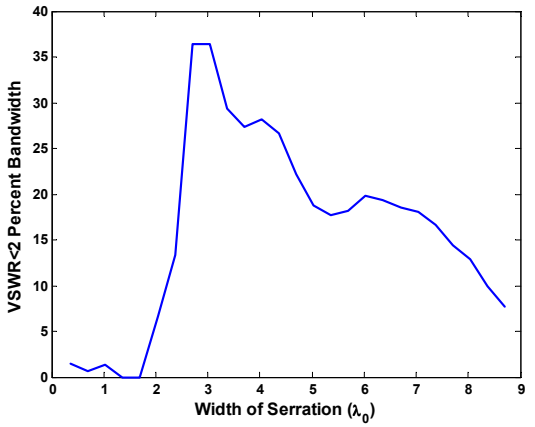

Figure 3.3: Results of parametric study of the effect of the width of serrations on the top plate on the percent bandwidth seen at a port looking into the parallel plate configuration for a plate separation of 0.08λ.

tween the two plates was set at 0.08λ. The study was conducted for two widths, 3λ and 2λ. The results of this study are shown in Figure 3.4. It is clear from the figure that for each width, there is a depth of serration that presents the best impedance bandwidth.

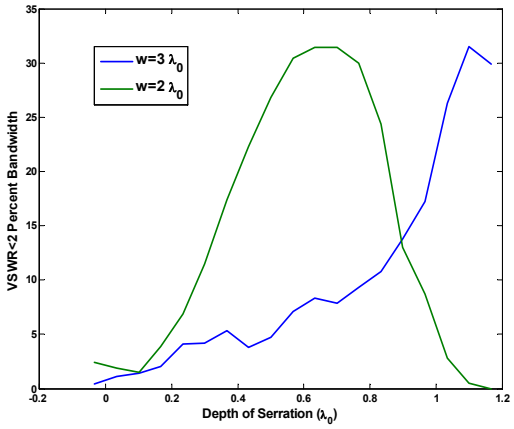

Figure 3.4: Results of parametric study of the effect of the depth of serrations on the top plate on the percent bandwidth seen at a port looking into the parallel plate configuration for a plate separation of 0.08λ.

To confirm that the serrations were providing an impedance match between free space and the parallel plate waveguide, the electric field was analyzed with and without serrations. A plot of the electric field magnitude with the corresponding VSWR plot for the parallel plate with and without serrations is shown in Figure 3.5. As can be seen in the figure, there is a clear standing wave without serrations. The standing wave is not present when the serrations are added to the top plate. The serration dimensions were w=2.5λ, d=0.74λ, and h=0.07λ.

The VSWR for the parallel plate configuration with and without serrations for an expanded frequency range is shown in Figure 3.6. The serrations significantly reduce the VSWR across the band, while without the serrations there is a clear standing wave.

The radiation properties of the serrations were investigated in simulation. The dominant polarization radiation patterns are shown in Figure 3.7 for the

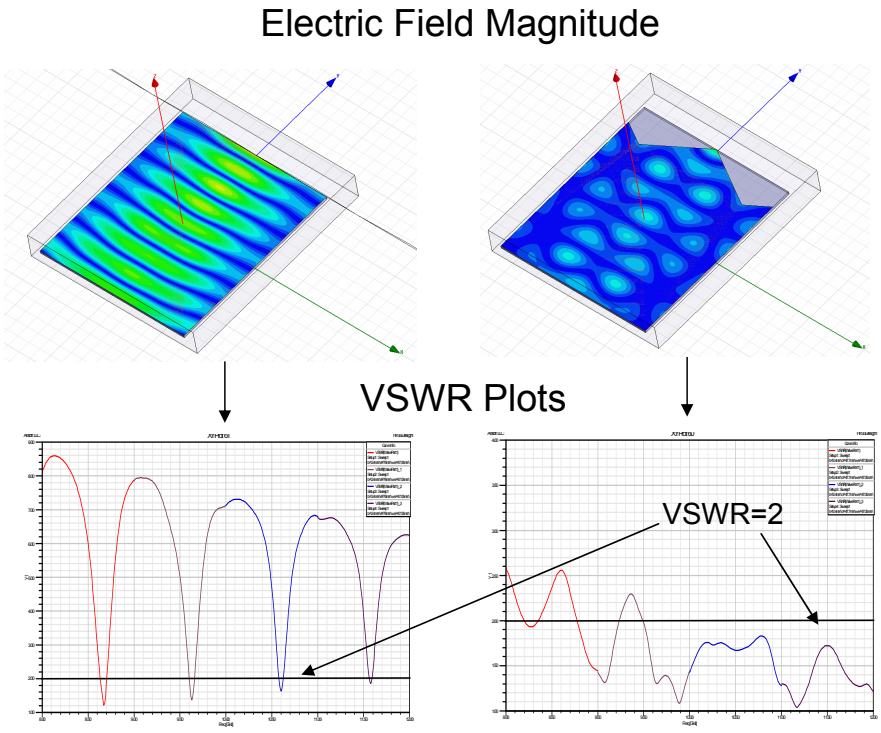

Figure 3.5: VSWR and electric field with and without serrations. The serration dimensions were w=2.5λ and d=0.74λ for a plate separation of h=0.07λ.

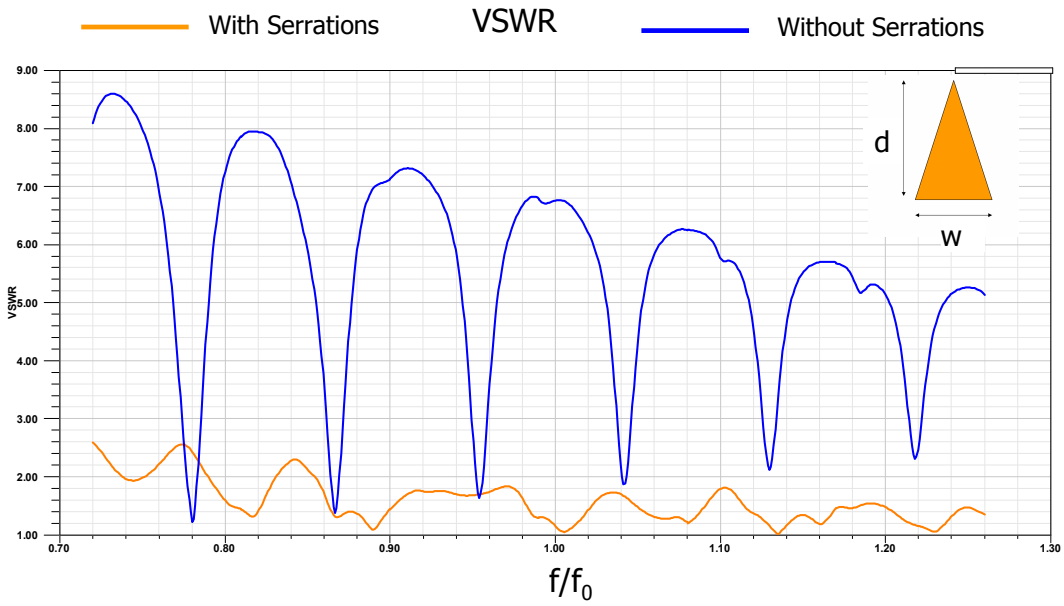

Figure 3.6: VSWR for expanded frequency range with and without serrations. The VSWR is plotted with and without serrations versus the frequency of operation over the center frequency of the band. The serration dimensions were w=2.5λ and d=0.74λ for a plate separation of h=0.07λ.

plate orientation shown in Figure 3.5. Realized gain was used for the radiation patterns; therefore, the impedance mismatch was accounted for in the gain calculation. As can be seen in the figure, there is a significant gain advantage by adding the serrations. The serrations also reduce back-plane radiation. The radiation patterns were taken for serration dimensions of w=2.5λ, d=0.74λ, and h=0.07λ.

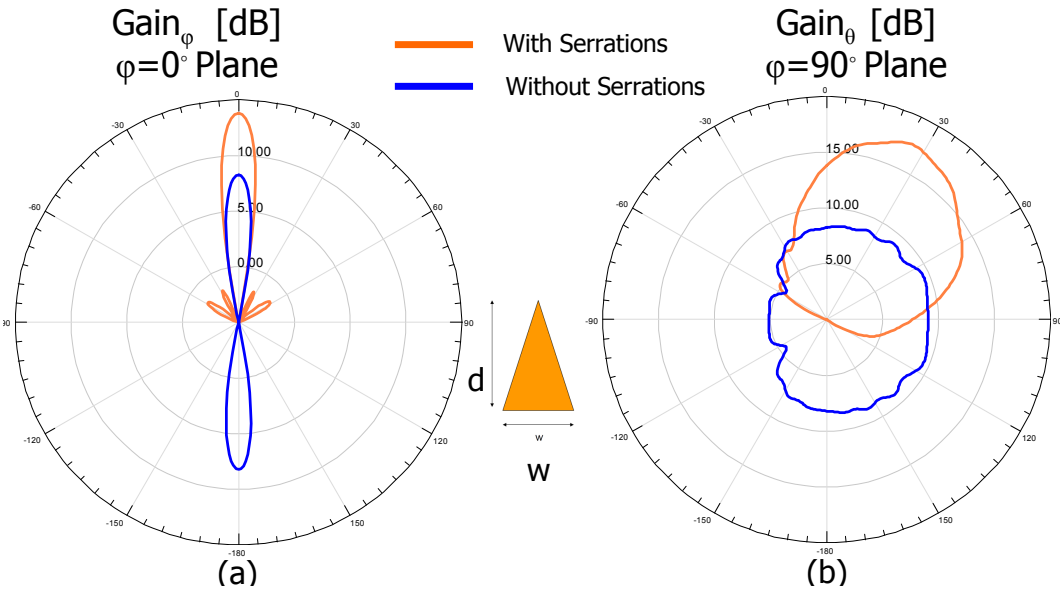

Figure 3.7: Co-polarized radiation patterns of parallel plate configuration with and without serrations: (a) Gain in the ϕ direction for the $\phi = 0$ plane, (b) Gain in the θ dimension for the $\phi = 90^0$ plane.

3.3 Transmission Line Model of Edge Serrations

While serrations have been used extensively in many applications, a model has never been developed that effectively describes their behavior. The serrations have largely been designed based on rules of thumb and general guidelines. The following is a proposed transmission line model to effectively describe the behavior of the serrations as terminations in a parallel plate configuration. The transmission line model provides an important step in the design process

between rules-of-thumb and full-wave simulations.

The transmission line model assumes that each serration is a separate transmission line attached to a single point on a parallel plate waveguide. The parallel plate waveguide is assumed to be thin enough that only the first mode (TEM) is propagating. This is a good assumption for heights less than half a wavelength [9].

Each section of the transmission line model is described in Figure 3.8. Each of the serrations can be described using a two-port ABCD matrix loaded with free space. The serrations are part (a) in the diagram. Part (b) in the diagram is the junction of the parallel plate waveguide and serrations. The parallel plate waveguide is simply a section of transmission line. This is labeled as part (c) in the diagram.

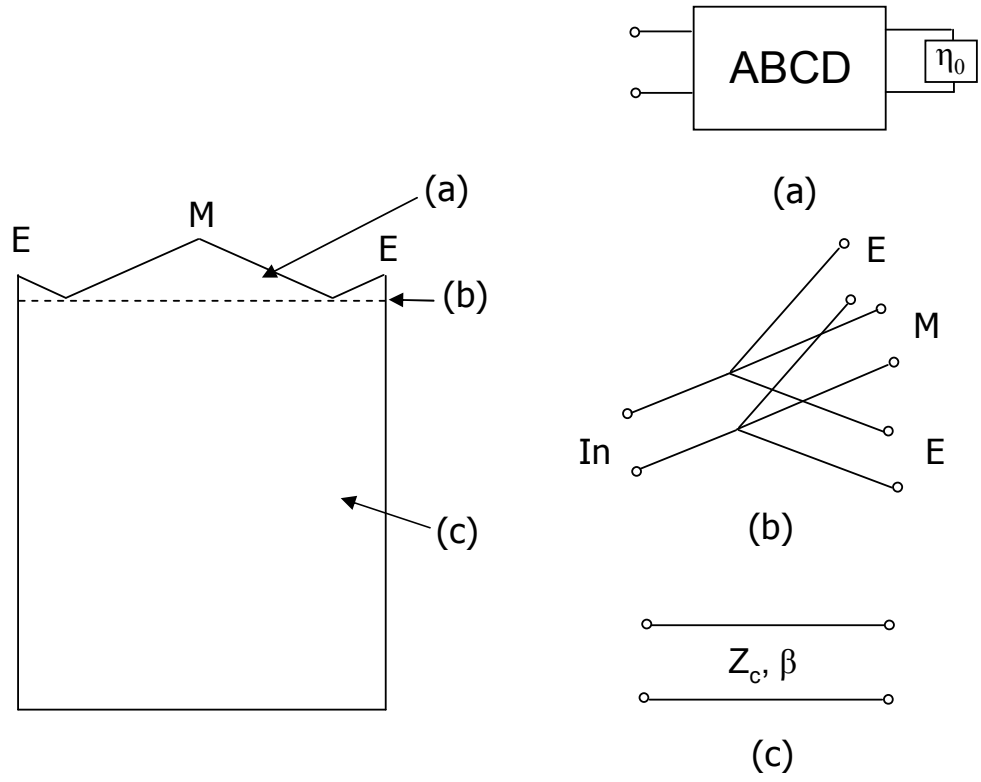

Figure 3.8: Top view of parallel plate with edge serrations with each piece of the transmission line model described.

The impedance of each serration is found by assuming it can be analyzed using a stair-step method as shown in Figure 3.9. The ABCD matrix for each section is found. Then, the ABCD matrices are multiplied in the appropriate order to find the total ABCD matrix for a serration.

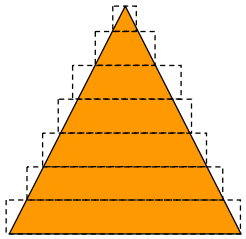

Figure 3.9: Depiction of one serration discretized in a stair step to calculate an approximate ABCD matrix describing the structure.

Once the ABCD matrix is found, the impedance of the serration can be determined using the standard equation shown in Equation 3.1 for input impedance, where η_0 is the impedance of free space and is the load impedance terminating the ABCD matrix that represents the serrations.

$$Z_{Load} = \frac{A\eta_0 + B}{C\eta_0 + D} \tag{3.1}$$

If it is assumed that the serrations are uniform and symmetric about the centerline of the parallel plate waveguide, then the impedance seen looking into the junction connecting the serrations to the parallel plate can be directly found based on a simple formula. According to the above assumptions, there will be N+2 serrations where

$$N = floor\left(\frac{W}{w_m}\right) \tag{3.2}$$

W is the width of the parallel plate waveguide, and w_m is the initial width of the serration. The floor function simply rounds the result of the fraction down to the nearest integer. There will be two serrations on the edges that will have widths less than the width of the middle serrations. This width of

the edge serrations, w_{me}, is described as

$$w_{me} = \frac{W - Nw_m}{2} \tag{3.3}$$

Once the ABCD matrices for the middle, Z_{Lm}, and edge serrations, Z_{Le}, are found, the impedance, Z_{Lserr}, looking into the serrations at the junction between the parallel plate and the serrations, denoted by the dotted line in Figure 3.8, can be found by

$$Z_{Lserr} = \frac{1}{\frac{2}{Z_{Le}} + \frac{N}{Z_{Lm}}} \tag{3.4}$$

which can be simplified to

$$Z_{Lserr} = \frac{Z_{Le}Z_{Lm}}{2Z_{Lm} + NZ_{Le}} \tag{3.5}$$

where Z_{Le} is the impedance of the edge serration and Z_{Lm} is the impedance of each middle serration.

The reflection at the junction between the parallel plate and the serrations, denoted by the dotted line in Figure 3.8, can be found as

$$\Gamma_{serr} = \frac{Z_{Lserr} - Z_c}{Z_{Lserr} + Z_c} \tag{3.6}$$

where

$$Z_c = \frac{\eta h}{w} \tag{3.7}$$

which is the characteristic impedance of a parallel plate waveguide in the TEM mode [9].

3.4 Results of Transmission Line Model of Edge Serrations

The impedance of the serrations found using the transmission line model and HFSS simulations are compared in Figure 3.10. The frequency band for which the serrations were analyzed encompasses traditional RFID frequencies. The width and length of the parallel plate waveguide studied were 300 and 600 mm, respectively. The depth of the serration, d, was 75.45 mm, the width of the serration, w, was 71.12 mm, and the plate separation distance, h, was 3 mm. As can be seen in the figure, the transmission line model captures the general outline of the effect of the serrations. However, there appear to be higher-order effects, likely from diffraction and radiation, that the transmission line model does not capture. However, the model works well for the purposes of design with an emphasis on the dominant lowest order modes.

3.5 Radial Ground Plane Serrations

Due to the circular shape of the Archimedean spiral slot structure discussed in Chapter 7, a radial edge treatment was investigated to determine its relative effectiveness at eliminating the parallel plate mode excited by the slot antenna in comparison to the edge treatment of the rectangular parallel plate waveguide. A transmission line model was also developed for this structure to aid in the design of the radial serrations. The transmission line model is detailed below along with its comparison to the predicted impedance by a full-wave solver and measured results. A radial parallel plate waveguide with edge serrations is depicted in Figure 3.11.

3.5.1 Transmission Line Model of Radial Serrations

The transmission line model for radial serrations uses the same method to find the impedance of an individual serration as was described earlier in the chap-

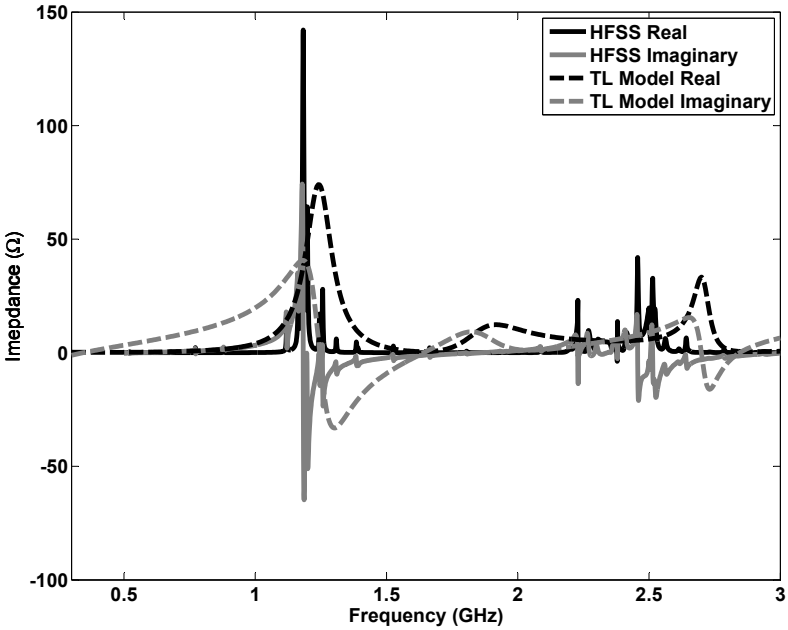

Figure 3.10: Results of the transmission line model compared with HFSS simulations. The real and imaginary parts of the impedance of the serrations are plotted. The impedance from HFSS is de-embedded to the plane where the serrations begin. The width and length of the parallel plate waveguide studied were 300 and 600 mm respectively. The depth of the serration, d, was 75.45 mm, the width of the serration, w, was 71.12 mm, and the plate separation, h, was 3 mm.

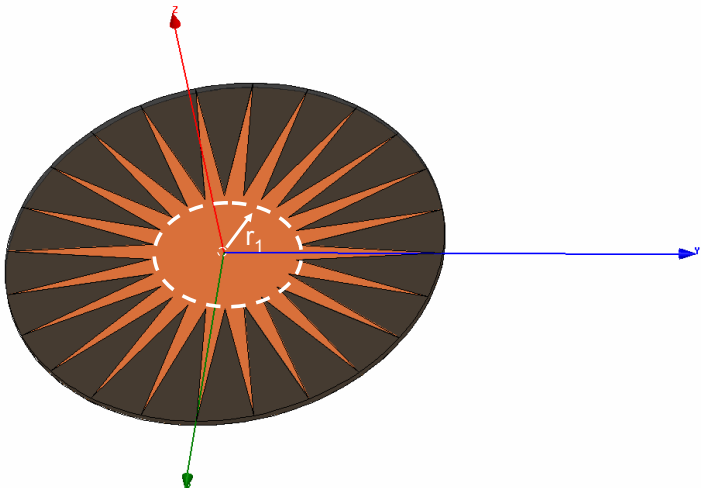

Figure 3.11: Depiction of radial serrations.

ter. The serration is analyzed in a stairstep fashion and an input impedance for each serration is found from the serration terminated in free space. The impedance at the radius of the parallel plate waveguide where the serrations begin (Z_{r1}) is then simply the impedance of all of the serrations in parallel. Explicitly,

$$Z_{r1} = \frac{Z_{serr}}{N} \tag{3.8}$$

where N is the number of serrations. To find the impedance of the serrated radial parallel plate waveguide, the admittance matrix found by the author in [10] and simplified by the authors in [11] can be used to deembed the impedance. An admittance matrix must be used instead of normal transmission line equations since the radial transmission line changes dimensions with increased radius. The admittance matrix used to determine the impedance at a central feed point is

$$Y_{11} = \frac{1}{jZ_1}\frac{H_1^2(kr_1)H_0^1(kr_2) - H_0^2(kr_2)H_1^1(kr_1)}{(H_0^2(kr_1)H_0^1(kr_2) - H_0^2(kr_2)H_0^1(kr_1)} \tag{3.9}$$

$$Y_{12} = \frac{1}{jZ_1}\frac{H_0^2(kr_1)H_1^1(kr_1) - H_1^2(kr_1)H_0^1(kr_1)}{(H_0^2(kr_1)H_0^1(kr_2) - H_0^2(kr_2)H_0^1(kr_1)} \tag{3.10}$$

$$Y_{21} = \frac{1}{jZ_2} \frac{H_0^2(kr_2)H_1^1(kr_2) - H_1^2(kr_2)H_0^1(kr_2)}{(H_0^2(kr_1)H_0^1(kr_2) - H_0^2(kr_2)H_0^1(kr_1)} \tag{3.11}$$

$$Y_{22} = \frac{1}{jZ_2} \frac{H_1^2(kr_2)H_0^1(kr_1) - H_0^2(kr_1)H_1^1(kr_2)}{(H_0^2(kr_1)H_0^1(kr_2) - H_0^2(kr_2)H_0^1(kr_1)} \tag{3.12}$$

where

$$Z_1 = \frac{\eta h}{2\pi r_1} \tag{3.13}$$

$$Z_2 = \frac{\eta h}{2\pi r_2} \tag{3.14}$$

and where r_1 and r_2 are the radii of the serrations and feed, respectively. The number of serrations is an integer and the width of the serration at r_1 is

$$W_{serr} = 2r_1 \sin\left(\frac{\pi}{N}\right) \tag{3.15}$$

A radial parallel plate waveguide with edge serrations was analyzed using both the transmission line model and HFSS simulations and the simulated structure was constructed and measured. The number of serrations was 24 and the depth of the serration was 68.8 mm (0.37λ at 1.6 GHz). The height of the substrate was 3.048 mm (0.02λ at 1.6 GHz) and the substrate material was RT Duroid 6002 with a relative permittivity of 2.94. The constructed structure was fed using a coaxial via feed at the center of the structure with the outer conductor of the coaxial line connected to the reflecting plane and the inner conductor extending through the substrate to connect to the ground plane. In the HFSS simulation the structure was fed using a small lumped port at the center of the structure. The simulated and measured results are shown in Figure 3.12. As can be seen in the figure, the transmission line model is significantly different from both the HFSS and measured results. More work should be pursued to better understand the bahavior of this structure.

The simulated radiation patterns for the radial serrations are shown in Figure 3.13. As can be seen in the figure, the radiation is θ directed in all elevation planes with a null at the feed. This implies that the radiation from the radial serration in this scenario is not from the ϕ-directed fringing fields of the serrations, as was observed with the serrations to the rectangular parallel plate

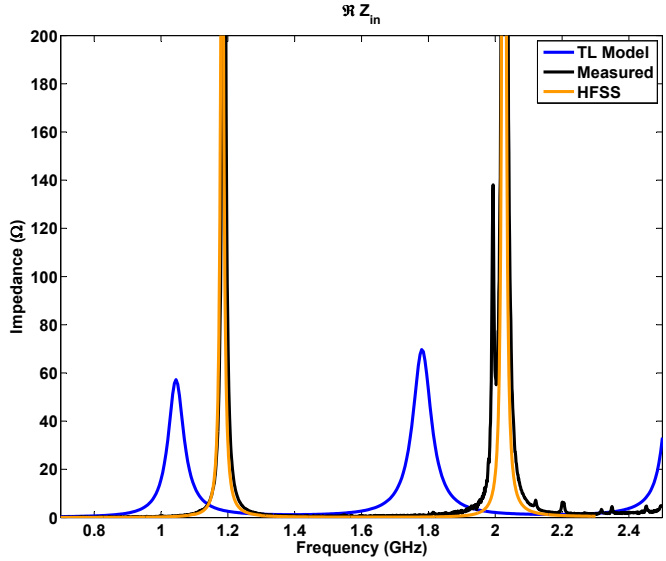

(a)

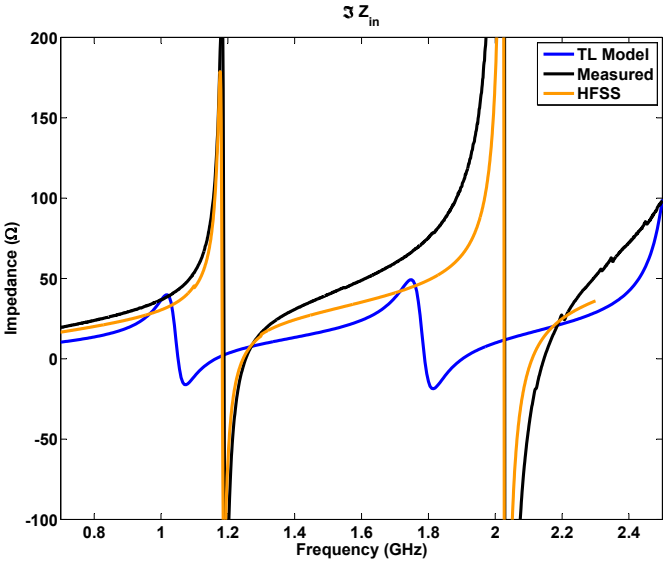

(b)

Figure 3.12: Impedance of serrated radial parallel plate waveguide with (a) Real and (b) Imaginary impedance for the transmission line model, HFSS simulation, and measured results.

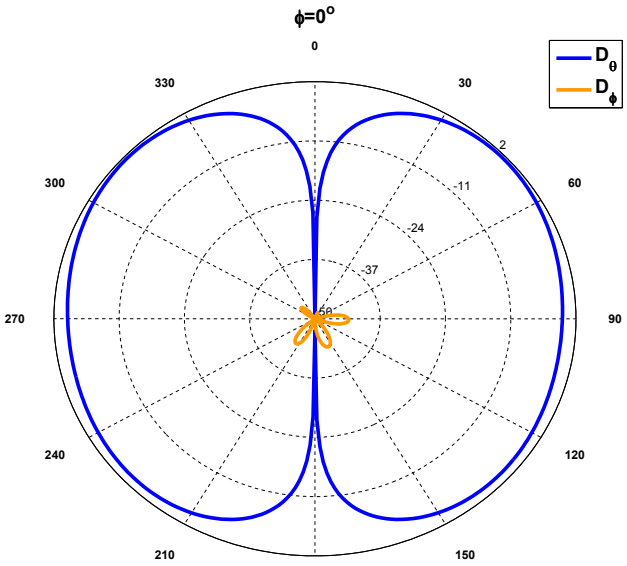

(a)

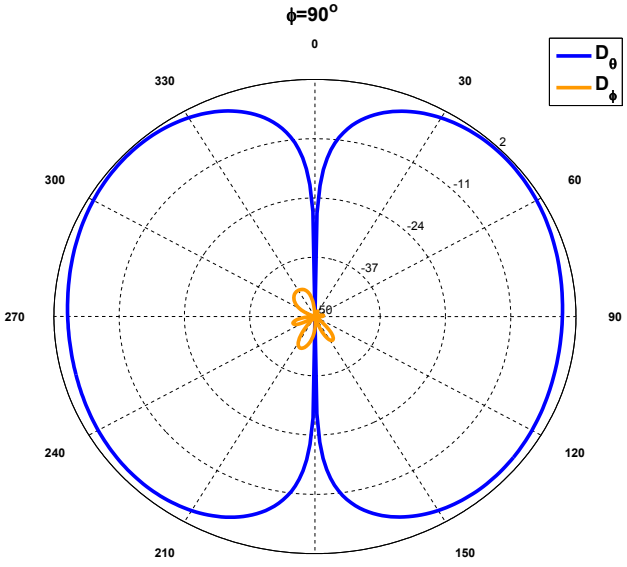

(b)

Figure 3.13: Simulated radiation patterns (displayed through directivity, D) of radial serrations at 1.2 GHz for (a) $\phi = 0$ plane, (b) $\phi = 90^o$ plane for the coordinate system that is shown in Figure 3.11.

waveguide in the last chapter. It is likely that the serrations are so close to each other electrically that the ϕ-directed fringing from each serration cancels with the fringing from the nearest serration that is oppositely directed, leaving only the radially directed fringing component. More work should be pursued toward a better understanding of the radiation mechanism for serrations and the effects of the radiation should be added to the transmission line model.

3.5.2 Radial Serrations Conclusions

A transmission line model for radial serrations was derived. It was found that the transmission line model is less accurate than that of the rectangular parallel plate waveguide and the radiation mechanism from the radial serrations is not fully understood. More work will be pursued in the future to fully understand this structure and its radiation mechanisms.

3.6 Conclusions

Ground plane edge serrations were shown to effectively reduce the cavity effect in parallel plate configurations. When added to a slot antenna with a reflecting plane, ground plane serrations should reduce the reactive loading typically observed at the feed point in that antenna configuration. By reducing the cavity effect through the use of serrations, the frequency shift typically observed when a reflecting plane is added behind a slot antenna can be minimized. A transmission line model for ground plane serrations was derived. This transmission line model is accurate enough to act as a first-order result to find appropriate serration dimensions before a final design can be determined using a full-wave solver. More work will be pursued in the future to add the radiation mechanism of the serrations to the transmission line model to increase the accuracy of the model.

CHAPTER 4

TRANSMISSION LINE MODEL OF SLOT ANTENNA

4.1 Introduction

A transmission line model for the slot antenna was pursued to aid in the design process of the antenna. With a transmission line model, the total time for the design process is shortened since the approximate dimensions for the antenna can be determined outside of a full-wave solver.

A previously derived transmission line model was found for a slot antenna that equates the power delivered to a lossy transmission line and the power radiated by a slot [12]. This model was originally derived by Himdi and Daniel in [12]. The model assumes that the slot antenna can be represented by two shorted lossy transmission lines in parallel, as shown in Figure 4.1. Using the field requirements from transmission line theory, the far-field expressions for the radiated electric field are analytically found. From these, the total power radiated is found in terms of the radiated loss per-unit-length (α). The value of α is found by equating the power delivered to and the power radiated by the slot. The derivation of all equations presented in [12] is shown below. The derivation presented in this chapter presents the details of the derivation not shown in [12] and corrects the equation for the power radiated.

4.2 Derivation of Equation for Slot Electric Field

Himdi and Daniel [12] begin by assuming an expression for the electric field in the slot. This electric field expression can be found using transmission line

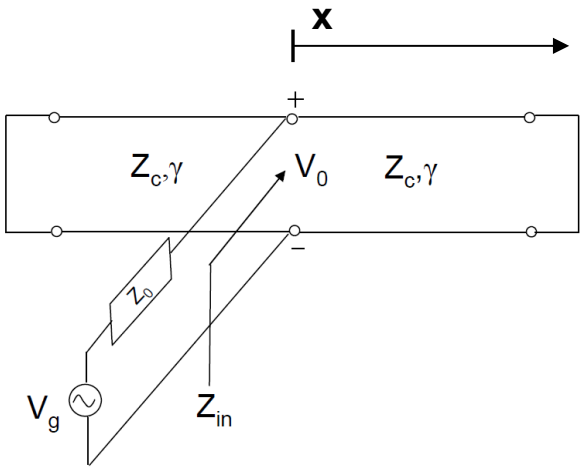

Figure 4.1: Transmission line model of slot antenna.

theory. The voltage on any loaded transmission line can be expressed as

$$V(x) = V_0(e^{-\gamma x} + \Gamma e^{+\gamma x}) \tag{4.1}$$

where Γ is the voltage reflection coefficient at the load, γ is the propagation constant and is defined as

$$\gamma = \alpha + j\beta \tag{4.2}$$

V_o is the excitation voltage, and where x describes the position on the line. For the case of the slot antenna the load is a short. Therefore, Z_L is zero and Γ is equal to -1 as shown below in Equation 4.3.

$$\Gamma = \frac{Z_L - Z_0}{Z_L + Z_0} = -1 \tag{4.3}$$

Given that the Γ is equal to -1, the voltage simplifies as

$$V(x) = V_0(e^{-\gamma x} - e^{+\gamma x}) = V_0^+(-2\sinh(\gamma x)) \tag{4.4}$$

The electric field in the slot can be assumed to be constant in the y-direction for a given position in x due to the aspect ratio of the slot (the length is

much greater than the width and the width of the slot is much less than a wavelength). Moreover, a constant field in the lateral dimension (y-dimension for this case) of the transmission line, for a given longitudinal position (x-dimension for this case) of the line, is always assumed within a transmission line model. Therefore, the electric field in the slot is simply the voltage divided by the slot width:

$$E(x) = \frac{V(x)}{w_a} = \frac{-2V_0}{w_a}\sinh(\gamma x) \tag{4.5}$$

where w_a is the slot width.

Shifting the distribution such that the electric field reflects about the origin, as shown in Figure 4.2, the electric field is defined as

$$E(x) = \frac{V(x)}{w_a} = \frac{-2V_0}{w_a}\sinh\left(\gamma\left(\frac{L_a}{2} - |x|\right)\right)\hat{y} \tag{4.6}$$

The electric field is then normalized so that the voltage at the center of the slot is V_0:

$$E(x) = \frac{V(x)}{w_a} = \frac{-V_0}{w_a}\frac{\sinh\left(\gamma\left(\frac{L_a}{2} - |x|\right)\right)}{\sinh(\gamma\frac{L_a}{2})}\hat{y} \tag{4.7}$$

where

$$V(x) = -V_0\frac{\sinh\left(\gamma\left(\frac{L_a}{2} - |x|\right)\right)}{\sinh(\gamma\frac{L_a}{2})} \tag{4.8}$$

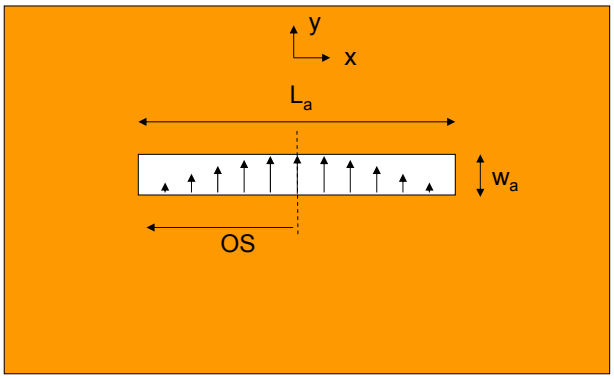

Figure 4.2: Depiction of slot with first mode of electric field.

4.3 Derivation of Equation for Power Radiated

The derivation of the power radiated by the slot antenna begins by assuming the electric field in the slot is as defined in the last section. Therefore the electric field in the aperture, E_a, is

$$E_a = \frac{V(x)}{w_a} = \frac{-V_0}{w_a}\frac{(\sinh(\gamma(\frac{La}{2} - |x|)))}{\sinh(\gamma\frac{L_a}{2})}\hat{y} \tag{4.9}$$

Using the equivalence principle, this electric field can be converted into a magnetic current [13].

$$\vec{M} = -2\hat{z} \times E_a = -2\frac{V_0}{w_a}\frac{\sinh(\gamma(\frac{L_a}{2} - |x|))}{\sinh(\gamma\frac{L_a}{2})}\hat{x} \tag{4.10}$$

The far-field electric fields are approximated by the following equations [13]:

$$E_\theta \approx \frac{-jke^{-jkr}}{4\pi r}(L_\phi + \eta N_\theta) \tag{4.11}$$

$$E_\phi \approx \frac{+jke^{-jkr}}{4\pi r}(L_\theta - \eta N_\phi) \tag{4.12}$$

where L_θ and L_ϕ are as [13]

$$L_\theta = \iint_S (M_x\cos(\theta)\cos(\phi) + M_y\cos(\theta)\sin(\phi) - M_z\sin(\theta))e^{+jkr'\cos(\psi)}dS' \tag{4.13}$$

$$L_\phi = \iint_S (-M_x\sin(\phi) + M_y\cos(\phi))e^{+jkr'\cos(\psi)}dS' \tag{4.14}$$

N_θ and N_ϕ will be zero for this slot antenna analysis method since they are functions of electric current - which is zero for this configuration.

The details showing the derivation of both polarizations of the far-field electric fields, E_θ and E_ϕ, can be found in Appendix A. The final step of the derivation concludes that the power radiated is

$$P_r = \frac{1}{2\eta}\iint_S \Re(|E_\theta|^2 + |E_\phi|^2)r^2\sin(\theta)d\theta d\phi \tag{4.15}$$

where the surface of integration is a hemisphere above the antenna. Putting the expressions for E_θ and E_ϕ into the power radiated integral,

$$P_r = \frac{|k|^2|V_0|^2|\gamma|^2}{2\eta\pi^2|\sinh\left(\gamma\frac{L_a}{2}\right)|^2}\iint_S \frac{[\sin^2(\phi)+\cos^2(\theta)\cos^2(\phi)]}{|\gamma^2+w^2|^2} * \left|\cosh\left(\gamma\frac{L_a}{2}\right)-\cos\left(w\frac{L_a}{2}\right)\right|^2 \sin(\theta)d\theta d\phi \tag{4.16}$$

Canceling terms and placing limits on the integral,

$$P_r = \frac{\zeta|k|^2|V_0|^2|\gamma|^2}{\eta\pi^2|\sinh(\gamma\frac{L_a}{2})|^2}\int_0^{\pi}\int_0^{\frac{\pi}{2}} \frac{[\sin^2(\phi)+\cos^2(\theta)\cos^2(\phi)]}{|\gamma^2+w^2|^2} * \left|\cosh(\gamma\frac{L_a}{2})-\cos(w\frac{L_a}{2})\right|^2 \sin(\theta)d\theta d\phi \tag{4.17}$$

An extra factor of ζ was added to the front of the integral. This factor is to account for the fact that the slot antenna is radiating into both half-spaces and the derivation assumes it only radiates into the upper half-space due to the treatment of the magnetic current. If the slot is placed on a substrate of air, then ζ will be equal to 2. Otherwise,

$$\zeta = 1 + \frac{1}{\sqrt{\epsilon_r}} \tag{4.18}$$

where ϵ_r is the substrate's relative dielectric constant. The formula shown in Equation 4.18 is that presented by Himdi and Daniel in [12].

The formula given for radiated power by Himdi and Daniel in [12] is

$$P_r = \frac{\zeta|\gamma|^2|\alpha|^2}{\eta|\gamma^2+w^2|}\frac{k^2|V_0|^2}{4\pi^2\left|\sinh\left(\gamma\frac{L_a}{2}\right)\right|^2} * \int_0^{\pi}\int_0^{\pi/2}\sin(\theta)(\sin^2(\phi)+\cos^2(\theta)\cos^2(\phi)) * \left|\cosh\left(\frac{\gamma L_a}{2}\right)-\cos\left(\frac{wL_a}{2}\right)\right|^2 d\theta d\phi \tag{4.19}$$

There are small but significant differences between the formula in Equation

4.19 derived by Himdi and Daniel and the formula in Equation 4.17. The magnitude of the impedance predicted by the equation derived by Himdi and Daniel will not match as well as that of the equation derived in this work.

4.4 Deriving Z_{in}

Figure 4.3 shows the slot antenna with the offset feed location labeled. The input impedance, Z_{in}, at the locations $x = -OS$ in Figure 4.3 can be represented as

$$Z_{in} = \frac{Z_L Z_R}{Z_L + Z_R} \tag{4.20}$$

where

$$Z_L = Z_c \tanh(\gamma l_L) \tag{4.21}$$

Z_L is the impedance looking to the left at the input into the shorted slot line. The length of the line to the left is

$$l_L = \frac{L_a}{2} - OS \tag{4.22}$$

where OS is the offset from the center. Similarly,

$$Z_R = Z_c \tanh(\gamma l_R) \tag{4.23}$$

and

$$l_R = \frac{L_a}{2} + OS \tag{4.24}$$

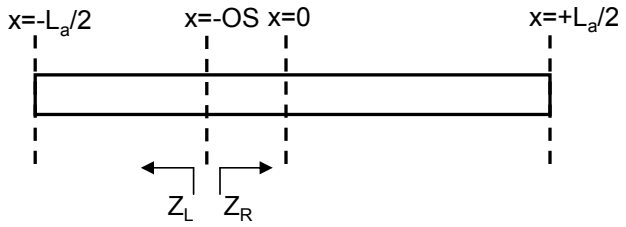

Figure 4.3: Depiction of slot with offset feed location labeled.

Substituting the impedances into the equation for the input impedance,

$$Z_{in} = \frac{Z_c \tanh(\gamma(\frac{L_a}{2} - OS)) Z_c \tanh(\gamma(\frac{L_a}{2} + OS))}{Z_c \tanh(\gamma(\frac{L_a}{2} - OS)) + Z_c \tanh(\gamma(\frac{L_a}{2} + OS))} \tag{4.25}$$

Factoring out Z_c,

$$Z_{in} = \frac{Z_c \tanh(\gamma(\frac{L_a}{2} - OS)) \tanh(\gamma(\frac{L_a}{2} + OS))}{\tanh(\gamma(\frac{L_a}{2} - OS)) + \tanh(\gamma(\frac{L_a}{2} + OS))} \tag{4.26}$$

If $OS = 0$ (feed at the slot's center), then the input impedance simplifies to

$$Z_{in} = \frac{Z_c}{2} \tanh\left(\gamma \frac{L_a}{2}\right) \tag{4.27}$$

4.5 Deriving P_{in} and V_0

The power delivered to a load for the circuit shown in Figure 4.4 is defined as [9]

$$P_{in} = \frac{1}{2}|V_g|^2 \frac{R_{in}}{(R_{in} + R_g)^2 + (X_{in} + X_g)^2} \tag{4.28}$$

where V_g is the generator voltage,

$$Z_{in} = R_{in} + jX_{in} \tag{4.29}$$

and

$$Z_g = R_g + jX_g \tag{4.30}$$

For the model discussed, it is assumed that

$$V_g = 1 \tag{4.31}$$

and

$$R_g = Z_0 \tag{4.32}$$

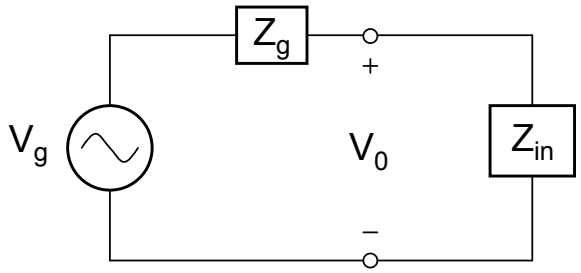

Figure 4.4: Depiction of circuit to describe power delivered to antenna.

and

$$X_g = 0 \tag{4.33}$$

Therefore,

$$P_{in} = \frac{1}{2} \frac{\Re(Z_{in})}{(\Re(Z_{in}) + Z_0)^2 + (\Im(Z_{in}))^2} \tag{4.34}$$

Putting the formula for the input impedance into the equation for the power delivered to a load,

$$P_{in} = \frac{Z_c \sinh(L_a \alpha)}{(4Z_0^2 - Z_c^2)\cos(L_a \beta) + (4Z_0^2 + Z_c^2)\cosh(L_a \alpha) + 4Z_0 Z_c \sinh(L_a \alpha)} \tag{4.35}$$

The last value left to determine is V_0. It can be found using transmission line theory and is defined as

$$V_{in} = V_0 = V_g \frac{Z_{in}}{Z_{in} + Z_g} = \frac{\frac{Z_c}{2} \tanh(\gamma \frac{L_a}{2})}{\frac{Z_c}{2} \tanh(\gamma \frac{L_a}{2}) + Z_0} \tag{4.36}$$

Simplifying,

$$V_{in} = \frac{1}{1 + \frac{2Z_0}{Z_c} \coth(\gamma \frac{L_a}{2})} \tag{4.37}$$

4.6 Comparison of Transmission Line Model with HFSS Results

To validate the transmission line model of the slot antenna, an analysis was undertaken to compare its results to that of HFSS. A MATLAB program was written to use the transmission line model to find the input impedance of a slot antenna. It numerically integrates the power radiated equation and uses a built-in optimization routine, fzero, to find α. It uses Cohn's method to calculate the characteristic impedance and guide wavelength of the slot [14]. The dimensions of the antenna analyzed were: $L_{gp} = 440$ mm, $W_{gp} = 300$ mm, $w_s = 6$ mm, $L = 175$ mm. OS is the feed-point offset and was varied from 0 to 87.5 mm. This analysis and model were for a slot antenna alone with no reflecting plane. Future work will extend this model to accommodate a reflecting plane.

A comparison of the two analysis methods is shown in Figure 4.5, where Figure 4.5(a) shows the real part of the input impedance and Figure 4.5(b) shows the imaginary part of the input impedance. As can be seen in the figure, the two analysis methods match fairly well. The transmission line model and simulation results are slightly different in magnitude for the real part of the impedance, especially for the center feed point. The HFSS simulations also show a broader response. This is likely due to the closed form model's assumption that the ground plane is infinite.

4.7 Conclusions

Using the method suggested by Himdi and Daniel in [12], a transmission line model for the slot antenna was derived. The correct equation for the power radiated by the slot was found through a detailed re-derivation. The results of the transmission line model match well with simulations. The next chapter expands this transmission line model to be appropriate for wider slots and frequencies past the first resonance. The extended transmission line model

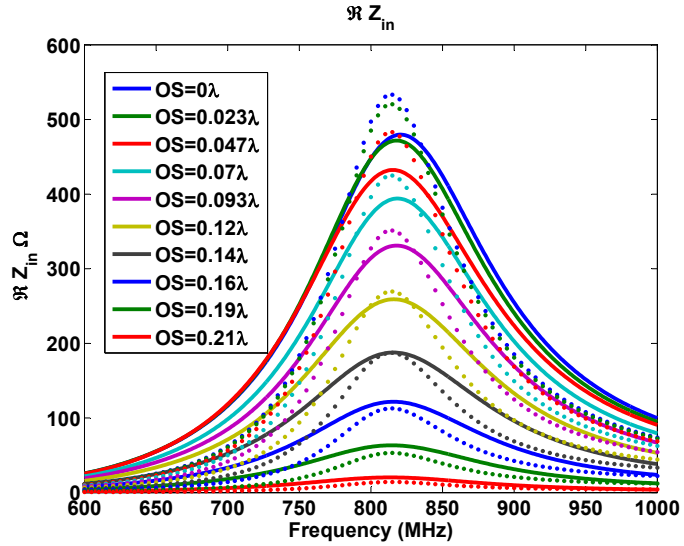

(a)

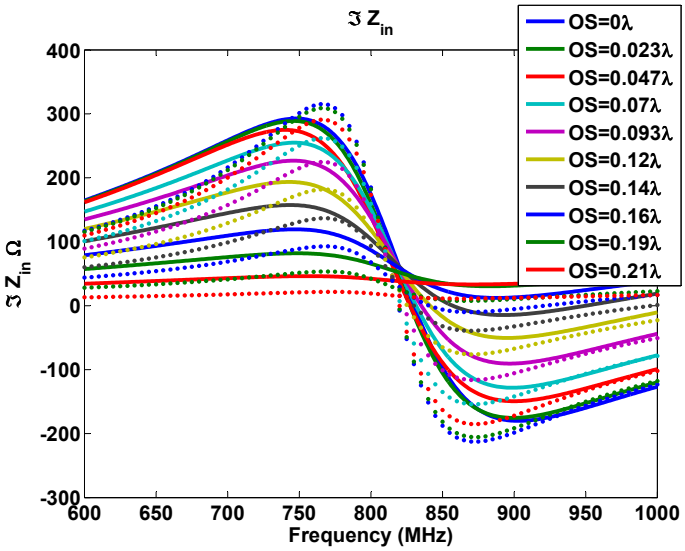

(b)

Figure 4.5: Comparison of transmission line model with results from HFSS for different feed points. The dotted lines are the results of the transmission line model and the solid lines are the results from HFSS. The frequency used to define the wavelength to which the feed offset, OS, is referenced is 800 MHz.

will be used with a transmission line model for a slotline inductor derived in later chapters to design a slot antenna that operates in multiple frequency bands.

CHAPTER 5

TRANSMISSION LINE MODEL OF SLOT ANTENNA EXTENDED

5.1 Introduction

This chapter presents a transmission line model that improves upon the previous model to increase the model's flexibility. The treatment of the voltage in the slot and the method used to account for radiative losses was insufficent for the loaded slot antenna used in Chapter 7. A different expression for the voltage in the slot is derived in this chapter and an expression for the inductance of the shorted ends of the slot is presented - an important addition for the wider slots investigated in this chapter. While the slot widths are wider than those discussed in the previous chapter, the width still must be significantly less than the length of the slot for the transmission line model assumptions to hold (voltage approximately constant across the slot). The model also changes the mechanism to account for radiative losses in the slot - using a conductance-per-unit-length, G, instead of an α (loss per-unit-length) added to the propagation constant. This is an important change since, as frequency increases, the low-loss condition no longer holds where the simple addition of α to the propagation constant is appropriate to represent the loss.

5.1.1 Slot Voltage Distribution

The voltage distribution discussed in the previous chapter, and described in Equation 4.8, does not hold past the first resonance because the voltage distribution can no longer be assumed to be a sinc function of the absolute value of

x. To determine a more general equation for the voltage, the slot needs to be considered as a modal structure. Figure 5.1 shows a slot with identical loads and the feed position offset from the center. The following presents a more general expression for the voltage on the slot.

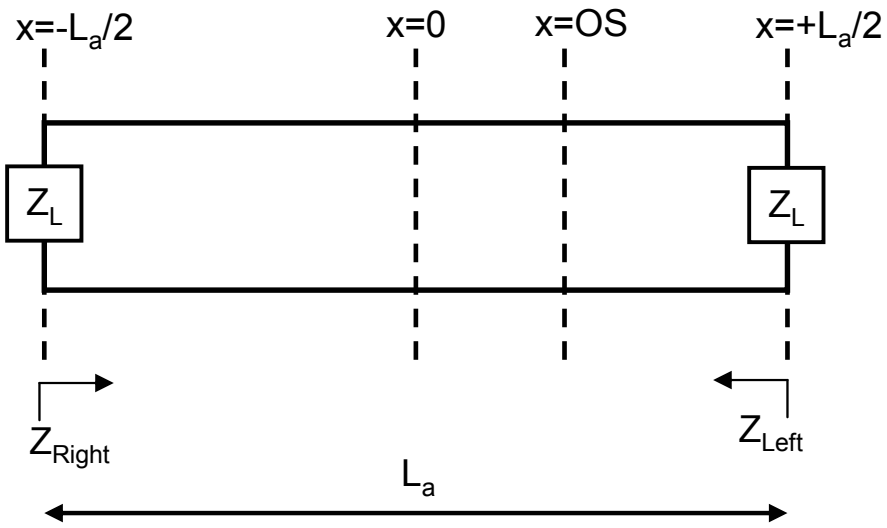

Figure 5.1: A slot with the shorts modeled as inductances.

As discussed in the previous chapter, the voltage on any transmission line can be expressed as a summation of forward and backward traveling waves. The difference between the equation used in the last chapter for the voltage in the slot and the more general equation discussed in this chapter is that multiple modes will be allowed in the slot. The voltage wave in the slot can be expressed as

$$V(x) = A\left(e^{-\gamma_m x} + \frac{B}{A}e^{\gamma_m x}\right) \tag{5.1}$$

where γ_m and $\frac{B}{A}$ are different for the many possible modes that could exist within the slot structure and will be solved for in the following discussion. The current can also be expressed as

$$I(x) = \frac{A}{Z_c}\left(e^{-\gamma_m x} - \frac{B}{A}e^{\gamma_m x}\right) \tag{5.2}$$

where Z_c is the characteristic impedance of the slot. Therefore, the impedance can be expressed as

$$Z(x) = \frac{V(x)}{I(x)} \tag{5.3}$$

The impedance across the slot at the loads can be expressed as

$$Z\left(x = \frac{-L_a}{2}\right) = Z\left(x = \frac{+L_a}{2}\right) = \frac{Z_L Z_{Line}}{Z_L + Z_{Line}} \tag{5.4}$$

assuming no termination at the input port, where

$$Z_{Line} = Z_{Left} = Z_{Right} = Z_c \frac{Z_L + Z_c \tanh(\gamma L_a)}{Z_c + Z_L \tanh(\gamma L_a)} \tag{5.5}$$

as defined in [9]. Knowing the boundary conditions of the known impedance at the ends of the slots, the modal propagation constant γ_m and the ratio between the forward and backward voltage waves $\frac{B}{A}$ can be determined to be

$$\gamma_m = \frac{jm\pi}{L_a} \tag{5.6}$$

$$\frac{B}{A} = \frac{-(e^{jm\pi}(3Z_L Z_c + Z_c^2 e^{2L_a\gamma} - 2Z_L^2 - Z_c^2 + Z_L Z_c e^{2L_a\gamma}))}{Z_L Z_c + 2Z_L^2 e^{2L_a\gamma} + Z_c^2 e^{2L_a\gamma} - Z_c^2 + 3Z_L Z_c e^{2L_a\gamma}} \tag{5.7}$$

where m is all integers from one to infinity and m represents the mode. If the loads are assumed to be perfect shorts, $Z_L = 0$, the ratio between the forward and backward waves simplifies to

$$\frac{B}{A} = -e^{jm\pi} \tag{5.8}$$

A general expression for the voltage in slot is

$$V(x) = A \sum_{m=1}^{\infty} A_m \left(e^{-\gamma_m x} + \frac{B}{A} e^{\gamma_m x}\right) \tag{5.9}$$

where A_m can be assumed to be

$$A_m = \frac{1}{(1- \mid (\gamma_m - \gamma) \mid^2)} \tag{5.10}$$

The relative weighting of the modes expressed using the function for A_m in the slot allows for the automatic prediction of the dominant mode in the structure. Although the sum is presented as a sum from one to infinity, in practice the first 100 terms are sufficient for all slot lengths discussed in this work and likely for all practical slot lengths. The magnitude of the voltage wave can then be determined by

$$A = \frac{V_0}{\sum_{m=1}^{\infty} A_m (e^{-\gamma_m OS} + \frac{B}{A} e^{\gamma_m OS})} \tag{5.11}$$

where

$$V_0 = \frac{V_g Z_{in}}{Z_{in} + Z_g} \tag{5.12}$$

Again, the first 100 terms of the sum are sufficient.

Figure 5.2 shows a comparison between this new expression for the voltage in the slot versus the commonly used expression for the voltage in a slot discussed in Section 4.2. The figure shows the magnitude of the voltage distribution in the slot for slot lengths varying between $\lambda/10$ to $3\lambda/2$. As can be seen in the figure, the old equation for the voltage describes non-physical distributions for slot lengths greater than a half wavelength as shown in parts (c) and (d) of the figure.

5.1.2 Expression for Inductances of Shorts

As should be expected, as frequency and the width of the slot increase, the shorted ends of the slot no longer look like true shorts. The shorts appear inductive. The following expression can be used for the inductance of the shorts:

$$L = 0.2 w_s \Big(\ln \left(\frac{4w_s}{d} \right) + \frac{d}{2w_s} - 1 \Big) [\text{nH}] \tag{5.13}$$

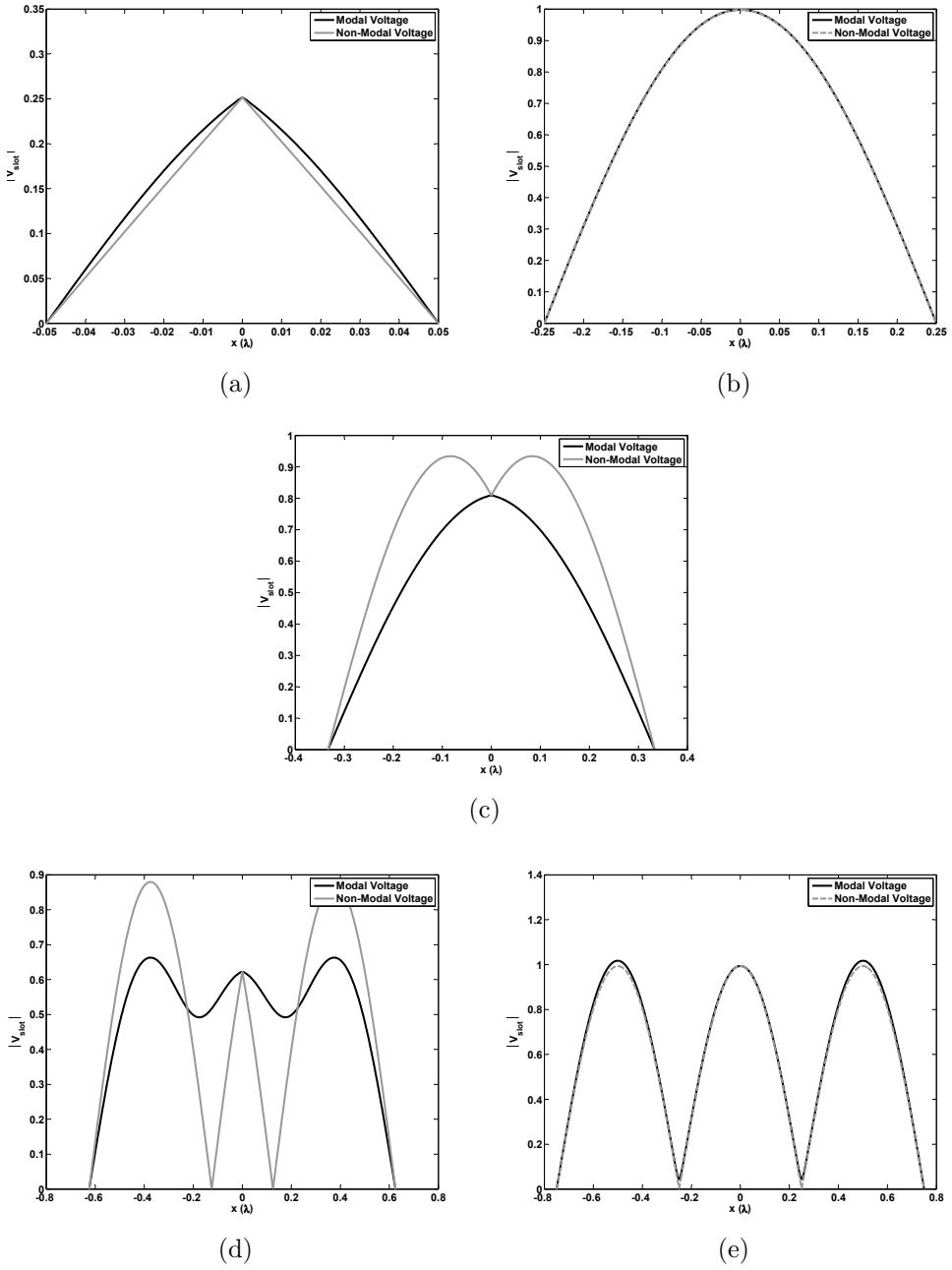

Figure 5.2: The absolute value of the voltage along a slot using the modal voltage derived in this chapter and the commonly used expression for the voltage discussed in Section 4.2 in Equation 4.8 for slots of length (a) $\lambda/10$, (b) $\lambda/2$, (c) $2\lambda/3$, (d) $5\lambda/4$, (e) $3\lambda/2$.

where w_s is the width of the slot and d is the effective width, both in mm [15]. This expression is for the inductance of a wire, where w_s is the length and d is the width. An expression for d, the thickness of the wire, to use to approximate the inductance could not be found in the literature. However, the following expression functions well for the slot dimensions studied in this work:

$$d = \frac{w_s + h_m}{20p^2} \tag{5.14}$$

where

$$p = \frac{\lambda_0}{\lambda} \tag{5.15}$$

and h_m is the thickness of the metal of the ground plane. The expression for p follows from Cohn [14]. The expression for d was surmised by assuming that the effective width for the inductance formula would increase with increasing slot width and metal thickness. It was also assumed that d would decrease with increasing relative permittivity - which is reflected by dividing by p. The factor of 20 was a factor that was found through trial and error to be appropriate and shifts the frequency response of the model minutely. The shorted ends of the slot also begin to radiate as frequency and width increase. The following expression can be used for the resistance to reflect this radiation:

$$R = \left(2.63 \times 10^{-3}\right) \frac{w_s}{d} \sqrt{f} \tag{5.16}$$

where f is the frequency in GHz [15]. The impedance at the short is then

$$Z_L = R + j\omega L \tag{5.17}$$

where R is described in Equation 5.16 and L is described in Equation 5.13.

5.1.3 Lossy Line Parameters

As the electrical length and width of the slot increase, the low-loss condition no longer holds in which a loss-per-unit-length α can simply be added to the propagation constant. Instead, conductance and resistance per-unit-length

must be used to account for the loss, and the following equations must be used for the characterictic impedance and propagation constant of the line, respectively:

$$Z_c = \sqrt{\frac{(R + j\omega L_c)}{(G + j\omega C_c)}} \tag{5.18}$$

and

$$\gamma = \sqrt{(R + j\omega L_c)(G + j\omega C_c)} \tag{5.19}$$

where R is the resistance per-unit-lenth, G is the conductance per-unit-length, L_c is the inductance per-unit-length, and C_c is the capacitance per-unit-length [9]. The inductance and capacitance per-unit-length can be determined by

$$L_c = \frac{1}{2\omega}(\beta Z_c^{lossless}) \tag{5.20}$$

$$C_c = \frac{1}{2\omega}(\frac{\beta}{Z_c^{lossless}}) \tag{5.21}$$

where

$$\beta = \frac{2\pi}{\lambda} \tag{5.22}$$

and $Z_c^{lossless}$ and λ are determined using Cohn's method [14].

The conductance-per-unit-length can be expressed as

$$G = G_{rad} + G_{loss} \tag{5.23}$$

where G_{rad} reflects the loss due to radiation by the slot and G_{loss} reflects loss due to imperfections of the dielectric of the substrate backing the antenna if it is present. This loss due to the dielectric can be approximated by

$$G_{loss} = 2\pi f \delta \epsilon_0 p^2 4 \frac{h_m}{w_s} \tag{5.24}$$

where δ is the loss tangent of the dieletric. The expression is from the conductance-per-unit-length in a parallel plate waveguide with the plate width assumed to be four times the height of the metal of the ground plane within which the slot exists [9]. The extension of the width in the calculation of the

conductance-per-unit length in parallel plate waveguide to be four times the height of the metal is to account for the fringing of the electric field in the slot. The resistance-per-unit-length of the slot can be approximated by

$$R = \frac{2R_s}{\pi d} \tag{5.25}$$

where

$$R_s = \sqrt{\frac{\pi f \mu}{\sigma}} \tag{5.26}$$

and σ and μ are the conductivity and permeability of the metal, respectively, and h_m and w_s are the height of the metal and the width of the slot, respectively. This expression for the resistance-per-unit-length comes from that of twin lead [9].

5.1.4 Power Condition for Determining Conductance

The modal voltage expression does not lend itself to symbolic integration. However the following expression for the power radiated

$$P_r = \frac{\zeta}{2\eta}\int_0^{2\pi}\int_0^{\frac{\pi}{2}} \frac{|k|^2}{(4\pi)^2}\left|\frac{4\sin(\frac{w_s g}{2})}{g w_s}[\sin^2(\phi)+\cos^2(\theta)\cos^2(\phi)]\right. \tag{5.27}$$
$$\left. * \int_{-L_a/2}^{+L_a/2} \frac{V(x')}{w_a} e^{jx' sin\theta cos\phi} dx' \sin(\theta) d\theta d\phi\right|^2$$

where

$$\zeta = 1 + \frac{1}{p} \tag{5.28}$$

can be integrated numerically in Matlab with a single for-loop that can be executed in parallel with the help of the function for trapezoidal numerical integration. The expression for the total power radiated in Equation 5.27 follows from the derivation for power radiated in the last chapter culminating in Equation 4.17.

The power delivered to the slot that can be equated to the power radiated

to determine the conductance-per-unit-length due to radiation is expressed as

$$P_d = \sum_{x=-L_a/2}^{L_a/2} 1/2|V(x)|^2 G_{rad} \Delta_x \tag{5.29}$$

where Δ_x is the resolution of the slot voltage distribution. Equation 5.29 assumes that the voltage is constant over some very small length of the slot and finds the power delivered to this very small length. The expression employed in Section 4.5 for the old transmission line model is no longer appropriate since loss other than radiative loss is considered. As with the old transmission line model, the power radiated and power delivered have a linear relationship with the radiative conductance-per-unit-length. Due to this linear relationship, G_{rad} is easily determined. The appropriate conductance-per-unit length to represent radiative losses, G_{rad}, is when the power radiated is equal to the power delivered to the slot. To determine the appropriate G_{rad}, the power delivered and power radiated are calculated for values of G_{rad}. With these two data points, the linear functions of the power radiated and power delivered with G_{rad} can be determined. Given these linear functions, the appropriate G_{rad} can be determined at the interception point for the linear functions of the power radiated and power delivered.

5.2 Results

Both a center and offset-fed slot that were 100 mm long and 4 mm wide on Rogers RO4230 dielectric with a height of 0.762 mm (ϵ_r=2.98 and δ=.001) were simulated in a full-wave solver (HFSS), analyzed using the new transmission line model, and constructed and measured. The constructed slot used a long length of semi-rigid coax to act as a "Dyson-like" balun to feed the antenna as a gap source [16]. The outer-conductor of the semi-rigid coax was soldered to the ground plane on one side of the slot and the inner conductor was extended across the slot and soldered to the opposite side of the slot. The constructed slot with this gap source is shown in Figure 5.3.

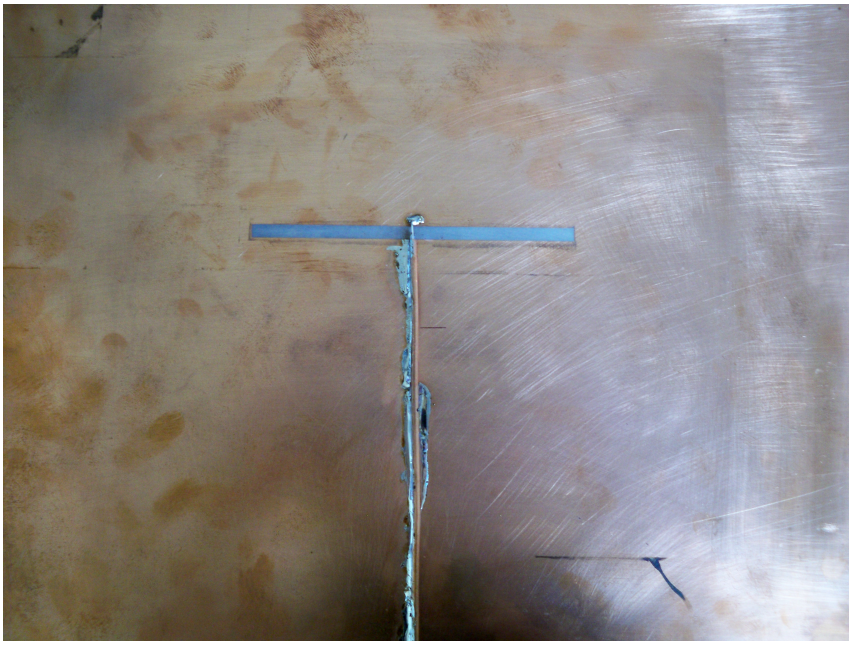

(a)

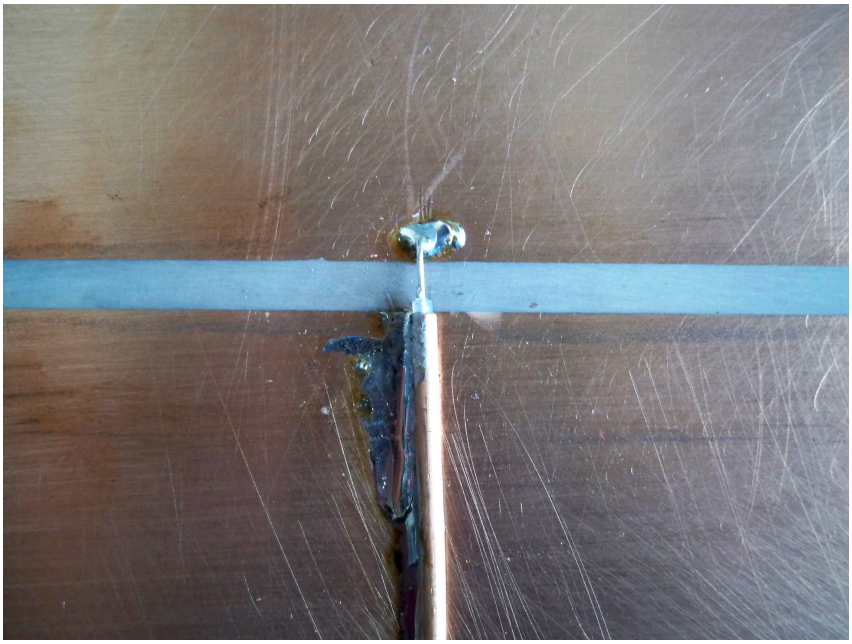

(b)

Figure 5.3: Photograph of the constructed slot employing semi-rigid coax to act as both a gap-source and a "Dyson-like" balun. (a) The length of semi-rigid coax used, (b) Detail of gap source.

The slot was excited in the full-wave solver in two different ways. The first was a simple lumped port across the slot and the second was with coaxial cable acting as a gap-source. The coaxial cable acting as a gap source was how the measured antenna was excited. The simulations for both excitation types are compared to the measured results for the center-fed slot in Figure 5.4 and for the offset-fed slot in Figure 5.5. As can be seen in the figures, the gap-source feeding method presents a small inductance as frequency increases. As can also be seen in the figures, the results of the full-wave solver are reliable for comparison to the transmission line model. Higher-order effects do appear in the measured results as frequency increases. This is likely due to the expansion of the dielectric in the feeding coaxial cable that is unavoidable as the cable is soldered to the ground plane of the slot.

The results of the new transmission line model are compared to the full-wave solver predictions for the center-fed slot in Figure 5.6 and for the offset-fed slot in Figure 5.7. As can be seen in the figures, the transmission line model does agree with the full-wave predicted impedance. As frequency increases, the transmission line model under-estimates the losses in the slot. There is likely another radiative mechanism for which the transmission line model does not account. This other radiative mechanism could also contribute to the imaginary part of the impedance predicted by the transmission line model not matching the full wave prediction away from the anti-resonance of the slot structure. The unaccounted for radiative losses can be attributed to a frequency shift due to the relationship between the propagation constant and the resistance and conductance per-unit-length described in Equation 5.19.

A comparison of the impedance predicted by the original transmission line model discussed in Chapter 4 with the new transmission line model and the predicted impedance by HFSS is shown in Figure 5.8 for the offset-fed slot. As can be seen in the figure, the old model is increasingly inaccurate with frequency. The model is particularly inaccurate for resonances when a center-fed slot would be located at a null in the voltage distribution. This is due to the fact that the old transmission line model does not differentiate in the calculation of the loss-per-unit-length between center and offset feed positions.

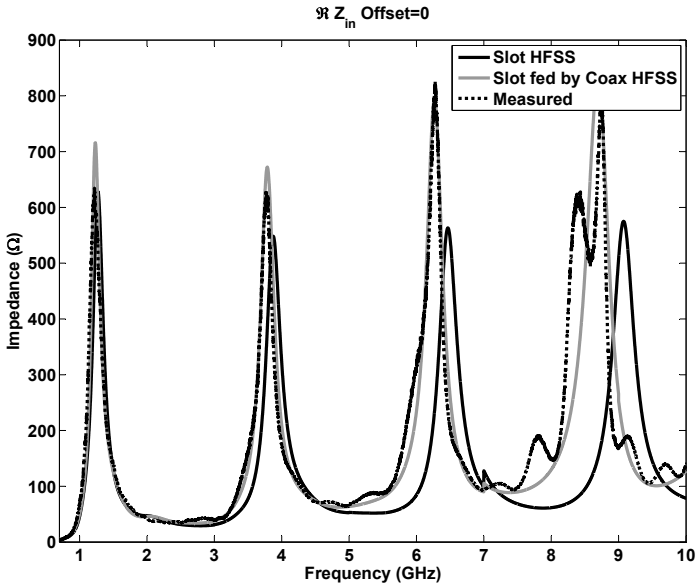

(a)

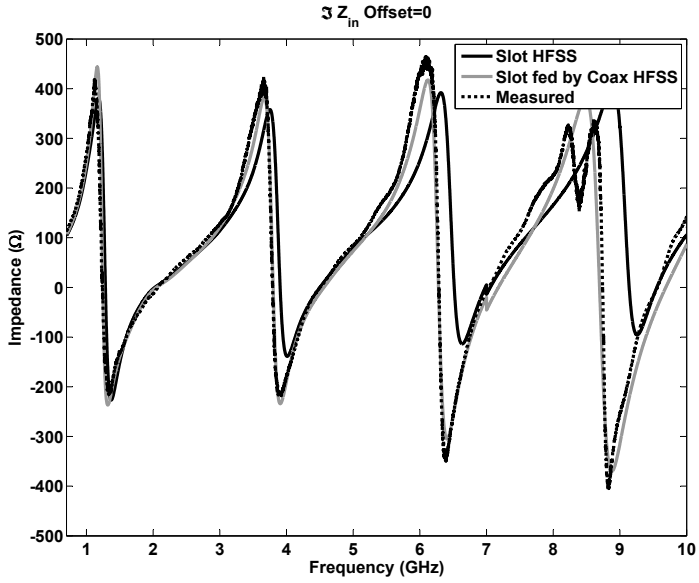

(b)

Figure 5.4: Comparison of simulated center-fed slot excited using lumped port and with gap source using coaxial cable versus measured. (a) Real part, (b) Imaginary part. The slot antenna dimensions were 100 mm long and 4 mm wide on Rogers RO4230 dielectric with a height of 0.762 mm (ϵ_r=2.98 and δ=0.001).

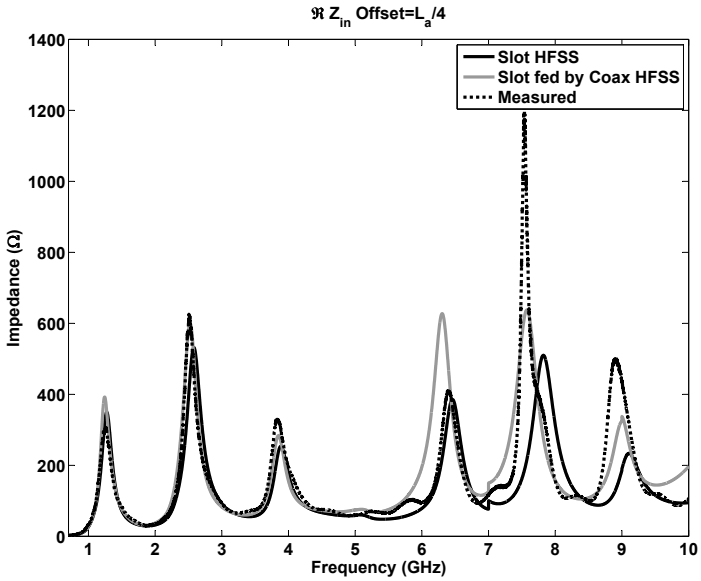

(a)

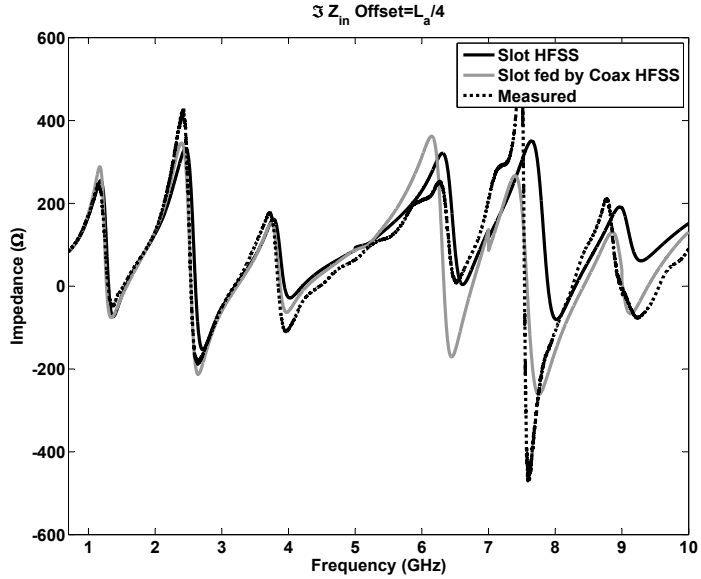

(b)

Figure 5.5: Comparison of simulated offset-fed slot excited using lumped port and with gap source using coaxial cable versus measured. (a) Real part, (b) Imaginary part. The feed was offset from the center point by one-fourth of the slot length. The slot antenna dimensions were 100 mm long and 4 mm wide on Rogers RO4230 dielectric with a height of 0.762 mm (ϵ_r=2.98 and δ=0.001).

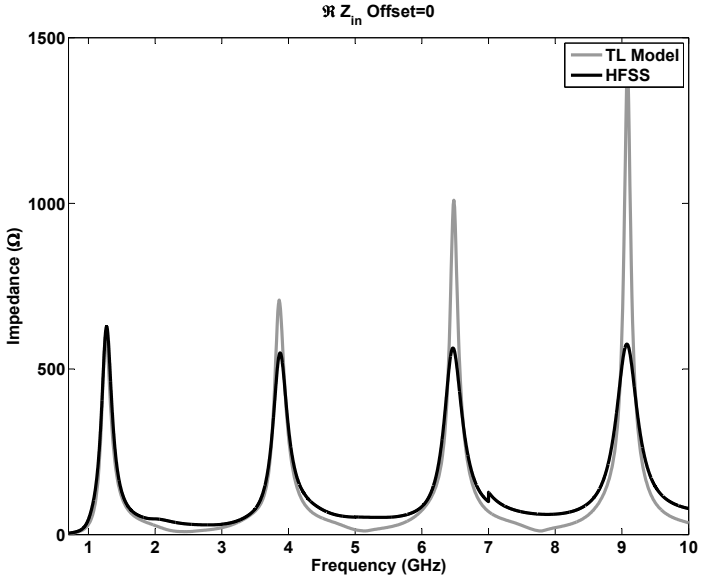

(a)

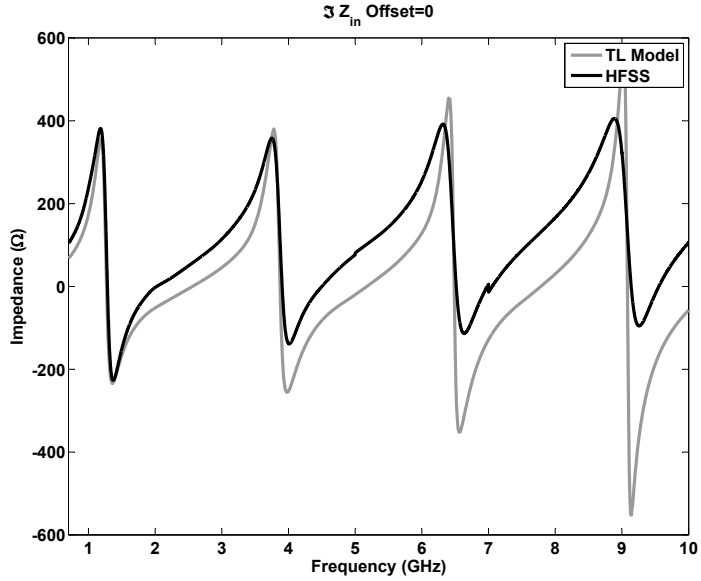

(b)

Figure 5.6: Comparison of impedance predicted by a full-wave solver versus the transmission line model for a center-fed slot antenna. (a) Real part, (b) Imaginary part. The slot antenna dimensions were 100 mm long and 4 mm wide on Rogers RO4230 dielectric with a height of 0.762 mm (ϵ_r=2.98 and δ=0.001).

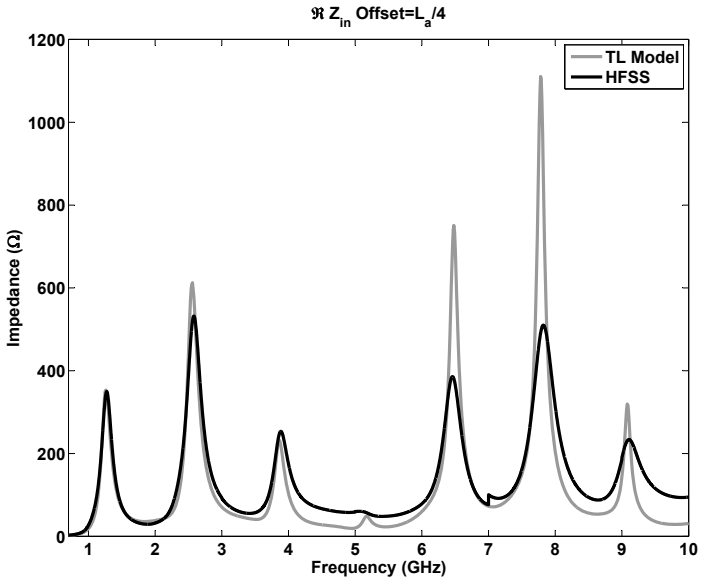

(a)

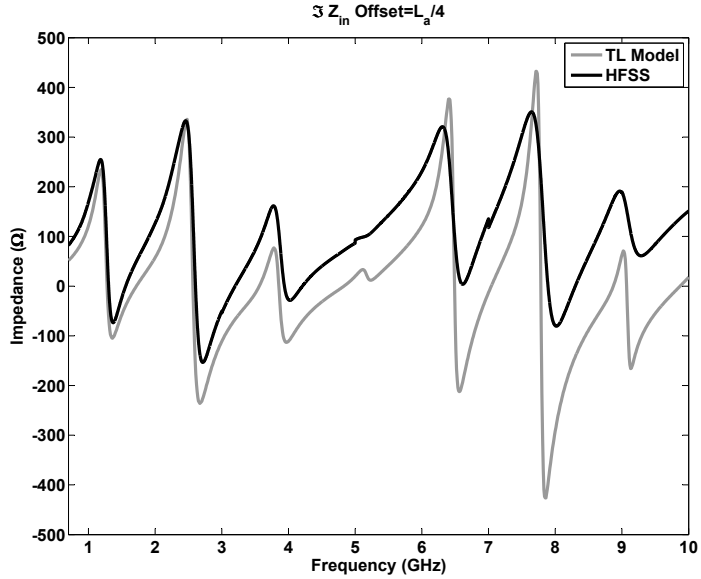

(b)

Figure 5.7: Comparison of impedance predicted by a full-wave solver versus the transmission line model for an offset-fed slot antenna. (a) Real part, (b) Imaginary part. The feed was offset from the center point by one-fourth of the slot length. The slot antenna dimensions were 100 mm long and 4 mm wide on Rogers RO4230 dielectric with a height of 0.762 mm (ϵ_r=2.98 and δ=0.001).

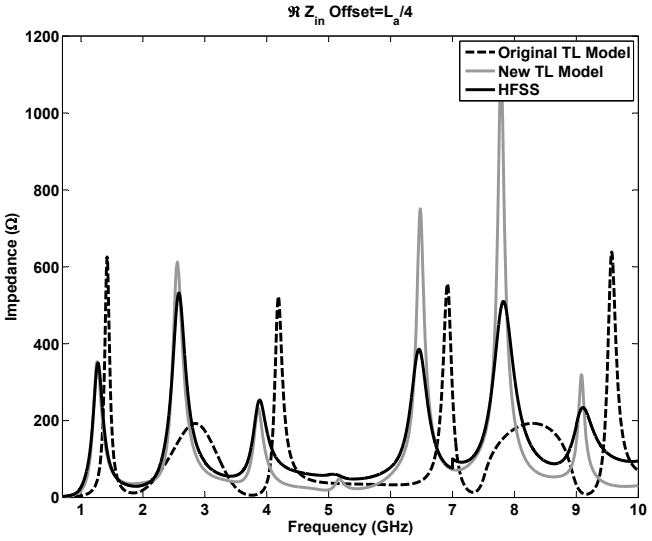

(a)

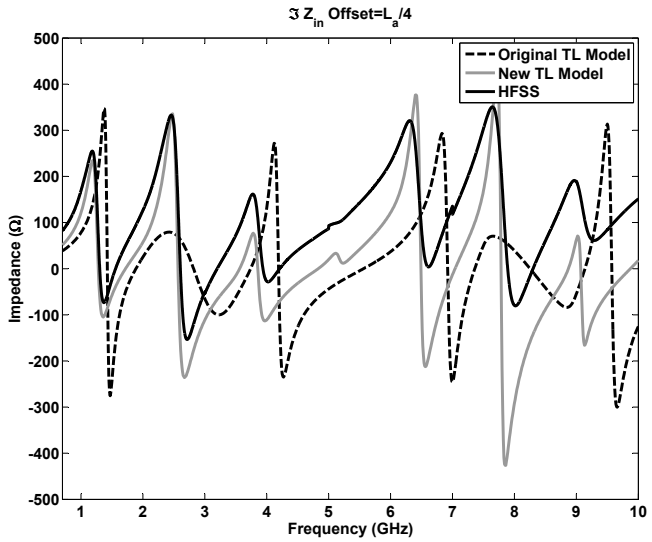

(b)

Figure 5.8: Comparison of impedance predicted by a full-wave solver versus the old transmission line model discussed in the beginning of the paper versus that derived later that uses a conductance and a modal voltage for an offset-fed antenna. (a) Real part, (b) Imaginary part. The feed was offset from the center point by one-fourth of the slot length. The slot antenna dimensions were 100 mm long and 4 mm wide on Rogers RO4230 dielectric with a height of 0.762 mm (ϵ_r=2.98 and δ=0.001).

5.3 Conclusions

In Chapter 4 a more complete derivation of the transmission line model for the slot antenna presented by the authors in [12] was detailed. This model is accurate for center-fed slots of narrow width with lengths of near or less than a half-wavelength long. A new transmission line model that rectifies many of the problems with the old model was presented in this chapter. The new model more accurately represents the voltage distribution in the slot. The new model also uses a conductance per-unit-length, G_{rad}, instead of an α to represent the radiative losses, which allows the model to better predict the behavior of the antenna for the condition when the losses contribute to a frequency shift in the input impedance of the antenna. In addition, the new model allows for the accurate prediction of the impedance for an offset fed antenna. Finally, the new model also details a method to account for the inductive nature of the shorts of a slot antenna.

The new transmission line model, conveniently, could also be used to predict radiation patterns of the slot structure since the far-fields are found with this method. This new transmission line model does not account for all radiation mechanisms for the slot structure and is therefore not perfectly accurate for slots that are more than a half-wavelength long. However, the transmission line model is useful for arriving at better than a first-order approximation of the impedance of the slot structure and is orders of magnitude faster than a full-wave solver. The transmission line model arrives at a prediction of the impedance of a slot antenna within seconds, whereas the full-wave solver required a full day to solve for the input impedance at the high end of the frequency range analyzed for this chapter. This new transmission line model provides an important approximation for the impedance of a nearly ubiquitous structure within electromagnetics - the simple slot antenna.

CHAPTER 6

RECTANGULAR SLOTLINE INDUCTOR

6.1 Introduction

A transmission line model of the slotline inductor was pursued to aid in the design process of the inductor-loaded slot antenna. A transmission line model for the inductor loaded slot provides a significant reduction in the time required for design by removing the requirement of a full-wave solver for a significant portion of the design process.

A depiction of a three-turn slotline inductor is shown in Figure 6.1 with dimensions. As can be seen in the figure, the planar inductor is a set of four connected multi-conductor transmission lines. The transmission line model for the slotline inductor is based upon the work of Shepherd outlined in [17]. Since multi-line transmission line characteristics are time consuming and difficult to compute, the model by Shepherd seeks to use the characteristics of two-line coupled lines to approximate the multi-line transmission line.

The transmission line model for the rectangular inductor derived in this chapter accurately predicts the location of the first resonance of the structure. However, as frequency increases the corners of the inductor begin to affect the impedance - causing reflections large enough that the entire inductor is not visible. A circular inductor is analyzed in the next chapter to avoid this problem. However, the method presented for analysis of the rectangular inductor is an important step leading to the method used for the circular inductor.

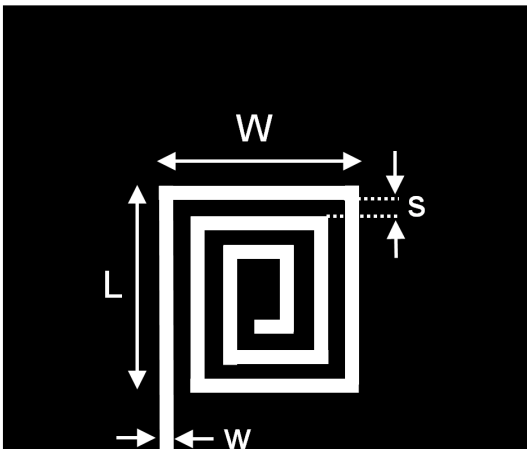

Figure 6.1: Slotline inductor with dimensions labeled.

6.2 Rectangular Inductor Model

Shepherd [17] deconstructs the multiline transmission line into parallel singly coupled transmission lines. One side of the three-turn rectangular inductor is depicted in Figure 6.2. The figure shows how the coupling lengths for a section of line are calculated. In the figure, the coupling lengths for Line 1 coupling to Lines 2 and 3 are shown. In the figure, the sections of the lines are denoted by L_{xy}. The x denotes the section to which the line belongs. The y denotes the secondary line to which the primary line is coupling. In the rectangular spiral inductor, a length of line can be broken up into three sections. In the first section, the line is in isolation when referencing a coupling configuration for a line toward the center of the spiral because there is no slotline directly next to the line in this section. If the coupling configuration is toward the outside of the spiral, the line is not in isolation. In the second section, the line couples to the neighboring line. In the third section, the line is again in isolation. In the model, the coupling length is an average of the two lengths of line (primary and secondary). The difference between the coupling length and the actual physical lengths is halved and is used as the length of the line in sections one and three to account for coupling of lines not directly beside each other. If the section of line under consideration is an inner line and the coupling configuration under analysis is to a line further out in the inductor,

the entire length of line is considered to be coupling to the outer line.

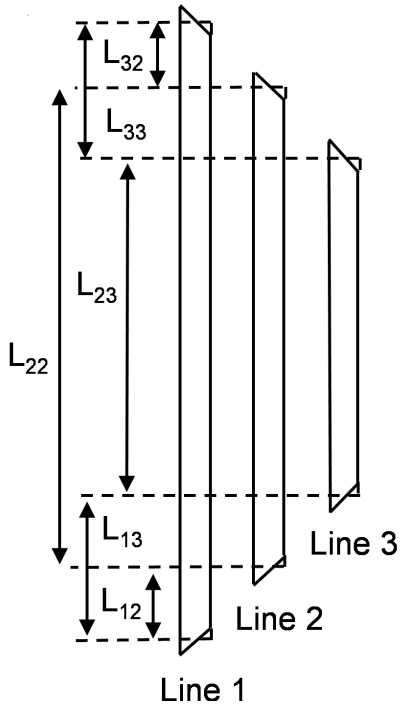

Figure 6.2: One section of slotline inductor with line length dimensions labeled.

Current curving has long been noticed in corners of transmission lines. Shepherd assumed in his model that there was no current curving and merely used the midpoint of the diagonal line showing the intersection between sides of the inductor. We assumed, and noticed this effect in images of fields in HFSS [6], that the current curving phenomena occurred with electric fields in slot-line. The image in Figure 6.3 depicts how we calculate the effective length for the corner of a slot transmission line. This effective length is used in the calculation of lengths shown in Figure 6.2. As can be seen in the figure, a circle (with a radius of half of the slot width) is placed with a center-point at the lower right of a corner. The arc (shown in orange), which is one-quarter of the total circumference of the circle, is the effective length of one-half of a corner in the slot-line inductor.

Using the lengths defined above, the method for assembling the transmission

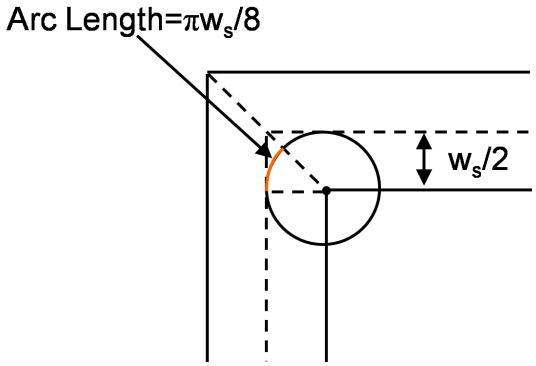

Figure 6.3: A corner of the slotline inductor depicting the assumption of field curving at corners.

line model of the slotline inductor is as follows. An ABCD matrix is calculated for each pair of coupled lines in isolation. In the case of the three-turn inductor, this would entail an ABCD matrix for the coupling configuration between Line 1 and Line 2 and another for the configuration between Line 1 and Line 3. These ABCD matrices are the result of multiplying three ABCD matrices together for each section of the line (as discussed earlier) where section 2 is the coupled line configuration and sections 1 and 3 are the lines in isolation. Once the cascaded ABCD matrices are calculated, each of these matrices is converted to a Y-matrix. The Y-matrices are added together to create a parallel configuration. This Y-matrix describing the multi-line transmission line is then converted to an ABCD matrix. This process is repeated for every length of line in the inductor. Then, all of the ABCD matrices for every length of line are multiplied together in the proper order to obtain a total ABCD matrix describing the inductor.

6.3 Calculation of Coupled Slotline Characteristics

To perform the calculations described above, the even and odd mode characteristic impedance and effective wavelengths must be known to properly describe the behavior of the coupled line. These quantities have been derived by Simons [18, 19]. The calculations are based upon Cohn's method [14],

which finds characteristic impedance and effective wavelength for a single slot. Cohn's method must be understood first before Simon's method is explained. Therefore, Cohn's method is outlined below.

Two images depicting the setup for Cohn's method are shown in Figure 6.4. In essence, Cohn places electric (or magnetic) walls through and around the slot to create a waveguide structure with the slotline as a capacitive iris in the waveguide [14]. Cohn derives the susceptance for both electric and magnetic walls and shows that the solutions converge. The walls perpendicular to the slot are placed a half-wavelength apart - which is the location of field nulls; therefore, they do not disturb the fields of the slot. The slot is shown with width w_s in Figure 6.4a. The walls parallel to the slot are placed symmetrically far enough apart from the slot to not affect the slot fields - this distance is b in Figure 6.4. This distance was found by Cohn to be approximately one wavelength [14]. The susceptance formula derived by Cohn is in terms of a, which is defined in the figure as the separation between the walls perpendicular to the slot. The total susceptance at the slot is derived as a sum of the susceptance looking into the dielectric below the slot (β_d) and looking into the air (β_a) as shown in Figure 6.4. When the susceptance that he derives for the capacitive iris is equal to zero, the slot is resonant according to the transverse resonance method. When the slot is resonant, a is equal to half of the effective wavelength [14]. We found the value of a through an optimization routine in Matlab minimizing the value of the susceptance at the slot. The iterative procedure is required since a cannot be solved for directly. An expression for the characteristic impedance of the slotline is also derived based upon an iterative procedure using the susceptance formula for the slot [14].

The fields for odd (a) and even (b) modes on the coupled slot are shown in Figure 6.5. For the odd mode, a magnetic wall can be placed halfway between the two slots. For the even mode, an electric wall can be placed halfway between the two slots.

Simons [18, 19] slightly alters the configuration of Cohn to derive the characteristic impedance and effective wavelength of the even and odd modes of a coupled slotline. His configuration is shown in Figure 6.6. Simons changed

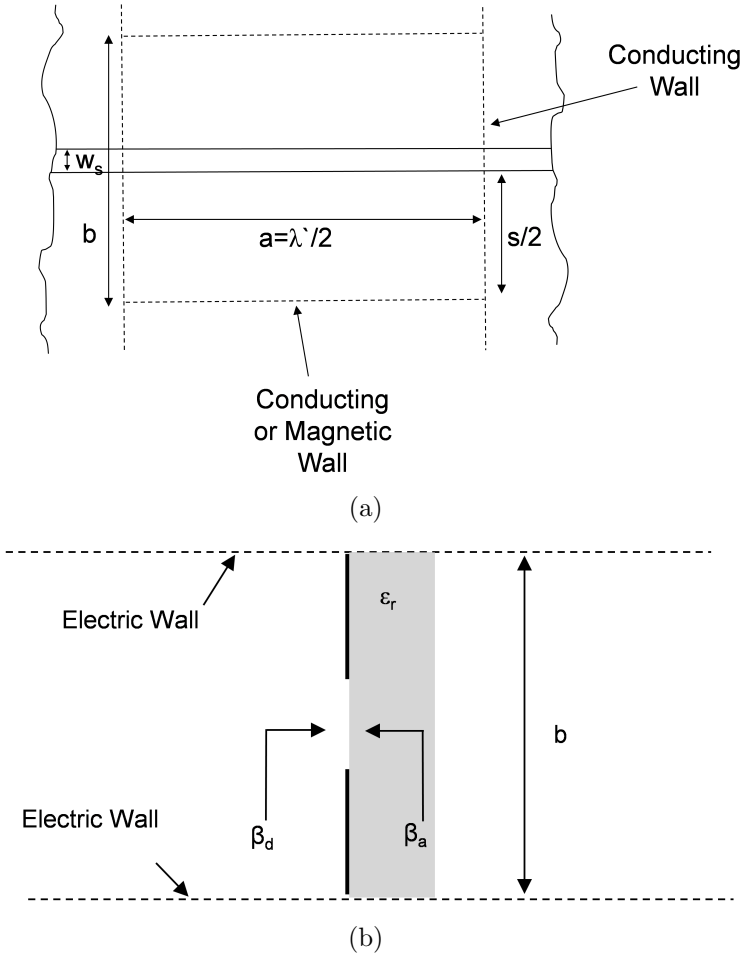

Figure 6.4: The setup Cohn [14] used to analyze the slotline including (a) Top view and (b) Side view.

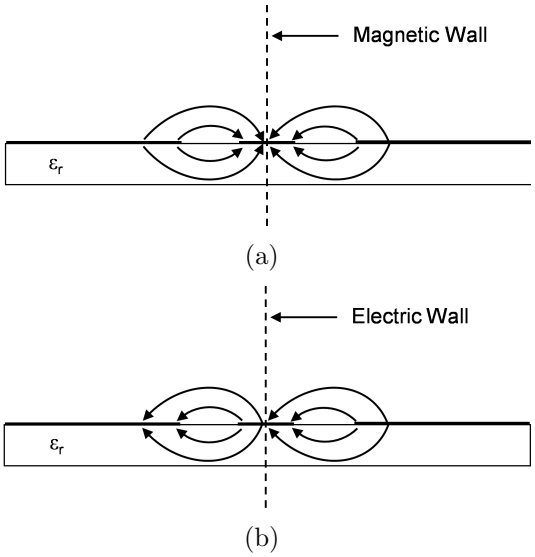

Figure 6.5: (a) Odd mode and (b) Even mode fields in a coupled slot configuration.

the setup of the walls parallel to the slotline to be asymmetric. Instead of being sufficiently far away to not disturb the fields, Simons sets one wall to be half of the distance (s) of the separation between the coupled slots. For the even mode, Simons derives the susceptance of the slot assuming the wall between the slots is magnetic. For the odd mode, the wall is set to be electric. The expressions that Cohn derived for effective wavelength and characteristic impedance can be used with the susceptance derived by Simons to find the even and odd mode characteristic impedance and effective wavelength. Setting up the problem in this manner allows one to find the characteristic impedance and effective wavelength of a slotline for a purely even or odd mode.

For the transmission line model of the slotline inductor, if the total length of the inductor (stretched out) is less than a quarter wavelength long, it is assumed that only the even mode exists. If the inductor length is between a quarter and a half wavelength, the odd mode is stepped in with frequency linearly such that by the time the inductor is a half-wavelength long, the assumed effective wavelength is the arithmetic average of the even and odd modes and the characteristic impedance is the geometric mean of the even

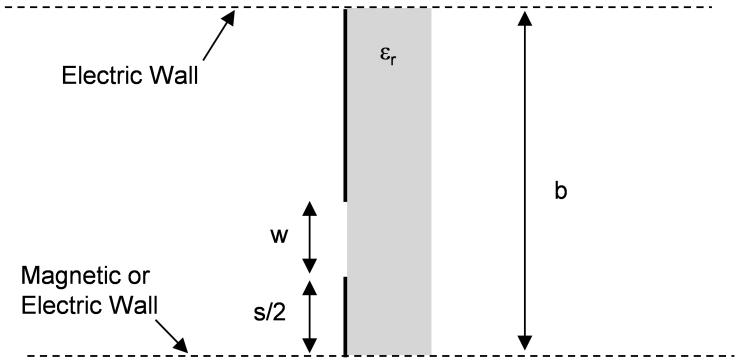

Figure 6.6: The setup Simons [18, 19] used to analyze the coupled slotline.

and odd mode characteristic impedance.

A transmission line model for the slotline inductor was developed using the methods outlined above. The results of this model are compared with simulated (HFSS) and measured results in the next section.

6.4 HFSS Simulation Setup

The setup for the simulation of the slotline inductor in HFSS is shown in Figure 6.7. Two slotline inductors are excited in parallel with a lumped port. The impedance of a single slotline inductor is found by multiplying the impedance at the lumped port by two and then de-embedding using transmission line equations to the input port of the slotline inductor.

6.5 Results Comparison

The results of the transmission line model of the slotline inductor compared with the HFSS simulation in the UHF band are shown in Figure 6.8. The dimensions of the inductor under consideration were: $L = 15$ mm, $W = 15$ mm, $w_s = 1$ mm, $h = 1.524$ mm, $\epsilon_r = 2.94$, $L_{ext} = 107.5$ mm. The dimensions not defined above are: h (height of substrate), ϵ_r (relative dielectric

(a)

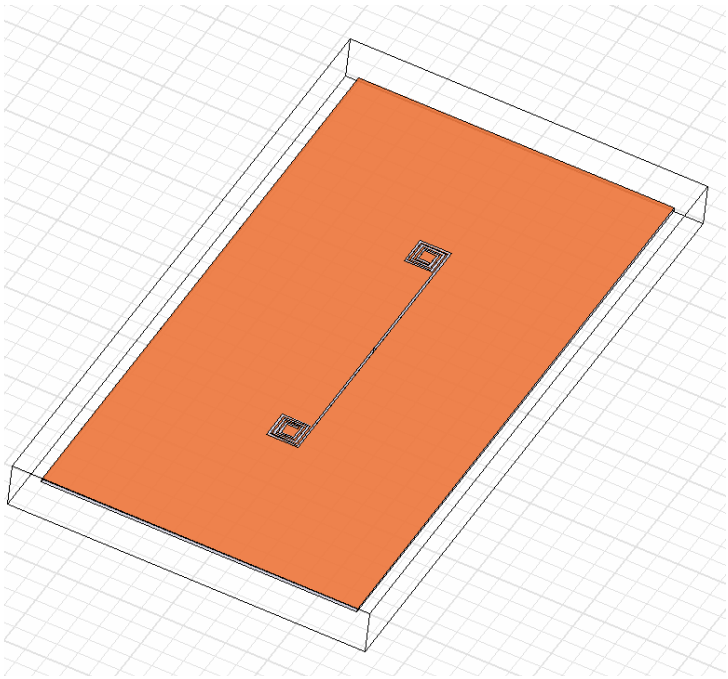

(b)

Figure 6.7: Simulation setup for the slotline inductor in HFSS. (a) Zoomed in, (b) Zoomed out. The inductors were simulated in parallel to avoid edge effects when the lumped port exciting the slotline was placed on the edge of a ground plane.

constant of substrate), and L_{ext} (length of transmission line to lumped port in simulation). The inductors were placed far apart in simulation to ensure that coupling effects between the inductors were not affecting the impedance at the lumped port. A comparison with the HFSS results de-embedded to the input port of the slotline inductor is shown in Figure 6.8(a). A comparison with the results from the HFSS simulation not de-embedded and the transmission line model extended by the necessary length of transmission line is shown in Figure 6.8(b). As can be seen in both figures, the model works well up to around 650 MHz or slightly above the first resonance of the structure in frequency. After this frequency, corner effects that are not taken into account in the model become important and the simulation results and transmission line model do not match as well.

The results of the transmission line model of the slotline inductor compared with the HFSS simulation in the X-band are shown in Figure 6.9. The dimensions are the same as the UHF band except for the length of the transmission line to the lumped port. L_{ext} is equal to 57.5 mm. As can be seen in the figure, the corner effects become important once the frequency reaches X-band. The amount of phase found for the slotline inductor at X-band is too large. This is due to the fact that at X-band the reactance due to the corners of the rectangular slotline inductor becomes so large that the reflections at each corner become significant. The reflections at the corners are so significant that the entire length of the slotline inductor is never "seen," resulting in the slotline inductor looking shorter than its actual physical length.

6.6 Antenna Measurement Results

A slot antenna was constructed with slotline inductors loading both ends. A picture of the constructed antenna is shown in Figure 6.10. The dimensions of the slotline inductor are identical to the dimensions discussed earlier except for the transmission line extension: $L = 15$ mm, $W = 15$ mm, $w_s = 1$ mm, $h = 1.524$ mm, $\epsilon_r = 2.94$, $L_{ext} = 2$ mm. The extension was large enough that

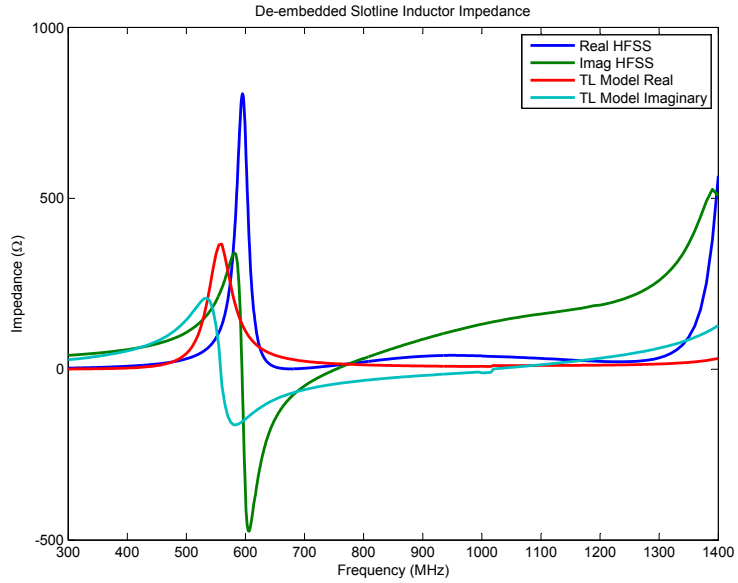

(a)

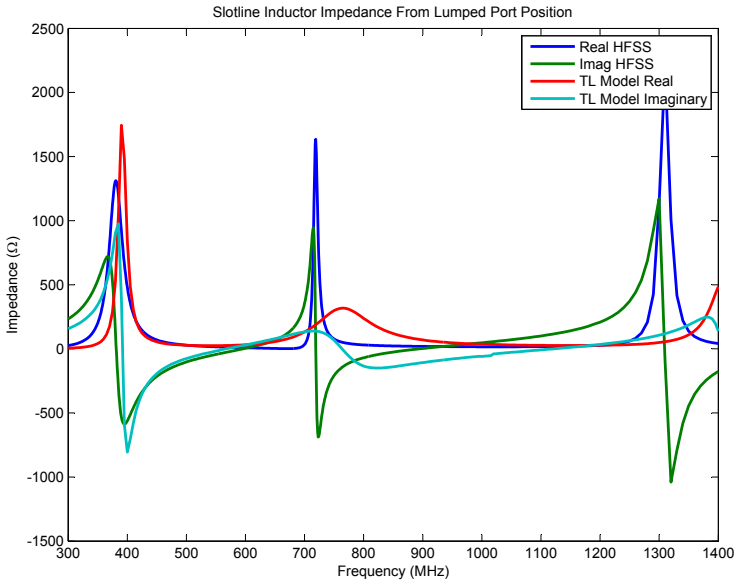

(b)

Figure 6.8: Comparison of transmission line model versus HFSS for slotline inductor impedance at UHF band. (a) De-embedded to input port of slotline inductor, (b) From lumped port position in HFSS simulation.

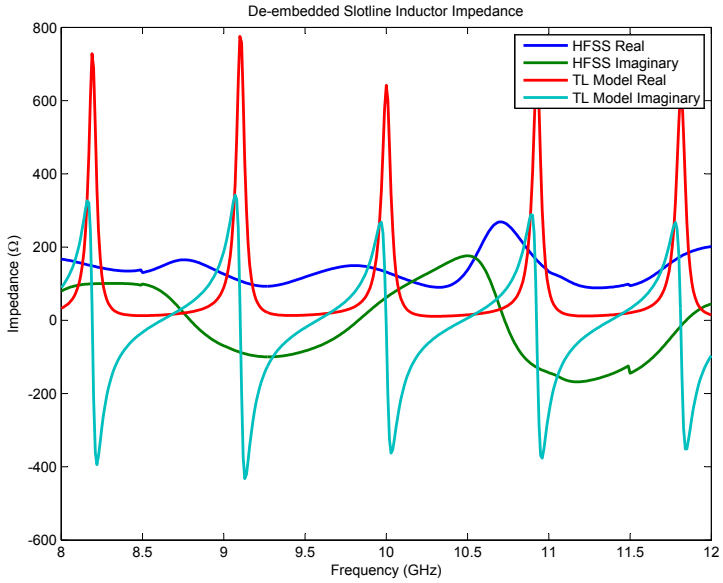

(a)

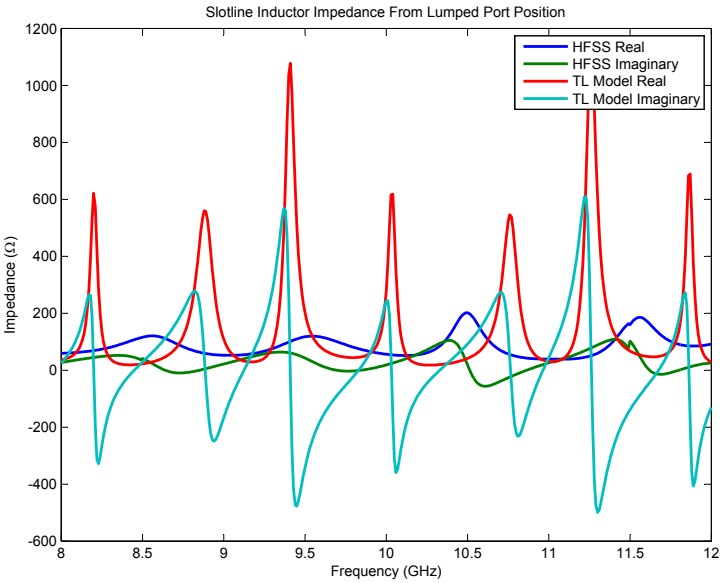

(b)

Figure 6.9: Slotline inductor impedance at X-band for transmission line model versus HFSS. (a) De-embedded to input port of slotline inductor, (b) From lumped port position in HFSS simulation.

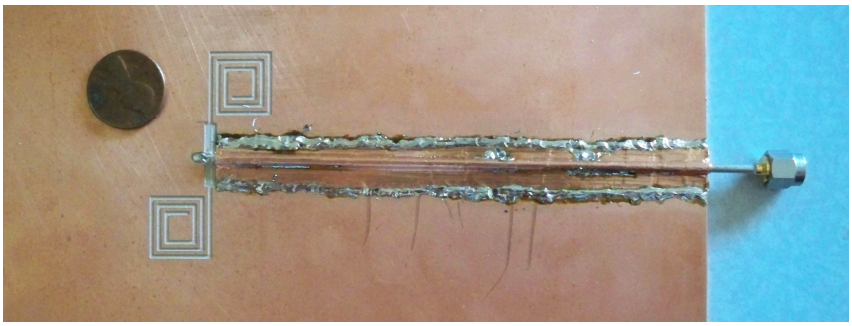

Figure 6.10: Photograph of constructed and measured slot antenna. A penny is placed next to the antenna to show size. The ground plane is larger than what is shown; the picture is zoomed in to show detail. The ground plane is 30 mm by 20 mm.

the inductors do not couple significantly. The slot that is fed connecting the two slotline inductors has dimensions $w_a = 3$ mm (width of slot), $L_a = 15$ mm (length of slot). The slot is fed at the center.

The measured results were compared to the transmission line model and the HFSS simulation. This comparison is shown in Figure 6.11. As can be seen in the figure, both the transmission line model and the HFSS simulation predict a lower frequency response than what is measured. This was thought to be due to the fact that the impedance of the coaxial probe is neglected. However, a model by Knorr [20] for the coaxial probe was included in the extraction and the frequency of the measured results was still approximately 100 MHz higher than the simulated results. Also, the response of the transmission line model is much smaller in magnitude than either the simulation or measured results. This is due to the fact that the transmission line model calculates the attenuation constant α as defined in Equation 4.2 for the slotline assuming the line is straight. Since the line is not straight but in fact coiled in the inductor, this assumption overestimates the attenuation constant.

The same antenna shown in Figure 6.10 was measured and simulated at X-band. The results of the analysis are shown in Figure 6.12. As can be seen in the figure, the measured and simulated results do not match well. It appears that the simulation may overestimate the effects of the corners in the slotline

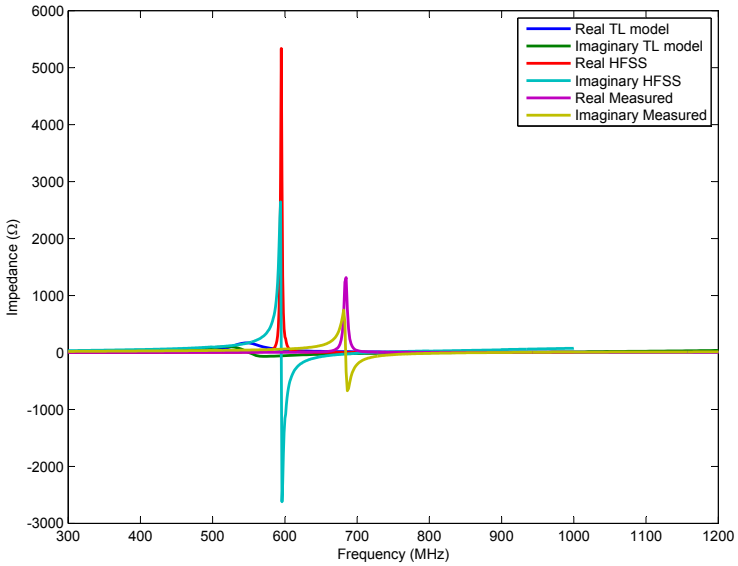

(a)

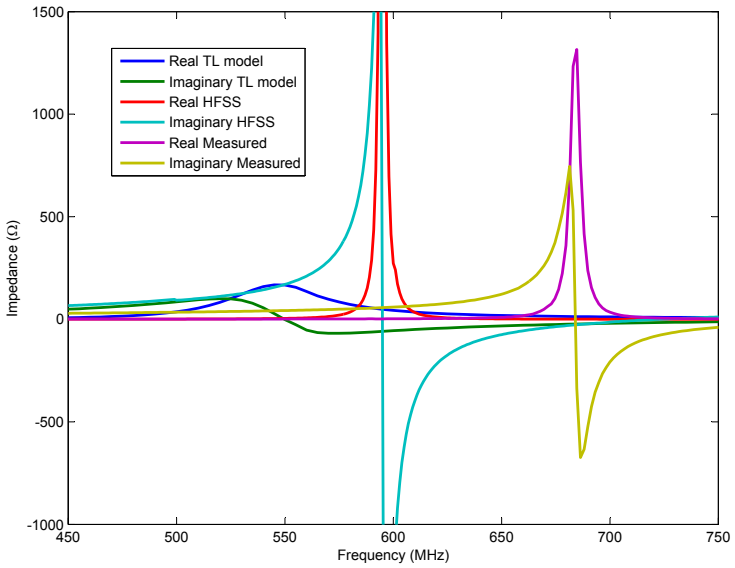

(b)

Figure 6.11: Input impedances found using transmission line model, HFSS, and measured results. (a) Zoomed out, (b) Zoomed in.

inductor. The measured results show more phase and less radiation than the simulated results. The transmission line model does not match well with either the measured or simulated results and again this is likely due to a neglect of the corners in the rectangular slotline inductor. The transmission line model shows more electrical length than what was found through measurements.

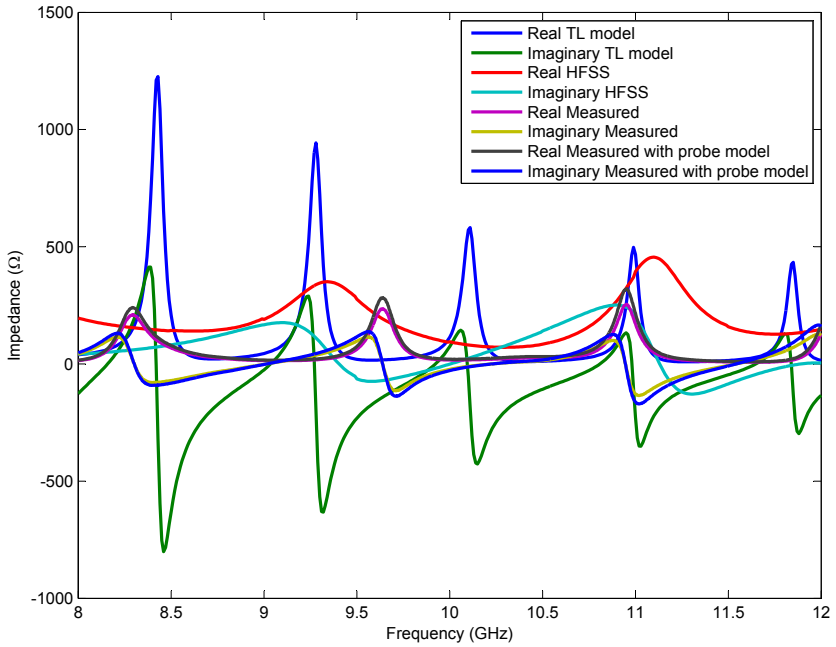

Figure 6.12: Impedance of antenna at X-band. Measured, simulated, and model results are shown. The measured results are shown with and without the model for the coaxial probe.

6.7 Conclusions

A transmission line model for a rectangular slotline inductor was developed to aid in the design of the miniaturized and dual-band slot antenna. This model is relatively accurate at low frequencies. However, at high frequencies, corner effects become important and the model no longer matches well. The slotline inductor model was incorporated into the transmission line model for the slot

antenna. The transmission line model with the slotline inductor model predicted resonant frequency within 50 MHz, but the magnitude of the predicted response was incorrect. This was largely because the model assumes the slot is straight to predict the attenuation constant of the slotline. Since the effects of corners become more prominent as frequency increases, a circular slotline inductor was investigated and will be discussed in Chapter 7.

CHAPTER 7

TRANSMISSION LINE MODEL OF ARCHIMEDEAN SPIRAL SLOT

7.1 Introduction

Slot spiral structures appear in many applications, including a circuit element in a three-dimensional filter in [21] and a broadband antenna in [22]. However, the design methodologies for the structure are currently limited to a full-wave solver or simple design equations that are only applicable when the structure is electrically very large. An Archimedean spiral structure as shown in Figure 7.1 is, in effect, a multi-line transmission line connected end-to-beginning at each turn. Multi-line characteristics are difficult to compute, requiring computationally expensive methods. The method presented in this work to characterize an Archimedean spiral structure uses singly coupled slotline characteristics to approximate the coupling effect in a multi-line transmission line. This method is similiar to that detailed in the last chapter for the rectangular spiral inductor.

This chapter begins with a presentation of the transmission line model for the Archimedean spiral structure. Section 7.3 discusses the transverse resonance method used to calculate the conductance-per-unit-length of the spiral. Section 7.4 presents measured results for a particular application of the spiral slot structure - an end-loaded slot antenna. The chapter closes with conclusions about the model along with implications and applications of the work.

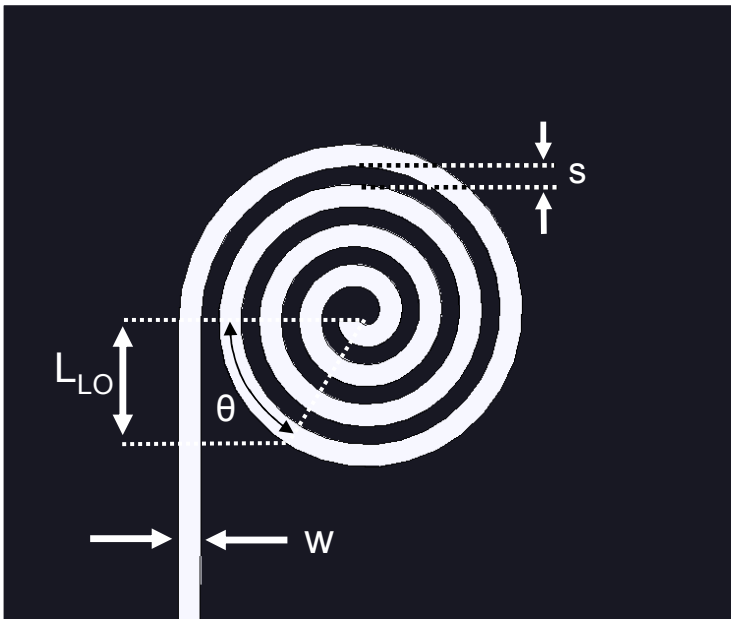

Figure 7.1: Circular slotline inductor with dimensions labeled.

7.2 Transmission Line Model

The transmission line model of the slot spiral structure uses an algorithm with multiple iterations. The first iteration uses a simplified model of a coupled line that does not attempt to compute power coupled between the lines. The higher-order iterations use a more complex model of the coupled lines that better approximates the coupling behavior at higher frequencies.

7.2.1 Two-Port Model for First Iteration

The first iteration of the transmission line model follows the method outlined by Shepherd in [17] to approximate multi-line behavior using singly coupled line characteristics. However, there are necessarily some differences since the model described by Shepherd is for a rectangular spiral inductor. Shepherd's model breaks the inductor into the four sections delineated by the corners of the inductor. For each section of spiral the ABCD matrix for each coupled

line configuration is found where the ABCD matrix is

$$\begin{bmatrix} A & B \\ C & D \end{bmatrix} = \begin{bmatrix} \cosh(\gamma l) & Z_c \sinh(\gamma l) \\ \frac{1}{Z_c}\sinh(\gamma l) & \cosh(\gamma l) \end{bmatrix}$$

and where

$$Z_c = \sqrt{Z_{0e} Z_{0o}} \tag{7.1}$$

also

$$\lambda = \frac{\lambda_e + \lambda_o}{2} \tag{7.2}$$

and

$$\gamma = \alpha + j\frac{2\pi}{\lambda} \tag{7.3}$$

with Z_c being the characteristic impedance of the slotline, and Z_{0e} and Z_{0o} the even and odd mode characteristic impedance, respectively.

Shepherd's model uses an attentuation per-unit-length, α, included in the propagation constant γ to represent the losses in the spiral. This is only correct for the low-loss condition. For the transmission line model discussed in this chapter, a conductance-per-unit-length, G, will be used to represent the radiative losses in the spiral so that the model accounts for the frequency shift that results from the losses and will remain accurate as frequency increases and the slot structure becomes electrically large. The characteristics Z_{0e}, Z_{0o}, β_e, and β_o can be found from Simon's method [18, 19]. To use a conductance, G, to represent radiative losses, the following equations from the definition of a coupled line in [23] should be used for the characteristics of the coupled slotline: the propagation constant

$$\gamma = \frac{\gamma_e + \gamma_o}{2} \tag{7.4}$$

the lossy even-mode characteristic impedance

$$Z_{0e}^{lossy} = \sqrt{\frac{j\omega(L + L_m)}{(G + j\omega(C - C_m))}} \tag{7.5}$$

the lossy odd-mode characteristic impedance

$$Z_{0o}^{lossy} = \sqrt{\frac{j\omega(L - L_m)}{(G + j\omega(C + C_m))}} \tag{7.6}$$

the lossy even-mode propagation constant

$$\gamma_e = \sqrt{j\omega(L + L_m)(G + j\omega(C - C_m))} \tag{7.7}$$

the lossy odd-mode propagation constant

$$\gamma_o = \sqrt{j\omega(L - L_m)(G + j\omega(C + C_m))} \tag{7.8}$$

with the inductance per-unit-length

$$L = \frac{1}{2\omega}\left(\beta_e Z_{0e} + \beta_o Z_{0o}\right) \tag{7.9}$$

the coupling inductance

$$L_m = \frac{1}{2\omega}\left(\beta_e Z_{0e} - \beta_o Z_{0o}\right) \tag{7.10}$$

the capacitance per-unit-length

$$C = \frac{1}{2\omega}\left(\frac{\beta_o}{Z_{0o}} + \frac{\beta_e}{Z_{0e}}\right) \tag{7.11}$$

and the coupling capacitance

$$C_m = \frac{1}{2\omega}\left(\frac{\beta_o}{Z_{0o}} - \frac{\beta_e}{Z_{0e}}\right) \tag{7.12}$$

In Shepherd's [17] model, the ABCD matrices for each section and coupling configuration are converted to Y-matrices and added together to represent the lines being approximately in parallel. The ABCD matrices for each section can then be multiplied in the correct order to find a single matrix representing the behavior of the inductor.

The square spiral inductor model analyzed one side of the inductor at a time. The circular spiral inductor analyzes five degrees in the geometrical dimension θ at a time where θ is denoted in Figure 7.1. For every five degrees in θ of the spiral, an ABCD matrix is found for each coupling configuration. This resolution in θ was chosen so that the voltage distribution at the high end of the frequency range of interest was continuous. Once these ABCD matrices are found, they are converted to Y-matrices and simply added together. This total Y-matrix is converted to an ABCD matrix. An ABCD matrix is thus found for every five degrees of the circular spiral inductor. These are multiplied in order to arrive at a total ABCD matrix to represent the behavior of the entire inductor. The length of line for each degree is found using the standard formula for arc-length in an Archimedean spiral. The arc length is found for the arc one-third of the distance between the inner curve and outer curve of the spiral. This estimation for the arc length was chosen to approximate the tendency of the fields in the spiral to crowd toward the center. The length of line for each section is assumed to be the average length between the primary and secondary line for each coupling configuration.

The method for the first iteration of the transmission line model is relatively accurate at low frequencies - for the first three resonances of the spiral structure. Below the first resonance, the even-mode dominates and coupling between lines is therefore negligible:

$$Z_c = Z_{0e}^{lossy} \tag{7.13}$$

and

$$\gamma = \gamma_e \tag{7.14}$$

At higher frequencies, the first iteration method becomes inaccurate and further iterations are necessary as described in the next section.

7.2.2 Conversion of Four-Port Network to Two-Port Network

The model described for the first iteration made assumptions regarding the coupling behavior in the spiral. It was assumed that the characteristic impedance was the geometric mean of the even and odd mode characteristic impedances and the effective wavelength was the arithmetic mean of the even and odd mode effective wavelengths. The power that is coupled between turns of the spiral was also not considered. The iterations of the transmission line model past the first do not have to make these assumptions.

The four-port model of a coupled line can be described completely by the following impedance parameters [24]:

$$\begin{aligned} Z_{11} &= Z_{22} = Z_{33} = Z_{44} \\ &= \frac{1}{2}(Z_{0e}^{lossy}\coth(\gamma_e l) + Z_{0o}^{lossy}\coth(\gamma_o l)) \end{aligned} \tag{7.15}$$

$$\begin{aligned} Z_{12} &= Z_{21} = Z_{34} = Z_{43} \\ &= \frac{1}{2}(Z_{0e}^{lossy}\coth(\gamma_e l) - Z_{0o}^{lossy}\coth(\gamma_o l)) \end{aligned} \tag{7.16}$$

$$\begin{aligned} Z_{13} &= Z_{31} = Z_{24} = Z_{42} \\ &= \frac{1}{2}(Z_{0e}^{lossy}\coth(\gamma_e l) - Z_{0o}^{lossy}\mathrm{csch}(\gamma_o l)) \end{aligned} \tag{7.17}$$

$$\begin{aligned} Z_{14} &= Z_{41} = Z_{23} = Z_{32} \\ &= \frac{1}{2}(Z_{0e}^{lossy}\coth(\gamma_e l) + Z_{0o}^{lossy}\mathrm{csch}(\gamma_o l)) \end{aligned} \tag{7.18}$$

where the ports for the coupled line are as labeled in small numbers in Figure 7.2. For iterations past the first, this four-port model can be used instead of the two-port since an estimation of the impedance looking toward the short Z_L and the impedance looking toward the source Z_S is known. To find the impedance looking toward the source, a source impedance must be assumed. However, the choice for this source impedance is unimportant as long as extreme values such as zero or one million are not used. Z_S and Z_L are labeled on the spiral in Figure 7.3 and on the four-port coupled line in Figure 7.2.

A two-port representation of each coupled line configuration can be found

Figure 7.2: The loading condition to convert the four-port coupled line model into a two-port network.

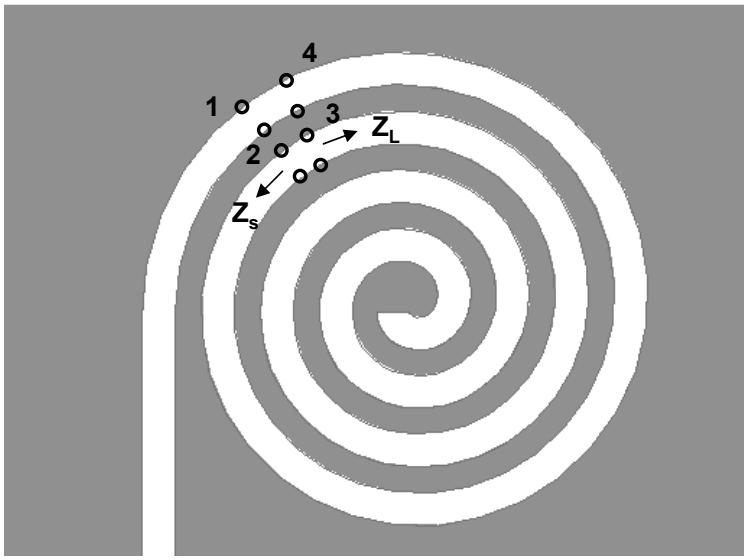

Figure 7.3: The loading condition to use the four-port coupled line model for the spiral structure.

by loading the four-port model appropriately. Once the two-port model is found, the same method that is used for the first iteration can be employed to effectively describe the multi-line behavior. The two-port network parameters are converted to Y-parameters and added together. Again, an ABCD matrix can be found describing every five degrees of the spiral. These matrices can be multiplied together in the correct order to arrive at an ABCD matrix describing the behavior of the total spiral. Iterations using the four-port model should continue until the input impedance looking into the spiral, power delivered to the spiral, and the voltage along the spiral converge. The method for finding the power delivered to and voltage of the spiral will be described later in the chapter.

7.2.3 Structure Lead-Out

The coupling effects in the lead-out section of slotline (labeled L_{Lo} in Figure 7.1) are accounted for in the transmission line model. The coupling effects are assumed to be negligible after the angle labeled θ in Figure 7.1 is equal to 60^o. At this point the fields inside the spiral are pointing more perpendicular than parallel to the fields in the feeding slotline. The same method that was presented earlier to account for coupling in the spiral can be used in the lead-out section of line. However, for the lead-out section, the coupled-line characteristics need to be recalculated periodically since the separation between slotlines changes. For this model, the coupled line characteristics were recalculated for every five degrees of the spiral in the lead-out section.

The results in this chapter show the lead-out section of line in two different configurations. The lead-out section can remain the same width as the spiral, as shown in Figure 7.1, or it can expand in width to allow for a wider input feedline as shown later. The analysis method holds for either configuration.

7.3 Conductance Calculation

The conductance per-unit-length of the spiral that represents the loss due to radiation can be found by determining the conductance per-unit-length for which the power radiated by the spiral is equal to the power delivered to the spiral. The power radiated can be found analytically from the electric field formed on the spiral. The power delivered to the spiral can be found using the network parameters describing the spiral. This method is similar in approach to the method described by the authors in [12] who approximated losses in a half-wavelength slot antenna and was used in previous chapters.

7.3.1 Power Radiated

The total power radiated by the Archimedean slot spiral structure can be found analytically. From the transmission line model, the network parameters for every five degrees of the spiral are known. From these network parameters the voltage along the line can be found using the formula for voltage gain, A_V, given below [25]:

$$A_V = \frac{Z_{21}Z_L}{Z_{11}Z_L + Z_{11}Z_{22} - Z_{12}Z_{21}} \tag{7.19}$$

The formula is given for Z-parameters; the known ABCD parameters of the spiral can be converted to Z-parameters to use the given formula or vice versa. The starting voltage for the spiral structure is known at the input to be

$$V_0 = \frac{V_g Z_{in}}{Z_0 + Z_{in}} \tag{7.20}$$

where V_g is the generator voltage. Since the input voltage and the network parameters for every five degrees of the spiral are known, the voltage along the spiral can be found. The electric field on the aperture of the spiral structure can be found by simply dividing the known voltage by the width of the slot. This electric field can be assumed to be pointing only in the radial direction and constant across the slot as shown below:

$$E_\rho = \frac{V_\rho}{w_s} \tag{7.21}$$

A magnetic current can be found by the equivalence theorem [13] that represents the electric field and is described by

$$M_\phi = -2\hat{z} \times E_\rho \tag{7.22}$$

From the magnetic current, the far-field vector potentials are

$$L_\theta = \iint_S (M_\phi \cos(\theta) \sin(\phi - \phi')) e^{jkr' \cos(\psi)} dS' \tag{7.23}$$

$$L_\phi = \iint_S (M_\phi \cos(\phi - \phi')) e^{jkr' \cos(\psi)} dS' \tag{7.24}$$

where

$$r' \cos(\psi) = \rho' \sin(\theta) \cos(\phi - \phi') \tag{7.25}$$

Both polarizations of the electric field are

$$E_\theta = \frac{-jke^{-jkr}}{4\pi r} L_\phi \tag{7.26}$$

$$E_\phi = \frac{jke^{-jkr}}{4\pi r} L_\theta \tag{7.27}$$

and the total power radiated can then be found by integrating the Poynting vector as shown below:

$$P_r = \frac{\zeta}{2\eta} \iint_S \Re(|E_\theta|^2 + |E_\phi|^2) dS \tag{7.28}$$

where

$$\zeta = 1 + \frac{1}{\epsilon_r}. \tag{7.29}$$

and the surface of integration is a hemisphere covering the top of the spiral structure. All of the integrations can be carried out numerically for this model.

7.3.2 Power Delivered

The power delivered to the spiral could be calculated by

$$P_d = \frac{1}{2} \mid V_0 \mid^2 \Re\left(\frac{1}{Z_{in}}\right) - P_{source} \tag{7.30}$$

where the input voltage V_0 has been described in Equation 7.20, Z_{in} is the input impedance of the spiral structure, and P_{source} is the power delivered back to the source due to coupling in the spiral. However, a simpler method is to estimate the power delivered to each segment of transmission line. The voltage along the line has already been calculated to obtain the power delivered by the structure. Since the voltage along the spiral is found at such a high resolution, the total power delivered can be estimated for every five degrees of the spiral to be

$$P_d = \frac{1}{2} \mid V \mid^2 G\Delta z \tag{7.31}$$

where V is the voltage for the segment, G is the conductance per-unit-length, and Δz is the length of transmission line for said segment. The total power delivered is then just the sum of the power delivered to all segments. The appropriate conductance can be easily found due to its linear relationship with the conductance per-unit-length. The power delivered and power radiated are computed for two different conductances. From this information, the linear functions of the power delivered and power radiated with conductance can be determined. Then, the intersection of the lines of the power radiated and delivered determines the correct conductance to represent the radiation from the structure.

7.4 End-Loaded Slot Antenna

The Archimedean slot spiral structure was used to end-load a slot antenna for the purpose of miniaturization. End-loading has long been used as a miniaturization method - the original Hertzian dipole was a dipole end-loaded with

metallic spheres [26]. The method has been used more recently in a slot structure by the authors in [27].

7.4.1 Transmission Line Model of End-Loaded Slot

To determine the impedance of an arbitrarily loaded slot, further analysis is required for the central slot that is loaded by the slotline inductors. The analysis must begin with a determination of the voltage on the central slot. This voltage can be determined by a method similiar to that employed in Chapter 5. An arbitrarily loaded slot can be represented in transmission line as shown in Figure 7.4.

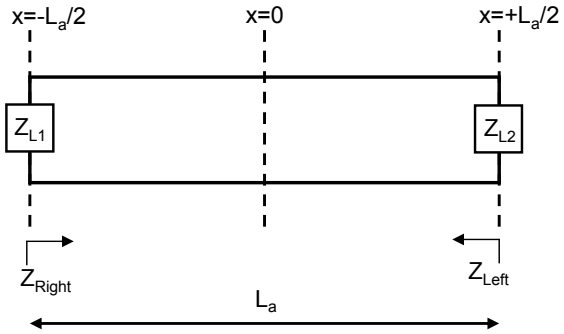

Figure 7.4: Depiction of an arbitrarily loaded slot transmission line.

The voltage within the central slot can be represented as

$$V(x) = A\left(e^{-\gamma_m x} + \frac{B}{A}e^{\gamma_m x}\right) \tag{7.32}$$

where γ_m, the propagation constant, and $\frac{B}{A}$, the voltage reflection coefficient, are modal in nature. The current at any point in the slot can also be described as

$$I(x) = \frac{A}{Z_c^{lossy}}(e^{-\gamma_m x} - \frac{B}{A}e^{\gamma_m x}) \tag{7.33}$$

where Z_c^{lossy} is the characteristic impedance of the slotline when radiative losses

are accounted for. The impedance at any point in the slot can be described as

$$Z(x) = \frac{V(x)}{I(x)} \tag{7.34}$$

The impedance at the loads of the slot can be described as

$$Z\left(x = \frac{-L_a}{2}\right) = \frac{Z_{L1} Z_{Right}}{Z_{L1} + Z_{Right}} \tag{7.35}$$

and

$$Z\left(x = \frac{+L_a}{2}\right) = \frac{Z_{L2} Z_{Left}}{Z_{L2} + Z_{Left}} \tag{7.36}$$

where

$$Z_{Right} = Z_c \frac{Z_{L2} + Z_c^{lossy} \tanh(\gamma_S L_a)}{Z_c^{lossy} + Z_{L2} \tanh(\gamma_S L_a)} \tag{7.37}$$

and

$$Z_{Left} = Z_c \frac{Z_{L1} + Z_c^{lossy} \tanh(\gamma_S L_a)}{Z_c^{lossy} + Z_{L1} \tanh(\gamma_S L_a)} \tag{7.38}$$

where γ_S is the propagation constant for the central slot and will be defined later. Given the above boundary conditions for the impedance, γ_m and $\frac{B}{A}$ can be solved to be

$$\gamma_m = 2m \ln \frac{j \left(\frac{X}{Y}\right)^{1/4}}{L_a} \tag{7.39}$$

where

$$\begin{aligned} X =& [Z_{L1} (Z_{L2} + Z_c) + Z_{L2} Z_c + \tanh (L_a \gamma) \left(Z_c^2 + Z_{L1}(Z_{L2} + Z_c)\right)] \\ & * [Z_{L1}(Z_c - Z_{L2}) + Z_{L2} Z_c + \tanh (L_a \gamma) \left(Z_c^2 + Z_{L1} Z_{L2} - Z_{L2} Z_c\right)] \end{aligned} \tag{7.40}$$

$$\begin{aligned} Y =& [Z_{L1}(Z_c - Z_{L2}) + Z_{L2} Z_c + \tanh (L_a \gamma) \left(Z_c^2 + Z_{L1}(Z_{L2} - Z_c)\right)] \\ & * [Z_{L1}(Z_{L2} + Z_c) + Z_{L2} Z_c + \tanh (L_a \gamma) \left(Z_c^2 + Z_{L1} Z_{L2} + Z_{L2} Z_c\right)] \end{aligned} \tag{7.41}$$

Also,

$$\frac{B}{A} = -\frac{H \left[j \left(\frac{X}{Y}\right)^{1/4}\right]^{2m}}{Q} \tag{7.42}$$

where

$$H = Z_{L1}(Z_c - Z_{L2}) + Z_{L2}Z_c + \tanh(L_a\gamma)\left(Z_c^2 + Z_{L1}(Z_{L2} - Z_c)\right) \tag{7.43}$$

$$Q = Z_{L1}(Z_{L2} + Z_c) + Z_{L2}Z_c + \tanh(L_a\gamma)\left(Z_c^2 + Z_{L1}(Z_{L2} + Z_c)\right) \tag{7.44}$$

The voltage within the slot can then be described as a sum of all possible modes present with appropriate weighting conditions as

$$V(x) = A\sum_{m=1}^{\infty} A_m\left(e^{-\gamma_m x} + \frac{B}{A}e^{\gamma_m x}\right) \tag{7.45}$$

where

$$A_m = \frac{1}{(1 - \mid(\gamma_m - \gamma_S)\mid^2)} \tag{7.46}$$

Similiar to the spiral, a conductance per-unit-length is used to represent the losses in the central slot. Therefore,

$$\gamma_S = \sqrt{j\omega L(G + j\omega C)} \tag{7.47}$$

and

$$Z_c^{lossy} = \sqrt{\frac{j\omega L}{(G + j\omega(C))}} \tag{7.48}$$

where

$$L = \frac{1}{2\omega}(\beta Z_c) \tag{7.49}$$

and

$$C = \frac{1}{2\omega}\left(\frac{\beta}{Z_c}\right) \tag{7.50}$$

The lossless characteristic impedance, Z_c, and effective wavelength, λ, for the central slot can be found using Cohn's method [14].

The amplitude of the voltage in the slot can be found by the following expression

$$A = \frac{V_0}{\sum_{m=1}^{\infty} A_m(1 + \frac{B}{A})} \tag{7.51}$$

where

$$V_0 = \frac{V_g Z_{in}}{Z_{in} + Z_0} \tag{7.52}$$

where V_g and Z_0 are the generator voltage and impedance, respectively. The power radiated and power delivered for the slot can be found as desribed in Chapter 5 and equated to determine the conductance of the central slot, G.

7.4.2 Results

The transmission line model for the spiral was used to design three antennas with first resonances equally spaced between 400 and 700 MHz. The number of turns was varied between four and seven, and the separation, s, was varied between 0.73 mm and 1.1 mm. The antennas were etched on boards of length and width equal to 30 cm and 20 cm, respectively. The antennas were fed with a gap source created by soldering the inner pin of semi-rigid coaxial cable to one side of the slot and the outer conductor to the other as shown in Figure 7.5. The semi-rigid coax was 200 mm in length and was soldered to the ground plane of the slot antenna, creating a Dyson-like balun [16]. Soldering the coaxial cable to the ground plane causes the currents that are reflected back from the feed point to flow to the ground plane and feed the slot, thus balancing the currents. In Chapter 5 the results from two simulations were compared, one straight slot fed with a lumped port and another fed with a gap feed from coaxial cable, and the parameters of the cable-slot transition were determined to be negligible at low frequencies, adding only a small inductance to the impedance of the slot as frequency increased.

Figures 7.6, 7.7, and 7.8 compare the simulated, measured, and transmission-line-model-predicted results for three different miniatuized slot antennas. As can be seen in the figures, the transmission line model can fairly accurately predict the resonant frequencies of the miniaturized slot antenna. However, the magnitude of the impedance predicted by the transmission line model is inaccurate. As expected, this inaccuracy increases with the number of turns in the spiral. This is likely due to an overestimation of the coupling and loss

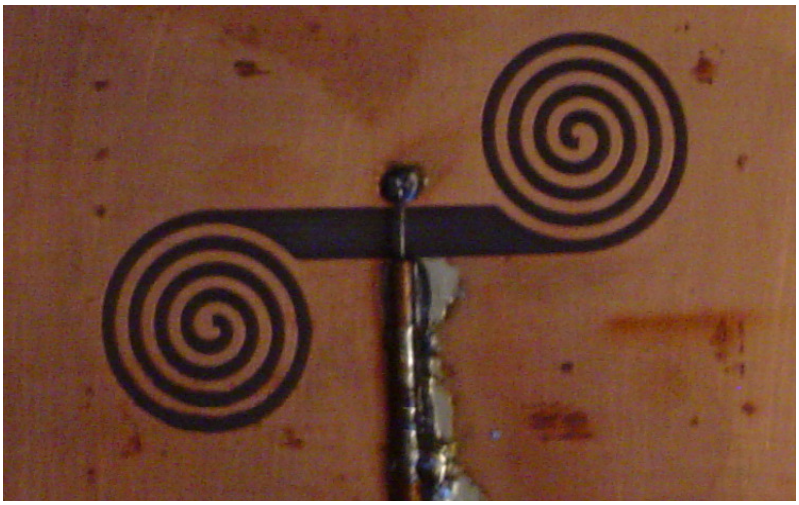

Figure 7.5: Picture of constructed end-loaded slot antenna fed with a gap source using semi-rigid coaxial cable.

in the transmission line model of the spiral structure. The resonant frequency of the second anti-resonance is also inaccurate due to the fact that the even mode again becomes more dominant due to a larger probability of the even mode field configuration. This condition is similiar to that below the first anti-resonance; however, it is not as easily corrected since the even mode cannot be assumed to be completely dominant. After the frequencies displayed in the plots in Figures 7.6, 7.7, and 7.8, the transmission line model ceases to converge. This occurs after the sixth or seventh anti-resonance of the spiral structure. The non-convergence effects can be seen at approximately 3.6 GHz for the six-turn spiral loaded slot antenna whose impedance characteristics are displayed in Figure 7.8.

The results of the transmission line model versus those of the first iteration of the transmission line model are compared in Figure 7.9 with the simulated and measured results for the miniaturized slot antenna with four-turn spiral loads. As can be seen in the figure, the first iteration is accurate for the prediction of the first three resonances of the structure but decreases in accuracy with increasing frequency. The first iteration of the transmission line model also underestimates the loss and coupling in the structure - predicting an

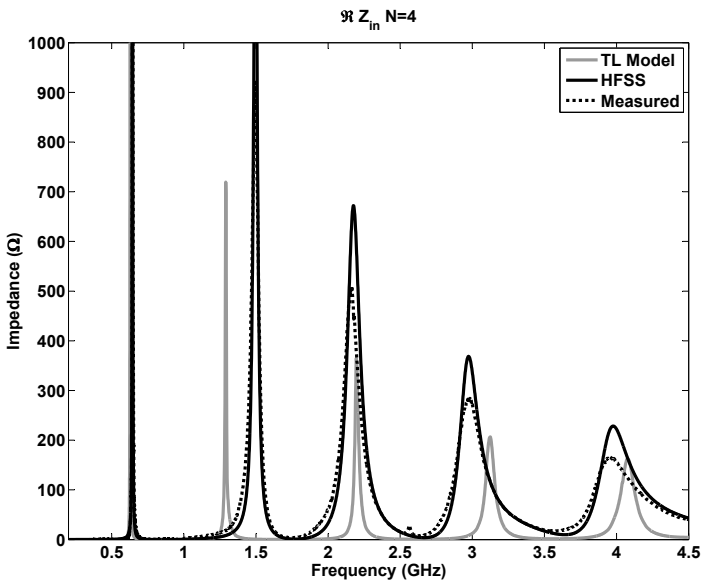

(a)

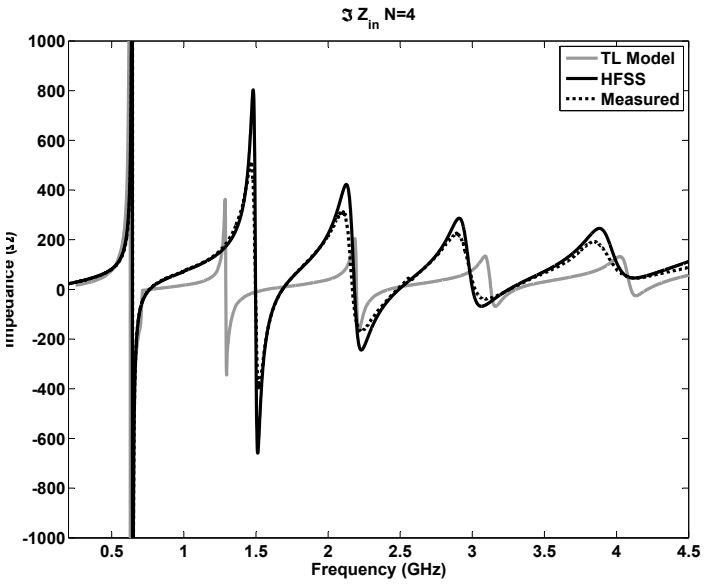

(b)

Figure 7.6: Measured, simulated, and transmission line model results of impedances of end-loaded slot antennas for a four-turn spiral (N=4) and s=1.1 mm. (a) Real part and (b) Imaginary part of input impedance of miniaturized slot antenna constructed using Rogers RO 4230 substrate with a height of 0.762 mm.

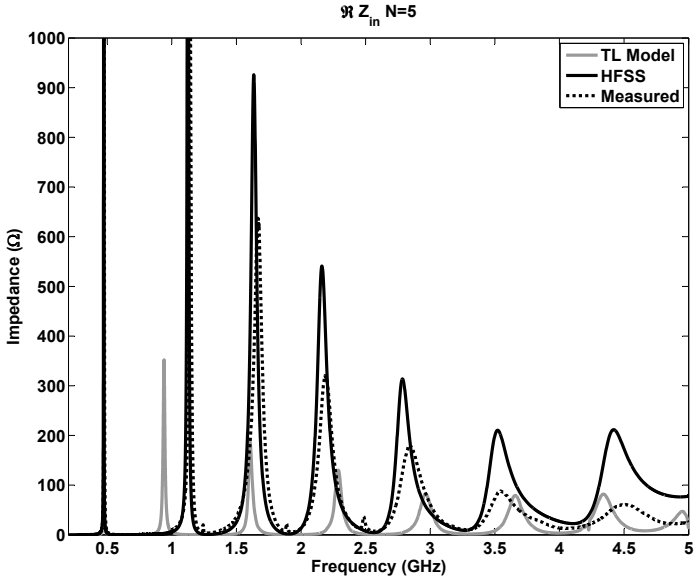

(a)

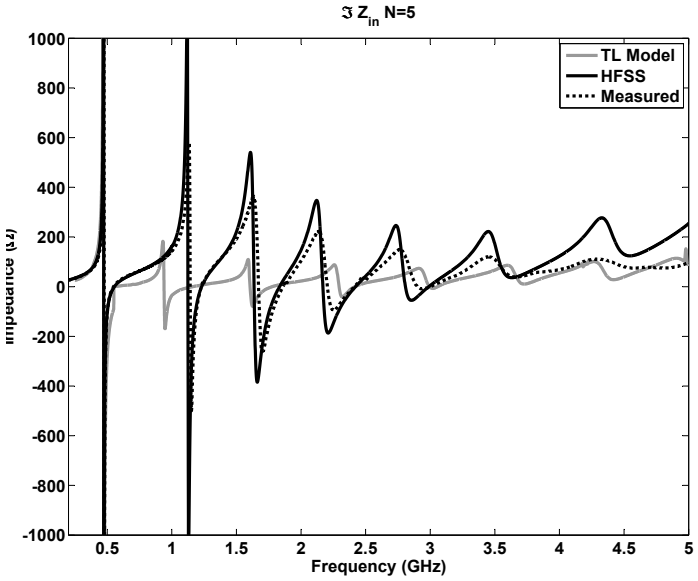

(b)

Figure 7.7: Measured, simulated, and transmission line model results of impedances of end-loaded slot antennas for a five-turn spiral (N=5) and s=0.9153 mm. (a) Real part, (b) Imaginary part of input impedance constructed using Rogers RO 4230 substrate with a height of 0.762 mm.

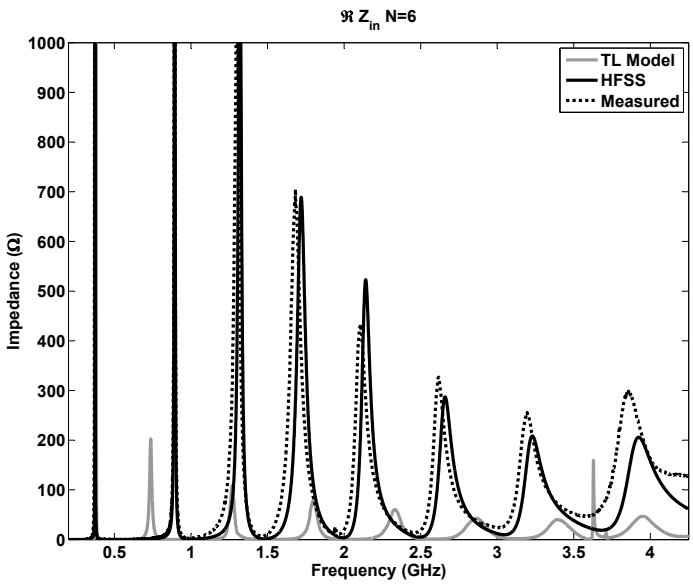

(a)

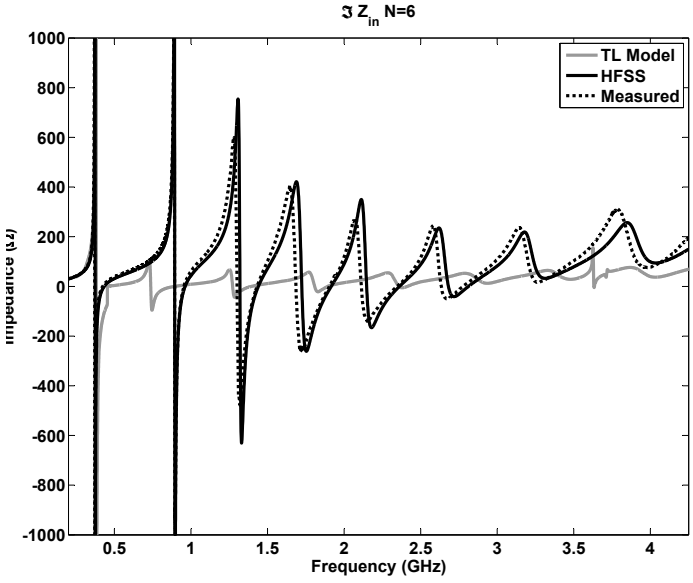

(b)

Figure 7.8: Measured, simulated, and transmission line model results of impedances of end-loaded slot antennas for a six-turn spiral (N=6) and s=0.73 mm. (a) Real part, (b) Imaginary part of input impedance of miniaturized slot antenna constructed using Rogers RO 4230 substrate with a height of 0.762 mm.

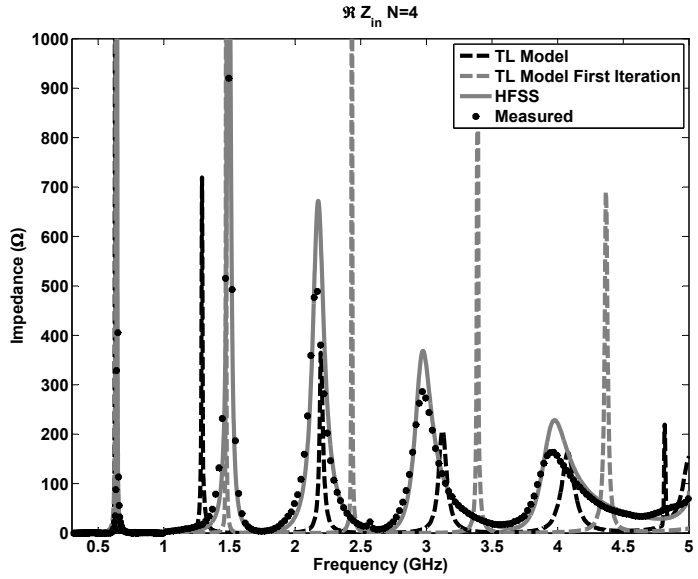

(a)

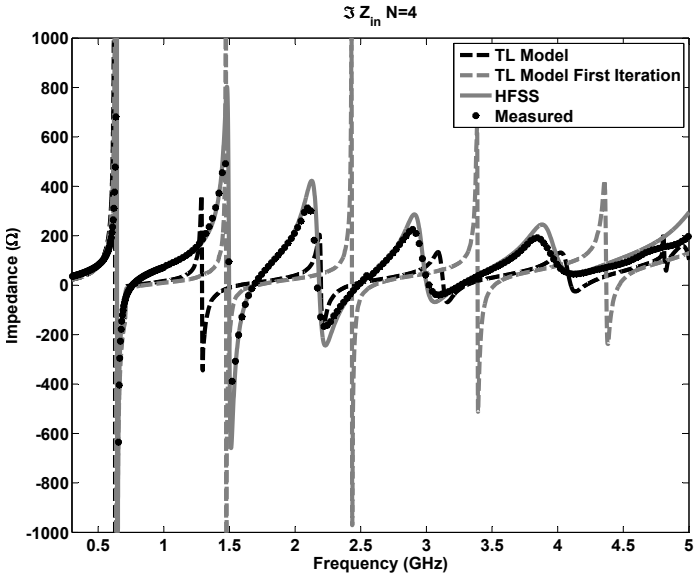

(b)

Figure 7.9: Measured, simulated, and both transmission line model results of impedances of end-loaded slot antennas for N=4, s=1.1 mm. (a) Real part and (b) Imaginary part of input impedance of miniaturized slot antenna constructed using Rogers RO 4230 substrate with a height of 0.762 mm.

impedance response with a much lower bandwidth than the measured results.

7.5 Conclusion and Future Work

The transmission line model for the Archimedean spiral structure accurately predicts the resonant frequencies of the highly coupled multi-line transmission line configuration without using difficult-to-determine multi-line transmission line characteristics. In the future, work will be pursued to add a compensation mechanism to account for the power coupled in the multi-line configuration to more accurately describe the magnitude of the response of the spiral. The model discussed in this chapter for the Archimedean spiral slot structure drastically reduces the time required for a final design since antenna dimensions can be largely determined outside of a full-wave solver. Only minor changes to the design for tuning are required within a computationally expensive full-wave solver.

CHAPTER 8

RFID ANTENNA DESIGN

8.1 Introduction

A reflecting plane was added to the design of the miniaturized slot antenna. As discussed in Chapter 3, slot antennas with reflectors (second ground plane) often couple energy into a parallel plate mode between the ground plane and the reflecting plane [28, 29, 30]. The parallel plate becomes a cavity with the walls of the substrate appearing as reactive loads to the slot antenna. Instead of attempting to reduce this mode, as the authors did in [28, 29, 30], edge treatments can be used to help this mode escape the substrate. We showed in Chapter 3 that edge serrations can reduce the cavity effect in a parallel plate configuration. This chapter discusses the results of a design when the miniaturization method of adding slotline inductors as loads to a slot antenna is combined with edge serrations to reduce the cavity effect when a reflecting plane is added to a slot antenna. A photograph of a constructed antenna that is discussed in this chapter is shown in Figure 8.1.

8.2 Balun and Measured Feeding Configuration

The slot antenna is a balanced structure and therefore requires a balun between the antenna and the coaxial cable feeding it. A quarter wave bazooka balun was constructed and characterized. The common-mode-rejection ratio (CMRR) was measured using the method outlined in [31] and is shown for the constructed balun in Figure 8.2. As outlined in [31], the CMRR was measured

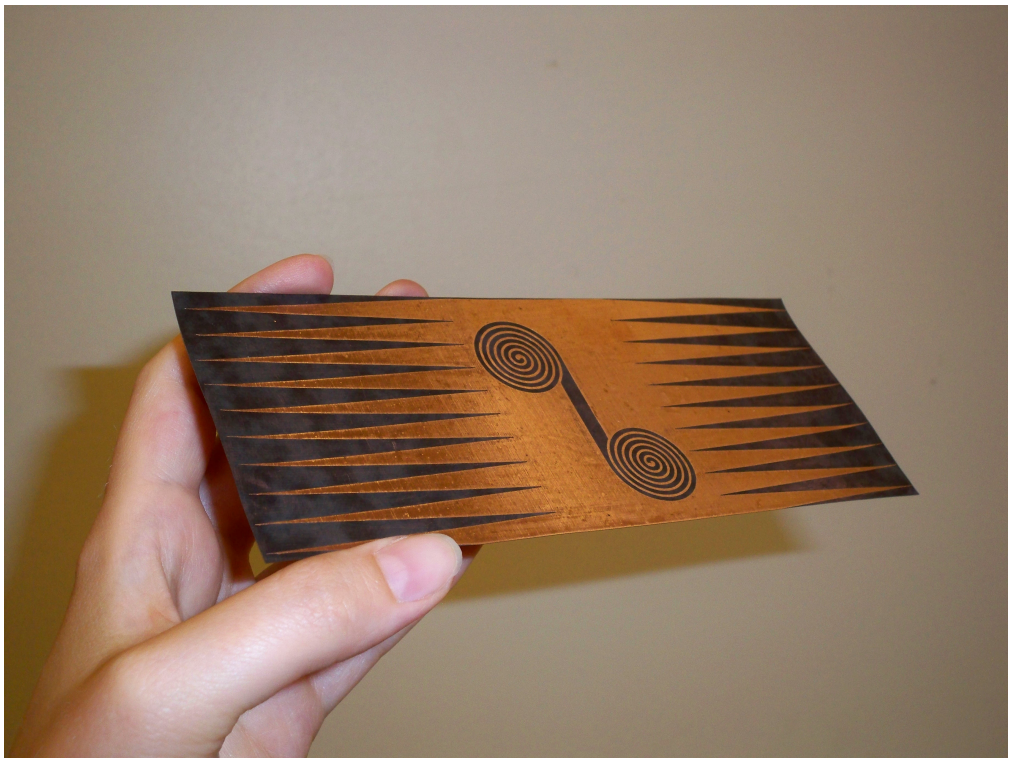

Figure 8.1: Photograph of miniaturized slot antenna with edge serrations and reflecting plane in isometric view.

using a jig as shown in Figure 8.3. The twin lead of the balun is soldered to the twin lead of the jig. The two pieces of semi-rigid coaxial cable share a ground. Therefore, the measurement of the transmission coefficient for each piece of semi-rigid coax can be used to obtain the CMRR. As can be seen in the figure, the CMRR is sufficiently large in the frequency range of interest for this antenna to balance the feeding currents and suppress all significant cable currents.

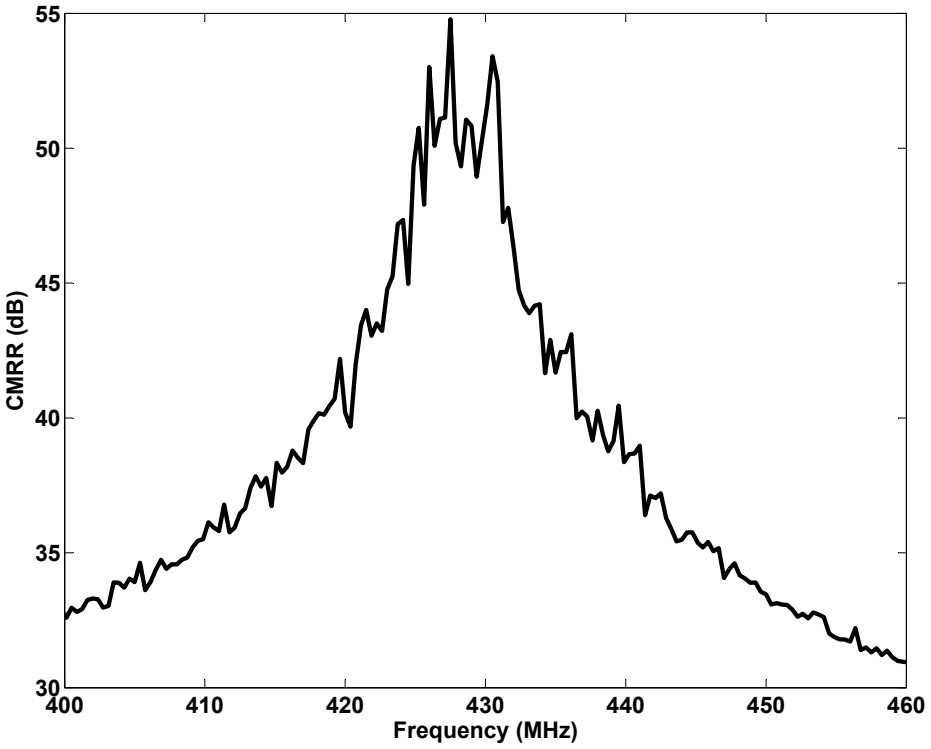

Figure 8.2: Common-mode-mejection ratio (CMRR) of the quarter-wave bazooka balun constructed to ensure feeding of the RFID antenna with balanced currents.

Figures 8.4, 8.5, and 8.6 show the miniaturized slot antenna with a reflecting plane fed using the bazooka balun. The antenna is fed from the back through a small, rectangular hole in the reflecting plane. The addition of the small hole does not appreciably change the behavior of the antenna. Two small holes are

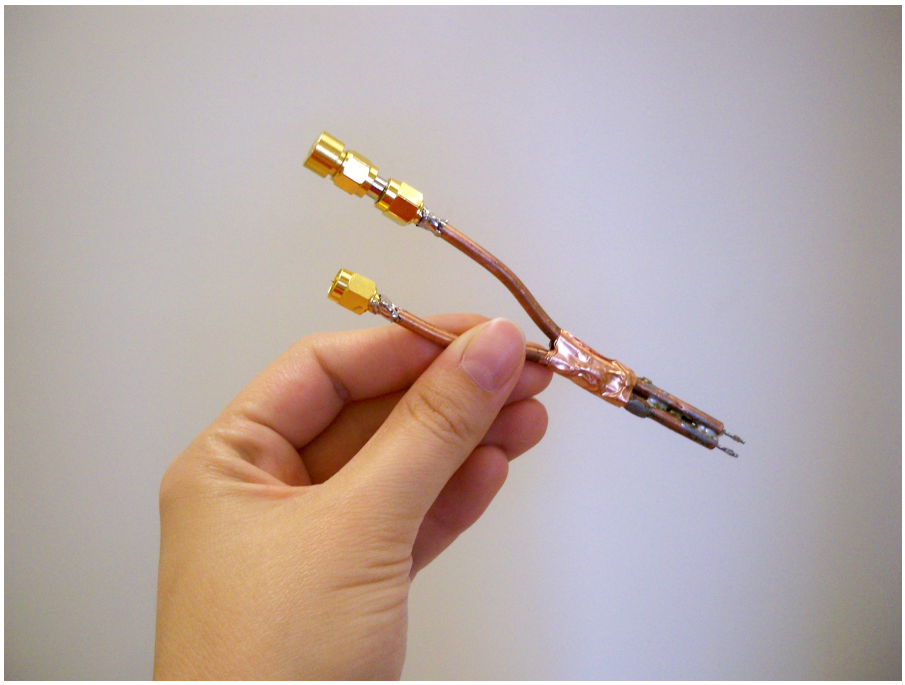

Figure 8.3: Photograph of jig used to measure common-mode-rejection ratio (CMRR) for balun.

also made through the substrate, through which the twin leads of the balun are fed and then soldered to the antenna.

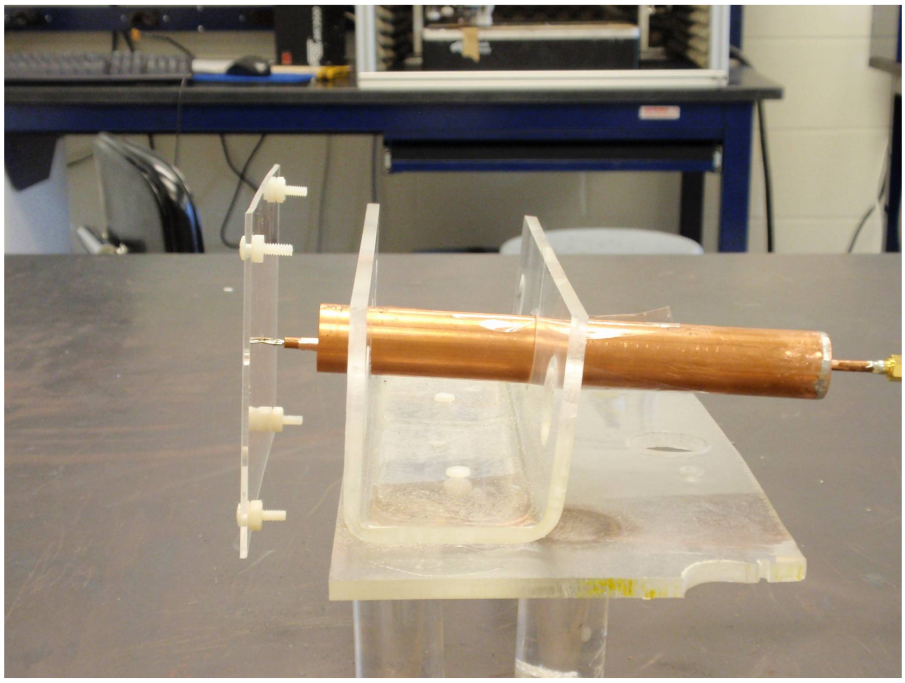

Figure 8.4: Photograph of antenna fed using balun.

8.3 Impedance Tuning Capability

Four antennas were designed to operate near 433 MHz for impedances ranging from 50 to 1500 Ω. The miniaturized slot antenna design presents a wide tuning range due to many of its characteristics. As the height of the substrate is increased, the range of possible impedances increases. For very thin antennas, the maximum impedance that can be achieved is capped by the conductor and dielectric losses; as the losses increase the bandwidth increases. Figure 8.7 displays how the miniaturized slot antenna can be designed to match many different impedances. In Figure 8.7, the VSWR for all four antennas is plotted against the real part of the source impedance.

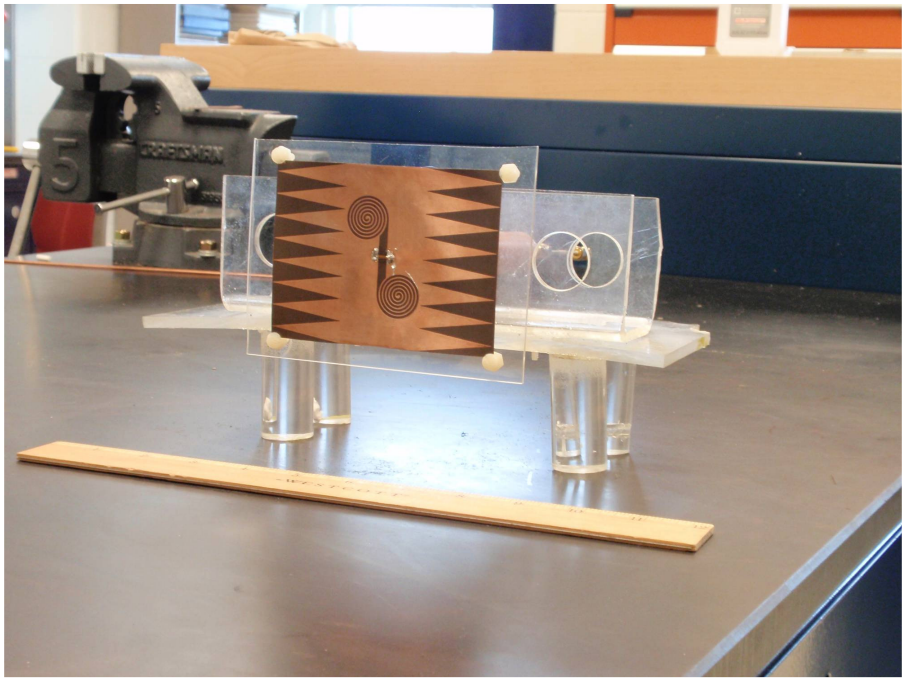

Figure 8.5: Photograph of antenna fed with balun in front view.

8.4 50 Ω Antenna Design and Measurements

A miniaturized slot antenna with a reflecting plane and edge serrations was designed for an input impedance of 50 Ω at 433 MHz. Most RFID chips have much lower output impedances. However, 50 Ω was chosen for the antenna impedance for this case to enable measurements with standard 50 Ω microwave equipment. The substrate was RT Duroid 5880 with a height of 0.147 mm to fit within a "peel-and-stick" form factor. The simulation results along with the measured impedance for the constructed antenna are shown in Figure 8.8. As can be seen in the figure, the measured results agree well with the predicted impedance from simulation. The measured results do deviate slightly from the predictions from simulation, with a frequency shift of approximately 2 MHz, as shown in the figure, as a small rotation. The measured impedance was extracted by de-embedding the results to the end of the balun and accounting for inductance encountered in the twin lead probes by using the formula for the inductance of a wire shown in Section 5.1.2.

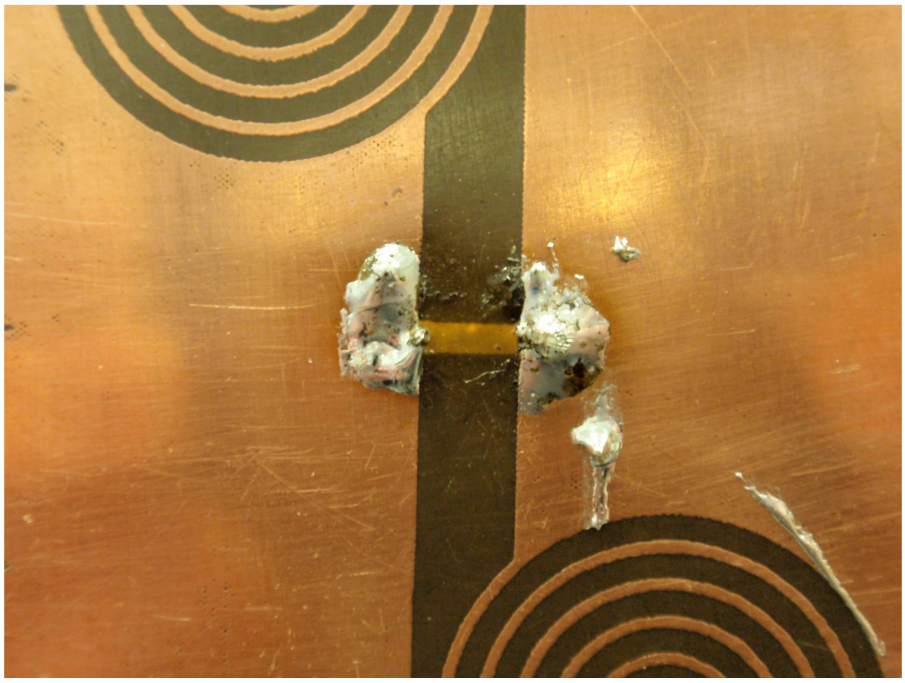

Figure 8.6: Photograph of antenna fed with the balun zoomed in at the feed. The box between the solder bumps is a result of the rectangle etched on the backplane.

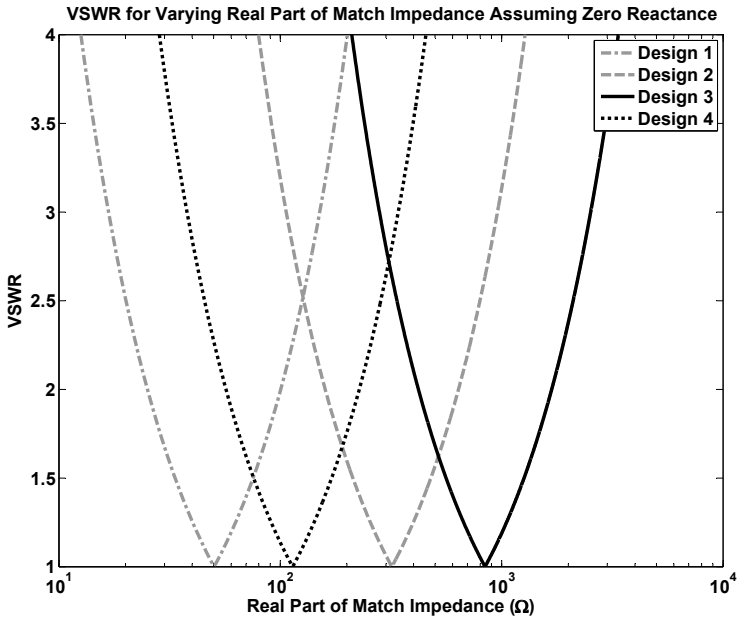

Figure 8.7: The impedance space that can be matched with the miniaturized slot antenna backed by a reflecting plane - results are simulated.

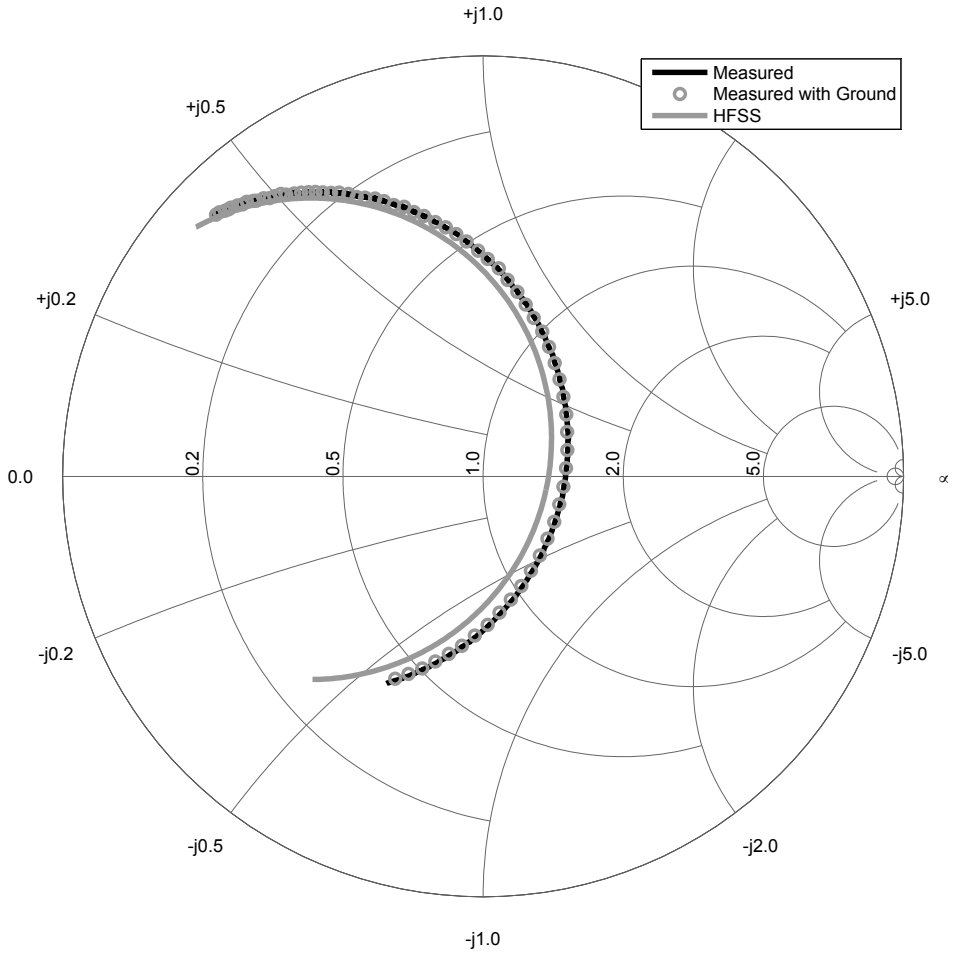

Figure 8.8: Smith chart showing the impedance characteristics of both the measured and simulated placement-insensitive RFID antenna.

The impedance of the antenna was also measured when the antenna was attached to a large metallic ground plane. The dimensions for the ground plane were 46 by 61 cm or (0.66 λ by 0.88 λ). This measured impedance is also shown in Figure 8.8 and, as can be seen in the figure, the ground plane has no effect on the impedance of the antenna.

The radiation patterns of the antenna were measured. The orientation of the antenna for radiation patterns is shown in Figure 8.9 and the radiation patterns are shown in Figures 8.10 and 8.11. The radiation patterns are in terms of realized gain for the antenna, which includes both efficiency and impedance mismatch losses. The maximum gain for both measured and simulated results is approximately -30 dB for both polarizations and cut planes. The radiation pattern in three dimensions is shown in Figure 8.12. When viewed in three dimensions, the antenna radiation pattern is omnidirectional with the null located along the angled axis of the antenna with the spiral inductors. The measured patterns agree relatively well with the simulations. There is a slight increase in directivity for the measured radiation patterns that can likely be attributed to the presence of a balun in the backplane of the antenna. There is also a small angular misalignment between the measurements and simulation that can be attributed to pointing error between the receive horn and the antenna-under-test.

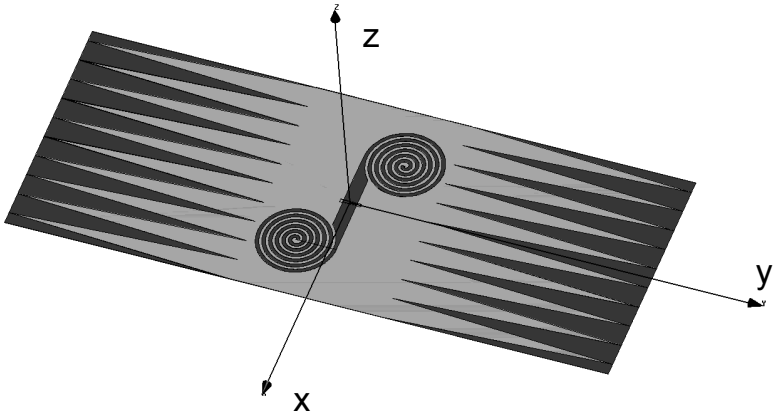

Figure 8.9: Miniaturized slot antenna with edge serrations and reflecting plane in isometric view.

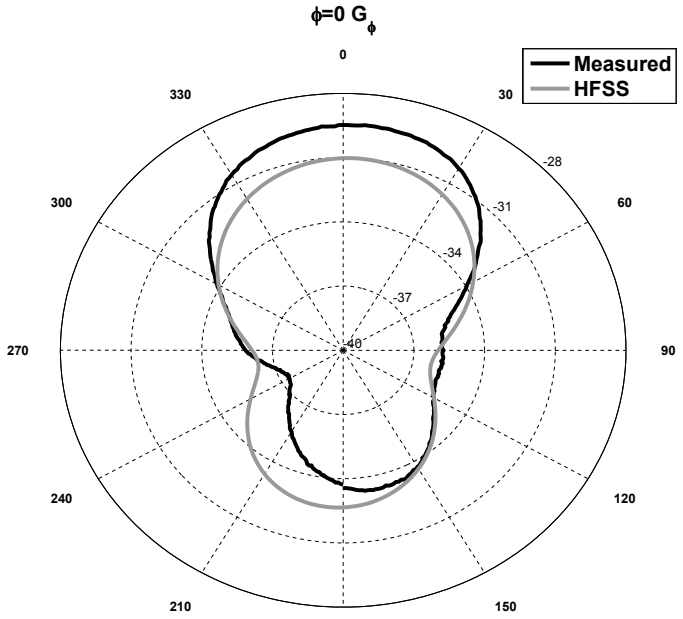

(a)

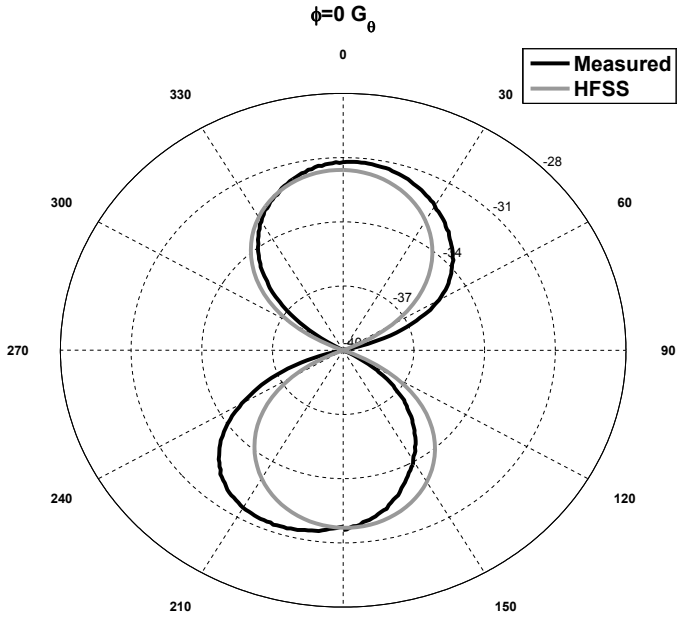

(b)

Figure 8.10: Radiation patterns of miniaturized slot antenna with reflecting plane and edge serrations showing both simulated and measured realized gain for (a) G_ϕ in the $\phi = 0$ plane and (b) G_θ in the $\phi = 0$ plane.

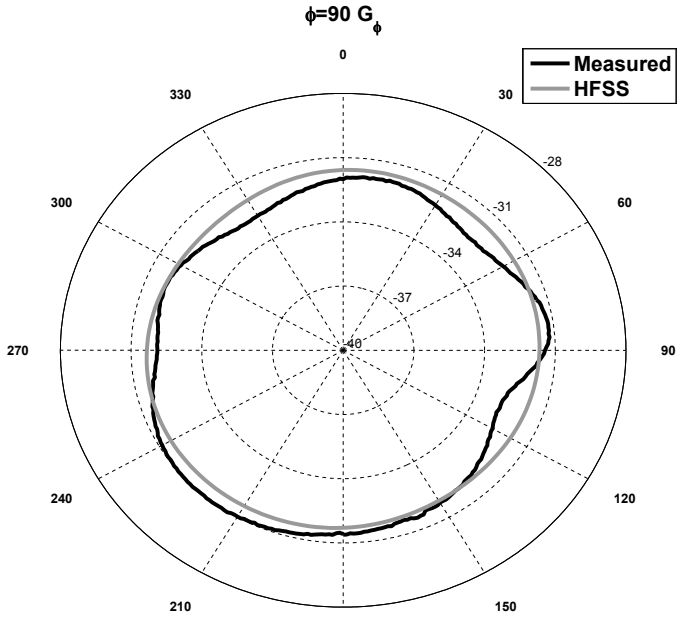

(a)

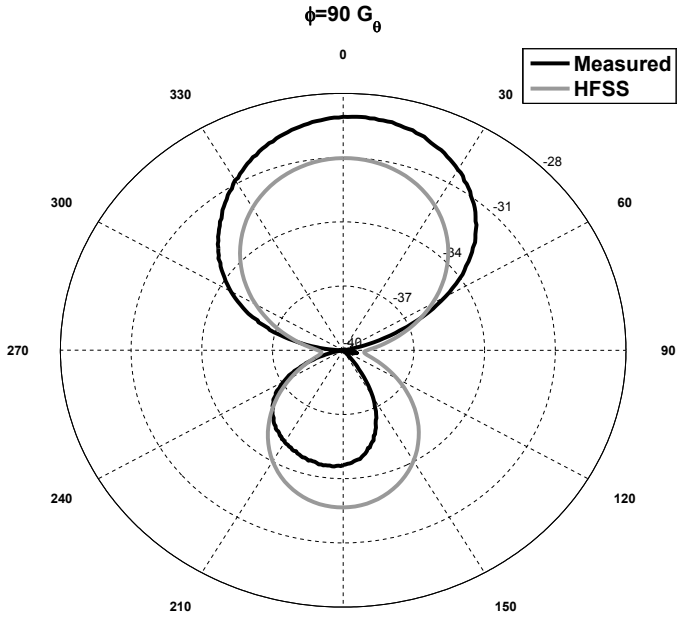

(b)

Figure 8.11: Radiation patterns of miniaturized slot antenna with reflecting plane and edge serrations showing both simulated and measured realized gain for (a) G_ϕ in the $\phi = 90^o$ plane and (b) G_θ in the $\phi = 90^o$ plane.

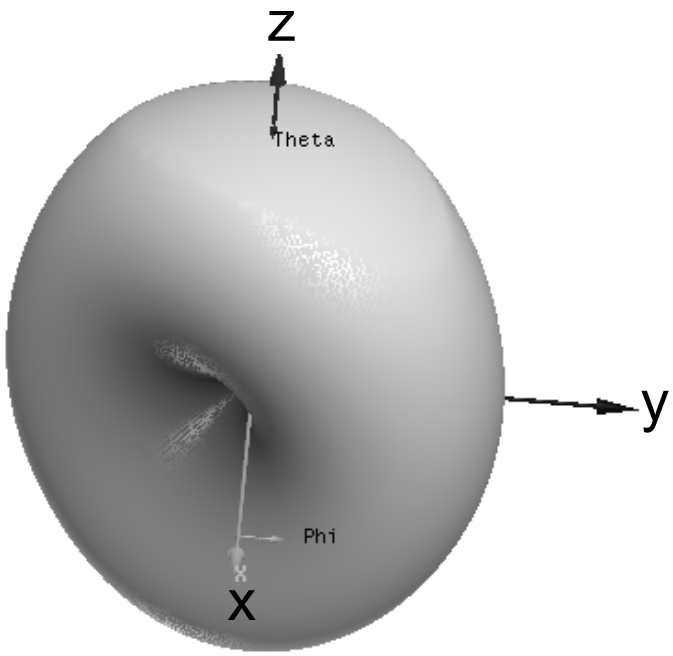

Figure 8.12: Three-dimensional radiation pattern of the total gain of the miniaturized slot antenna with reflecting plane and edge serrations.

The radiation patterns of the antenna were also taken when the antenna was backed by a large ground plane. The same ground plane was used to measure radiation patterns as was used to measure the effect on impedance. These radiation patterns are shown in Figure 8.13 with the same orientation for the antenna as was shown in Figure 8.9. As can be seen in the figure, the large ground plane attached to the antenna makes the antenna radiation more directional. The maximum gain for the antenna is seen in the $\phi = 0^o$ cut plane and in the ϕ polarization at -22.4 dB. The maximum measured gain in the $\phi = 90^0$ cut plane is slightly smaller due to the fact that the ground plane backing the antenna was not square and was not rotated with the antenna when the radiation patterns were taken; a smaller extra ground plane yields less of an increase in gain. The increase in gain due to the addition of a second ground plane is to be expected since the added ground plane both directs the antenna radiation and provides a structure for the antenna to couple into, providing another radiation mechanism.

8.5 Realized Gain Comparison

The effect of the substrate height on efficiency, and therefore on realized gain, was investigated in simulation. The results of this study are shown in Table 8.1. As can be seen in the table, the realized gain improves as the height of the substrate is increased. As discussed earlier, the magnitude of the impedance also increases with the height of the substrate. The realized gains reported for the miniaturized slot antenna with the reflecting plane are low, compared to a standard half-wavelength resonant antenna, so they are compared to an edge fed microstrip patch antenna of identical size. As can be seen in the table, and as one would expect, the realized gains of the two types of antennas are comparable when an impedance mismatch factor is not included. However, since the antennas are electrically small, the impedance of the edge fed microstrip patch antenna is very small and would require an impedance transformer to match to any used source impedance. The geometry of the miniaturized slot

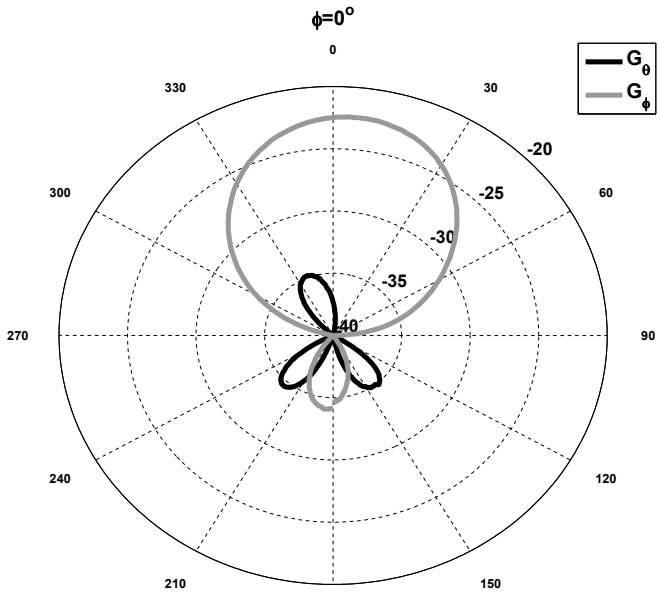

(a)

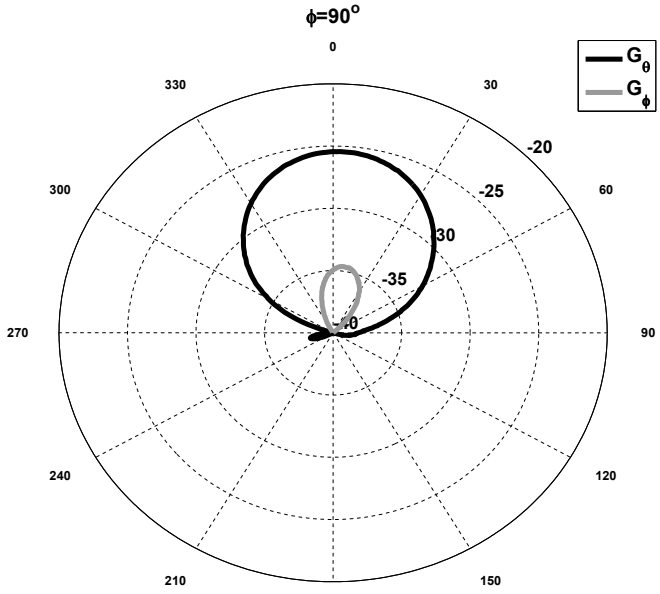

(b)

Figure 8.13: Radiation patterns of miniaturized slot antenna with reflecting plane and edge serrations attached to a metallic ground plane showing measured realized gain for G_ϕ and G_θ in the (a) $\phi = 0$ plane, (b) $\phi = 90^o$ plane.

Table 8.1: The effect of height on efficiency for (a) miniaturized slot antenna and (b) edge-fed microstrip patch antenna. Operation at 433 MHz.

(a)

Miniaturized Slot								
h (mm)	Lgp (mm)	Wgp (mm)	Z Real	Z Imaginary	Gain (dBi)	Assumed Source Impedance	IGammaI	Realized Gain (dBi)
0.147	175	70	54.70	0.46	-29.31	50	0.05	-29.32
0.381	192	60	290.34	-11.22	-19.32	300	0.03	-19.32
0.762	176	65	872.64	-105.22	-16.74	900	0.06	-16.76

(b)

Edge Fed Microstrip Patch								
h (mm)	Lgp (mm)	Wgp (mm)	Z Real	Z Imaginary	Gain (dBi)	Assumed Source Impedance	IGammaI	Realized Gain (dBi)
0.147	175	70	0.06	1.65	-24.69	50	1.00	-47.59
0.381	192	60	0.13	6.64	-16.39	50	0.99	-36.36
0.762	176	65	0.16	16.43	-15.42	50	0.99	-34.88

antenna with a reflecting plane and edge serrations imparts many opportunities for impedance tuning. All of the antennas designed for this work were designed for maximum impedance for the given substrate height by choosing the inductor dimensions to be identical at both ends of the slot. To tune the impedance down to a smaller magnitude, the inductors could be chosen to be non-identical with one inductor presenting a much larger inductance than the other. The serration dimensions for each antenna were also necessarily different due to the change of substrate height.

For further comparison, a straight copper ribbon dipole over a ground plane of size 175 and 70 mm in length and width, respectively, was analyzed in HFSS for three separation distances between the dipole and a ground plane. The width of the dipole was 1 mm and the length was 175 mm. The realized gain of the dipole was found to be -88 dBi, -82.4 dBi, -77.6 dBi for separation distances of the dipole from the ground plane of 0.147 mm, 0.381 mm, and 0.762 mm, respectively.

8.6 Conclusions and Future Work

An antenna suitable for a "peel-and-stick" RFID system for non-electromagnetically transparent objects was developed. The impedance characteristics of this antenna are unaffected by the presence of a large ground plane. The presence of a ground plane also improves the realized gain of the antenna by directing the radiation and providing a secondary radiating structure. It is known that the antenna must be coupling into the second ground plane as a radiating structure from the measured realized gain. When the antenna is radiating in free space the realized gain is approximately -30 dBi and when the antenna is backed by the second ground plane the realized gain is -22.4 dB. This is greater than the 3 dB difference typically encountered when an antenna is backed by a suitably spaced ground plane, implying that the antenna is in fact coupling into the second ground plane as a secondary radiating structure.

CHAPTER 9

DUAL BAND MINIATURIZED SLOT ANTENNA WITH REFLECTING PLANE AND RADIAL EDGE SERRATIONS

9.1 Introduction

The miniaturization method chosen, loading the slot antenna with slotline inductors, inherently offers the possibility of a multi-band antenna due to the distributed nature of the loads. A dual-band design was pursued in both the UHF and X-band and is detailed in this chapter.

9.2 Preliminary Design and Results

The multiband behavior of the antenna was explored and a dual-band antenna design was pursued for both UHF and X-band. More specifically, the antenna designed operates at both 433 MHz and 9.8 GHz. Radial serrations were used as an edge treatment for the dual-band design. It was found that the radial serrations were more effective than the edge serrations on only two edges of a rectangular parallel plate at X-band. This is likely due to the Archimedean spiral slot structure exciting a radial wavefront. In the UHF band, the parallel plate mode is largely excited by the central slot in one plane. In X-band, the spiral structure begins to excite the parallel plate mode, thus requiring a different treatment to address the mitigation of this mode. The antenna design is shown in Figure 9.1. The height of the antenna is 0.381 mm or 15 mil. The diameter of the antenna is 165 mm.

The dual-band antenna was analyzed in simulation. A Smith chart showing the simulated common impedance behavior of the antenna for both UHF and

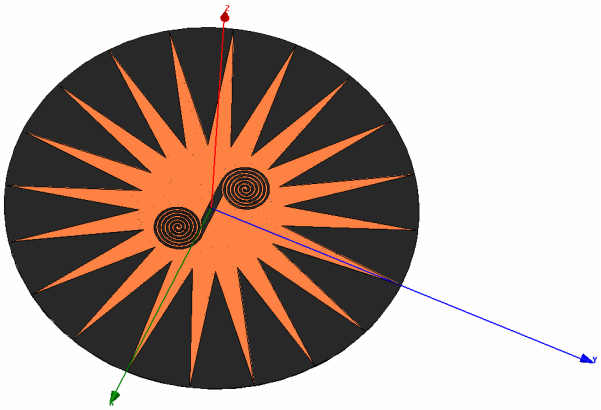

Figure 9.1: Miniaturized dual-band slot antenna with radial serrations.

X-band is shown in Figure 9.2. The simulated realized gain for the antenna in the UHF band (433 MHz) is shown in Figure 9.3 and for X-band (9.85 GHz) is shown in Figure 9.4. As should be expected, the gain is much greater for the antenna in X-band. The antenna is 0.24λ in diameter at 433 MHz and 5.46λ in diameter at 9.85 GHz.

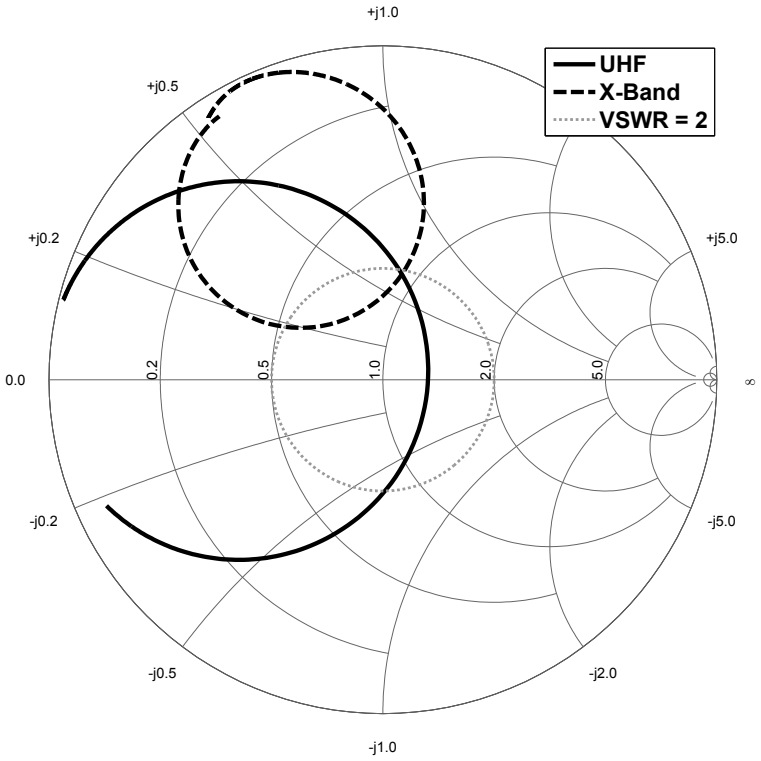

Figure 9.2: Smith chart showing common impedance bandwidth for antenna in both UHF and X-band.

9.3 Conclusions

A dual-band antenna that operates in the extremely widely spaced bands of UHF and X-band was designed. As part of future work, another dual-band design for this antenna will be pursued in the commercially used UHF RFID frequencies of 433 and 915 MHz.

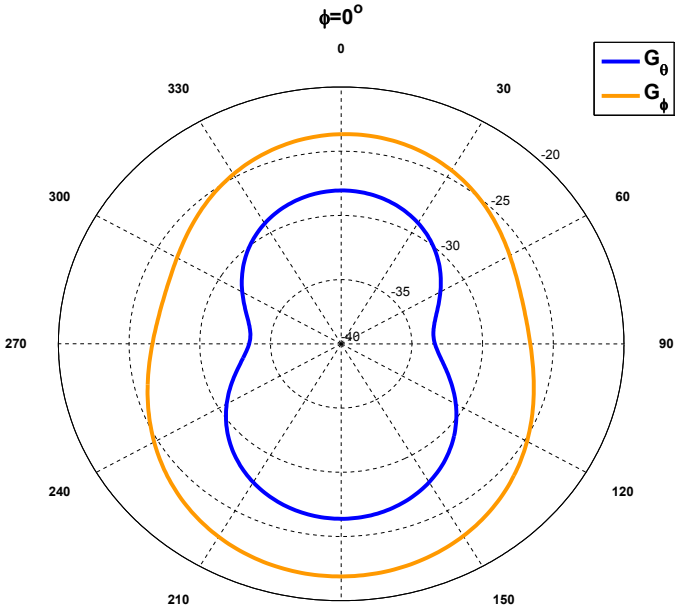

(a)

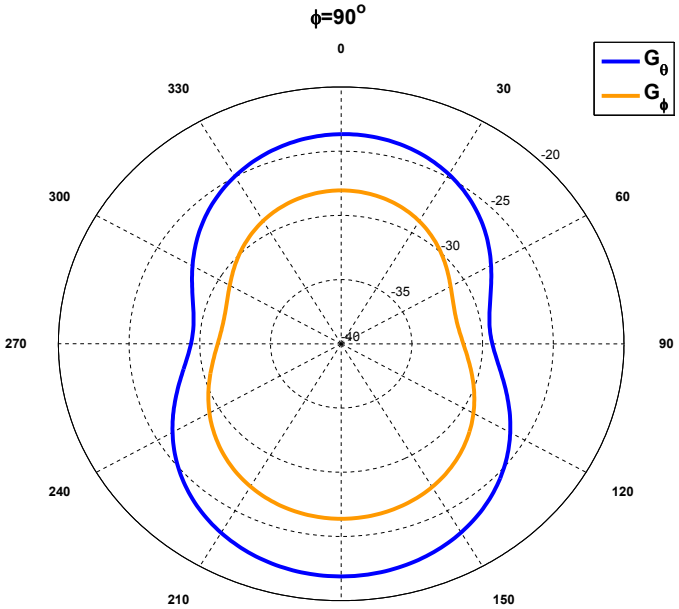

(b)

Figure 9.3: Absolute gain of miniaturized slot antenna with reflecting plane and radial serrations at 433 MHz for (a) $\phi = 0^o$ plane, (b) $\phi = 90^o$ plane.

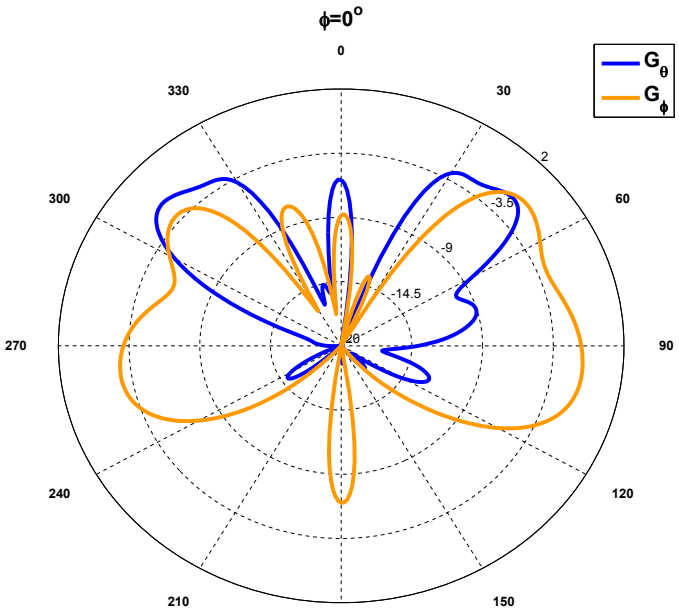

(a)

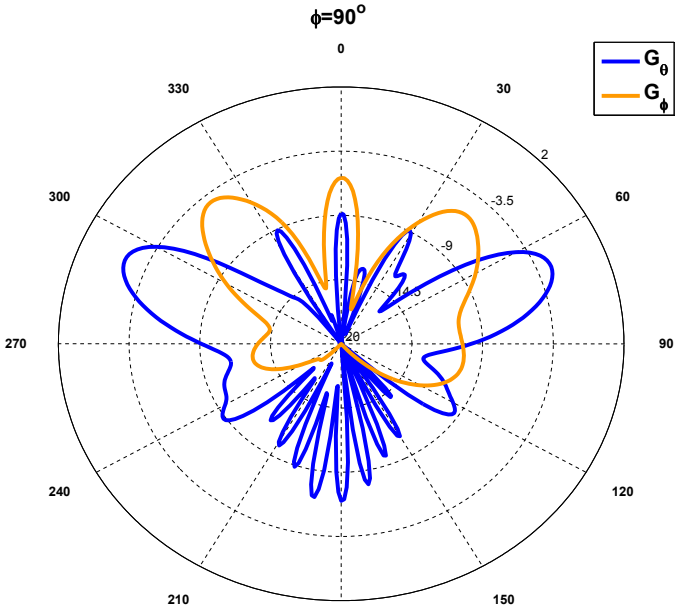

(b)

Figure 9.4: Absolute gain of miniaturized slot antenna with reflecting plane and radial serrations in 9.85 GHz for (a) $\phi = 0^o$ plane,(b) $\phi = 90^o$ plane.

CHAPTER 10

CONCLUSIONS AND FUTURE WORK

10.1 Conclusions

Current RFID antennas rely heavily on dipole antenna designs. The dipole has been shown to be a fundamentally flawed choice for a placement insensitive antenna. The following discusses the three major problems that were addressed to enable the use of slot antennas for "peel-and-stick" RFID antennas for non-electromagnetically transparent objects.

Problem 1: Miniaturization Technique

A traditional straight half-wavelength slot antenna would be too large for an RFID antenna at commonly used RFID frequencies. We investigated loading the slot antenna to reduce its size. By end-loading the slot, the total size of the slot can be greatly reduced. If the slot antenna is correctly loaded for a particular frequency, the input impedance seen at the feed point is the same for the full-sized or loaded slot. If an effective length of less than a half-wavelength is desired for the slot, the loads should be inductive. A slotline inductor provides an easily integratable inductance for the slot antenna and was used for the present antenna design. Loading the slot with a slotline inductor also provides the ability to make the antenna multi-band since the impedance of the inductor changes with frequency.

Major contributions in antenna design:

- Electrically small
- Easily fabricated miniaturization method using standard lithography
- Impedance tuning using variable size loads

- Multi-band due to distributed nature of loads

Problem 2: Placement Insensitivity

To ensure that the performance of the miniaturized slot antenna is independent of the material to which it is attached, a reflecting plane was added to the design. However, slot antennas with closely spaced reflectors often couple energy into a parallel plate mode between the ground plane and the reflecting plane. The parallel plate becomes a cavity with the walls appearing as reactive loads to the slot antenna. We showed that edge serrations can reduce the cavity effect in a parallel plate configuration, making a slot antenna with edge treatments a viable design for environment-independent peel-and-stick applications.

Major contributions:

- Enable placement of slot antenna in extreme proximity to metallic plane
- Eliminate cavity effect in parallel plate structures

Problem 3: Design Methodology

Many current RFID antennas lack a coherent design methodology, rendering the current designs useless outside of specific applications. For this research to be broadly applicable, transmission line models were pursued to aid in the design process. Transmission line models for a rectangular and circular slotline inductor are presented as well as a model describing edge serrations on the ground plane in a parallel plate configuration. Each of these models is useful in and of itself and were combined in this research to present a design methodology for placement insensitive peel-and-stick RFID antennas. With the discussed design methodology, different antennas can be designed for many different frequency bands and applications within RFID and any other application that requires an antenna that fits within a thin form-factor.

Major Contributions:

Design models provided for

- Rectangular spiral slot
- Archimedean spiral slot
- Edge serrations on parallel plate

- Slot antenna - electrically large
- Slot antenna - miniaturized using end-loading

Multiple placement insensitive miniaturized slot antennas with edge serrations were designed for RFID systems with widely varying impedances, including a 50 Ω system operating in the 433 MHz band. The 50 Ω antenna was constructed and shown through measurements to have an impedance behavior truly independent of the material properties of the object to which it is attached. The absolute gain of this antenna is shown to be 30 dB better than a typical antenna with the same form factor. In conclusion, the miniaturized slot antenna with edge serrations provides a revolutionary change to the types of objects that can be tracked using peel-and-stick RFID antennas and the method used to design the antennas used for these applications.

10.2 Future Work

Future work will pursue a dual-band design for 433 and 915 MHz - the two most often used frequency bands for RFID. Work will also be pursued toward a transmission line model for a slot placed over a reflecting plane. Additionally, work will be pursued toward adding radiation effects to the transmission line models for serrations.

APPENDIX A

DERIVATION OF POWER RADIATED

The derivation of the power radiated by the slot antenna begins by assuming the electric field in the slot is as defined in Chapter 4 as

$$E_a = \frac{V(z)}{w_a} = \frac{-V_0}{w_a} \frac{(\sinh(\gamma(\frac{La}{2} - |x|)))}{\sinh(\gamma \frac{L_a}{2})} \hat{y} \tag{A.1}$$

and as shown in Figure A.1. Using the equivalence principle, this electric field can be converted into a magnetic current [13]:

$$M = -2\hat{z} \times E_a = -2\frac{V_0}{w_a} \frac{\sinh(\gamma(\frac{L_a}{2} - |x|))}{\sinh(\gamma \frac{L_a}{2})} \hat{x} \tag{A.2}$$

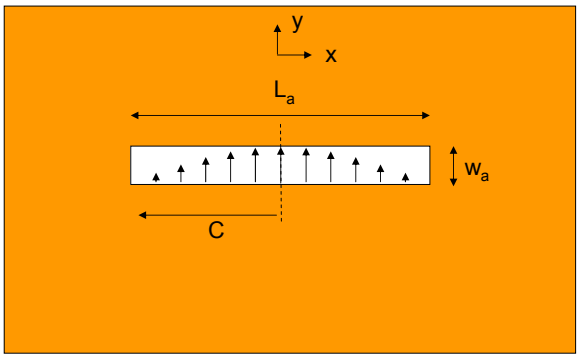

Figure A.1: Depiction of slot with first mode of electric field.

The far-field electric fields are approximated by the following equations [13]:

$$E_\theta \approx \frac{-jke^{-jkr}}{4\pi r}(L_\phi + \eta N_\theta) \tag{A.3}$$

$$E_\phi \approx \frac{+jke^{-jkr}}{4\pi r}(L_\theta - \eta N_\phi) \tag{A.4}$$

where L_θ and L_ϕ are [13]:

$$L_\theta = \iint_S (M_x \cos(\theta)\cos(\phi) + M_y \cos(\theta)\sin(\phi) - M_z \sin(\theta))e^{+jkr'\cos(\psi)}dS' \tag{A.5}$$

$$L_\phi = \iint_S (-M_x \sin(\phi) + M_y \cos(\phi))e^{+jkr'\cos(\psi)}dS' \tag{A.6}$$

N_θ and N_ϕ will be zero for this slot antenna analysis method since they are functions of electric current, which is zero for this configuration. For the aperture configuration depicted in Fig. A.1, $r'\cos(\psi)$ is [13]

$$r'\cos(\psi) = x'\sin(\theta)\cos(\phi) + y'\sin(\theta)\sin(\phi) \tag{A.7}$$

Substituting the magnetic current and $r'\cos(\psi)$ into the equation for L_θ and L_ϕ,

$$L_\theta = \iint_S \frac{-2V_0}{w_a}\frac{\sinh(\gamma(\frac{L_a}{2} - |x|))}{\sinh(\gamma\frac{L_a}{2})}\cos(\theta)\cos(\phi) \tag{A.8}$$
$$* e^{+jk(x'\sin(\theta)\cos(\phi)+y'\sin(\theta)\sin(\phi)}dx'dy'$$

$$L_\phi = \iint_S [\frac{2V_0}{w_a}\frac{\sinh(\gamma(\frac{L_a}{2} - |x|))}{\sinh(\gamma\frac{L_a}{2})}\sin(\phi)]e^{+jk(x'\sin(\theta)\cos(\phi)+y'\sin(\theta)\sin(\phi)}dx'dy' \tag{A.9}$$

Adding in the bounds and expanding the integrals,

$$L_\theta = -2V_0 \frac{\cos(\theta)\cos(\phi)}{w_a \sinh(\gamma \frac{L_a}{2})} \int_{\frac{-w_a}{2}}^{\frac{w_a}{2}} e^{jky' \sin(\theta)\sin(\phi)} dy' \\ * \int_{\frac{-L_a}{2}}^{\frac{L_a}{2}} \sinh(\gamma(\frac{L_a}{2} - |x|)) e^{jkx' \sin(\theta)\cos(\phi)} dx' \tag{A.10}$$

$$L_\phi = 2V_0 \frac{\sin(\phi)}{w_a \sinh(\gamma \frac{L_a}{2})} \int_{\frac{-w_a}{2}}^{\frac{w_a}{2}} e^{jky' \sin(\theta)\sin(\phi)} dy' \\ * \int_{\frac{-L_a}{2}}^{\frac{L_a}{2}} \sinh(\gamma(\frac{L_a}{2} - |x|)) e^{jkx' \sin(\theta)\cos(\phi)} dx' \tag{A.11}$$

Evaluating the integral in y',

$$L_\theta = -2V_0 \frac{\cos(\theta)\cos(\phi)}{w_a \sinh(\gamma \frac{L_a}{2})} \frac{\sin(\frac{kw_a}{2}\sin(\theta)\sin(\phi))w_a}{k\frac{w_a}{2}\sin(\theta)\sin(\phi)} \\ * \int_{\frac{-L_a}{2}}^{\frac{L_a}{2}} \sinh(\gamma(\frac{L_a}{2} - |x|)) e^{jkx' \sin(\theta)\cos(\phi)} dx' \tag{A.12}$$

$$L_\phi = 2V_0 \frac{\sin(\phi)}{w_a \sinh(\gamma \frac{L_a}{2})} \frac{\sin(\frac{kw_a}{2}\sin(\theta)\sin(\phi))w_a}{k\frac{w_a}{2}\sin(\theta)\sin(\phi)} \\ * \int_{\frac{-L_a}{2}}^{\frac{L_a}{2}} \sinh(\gamma(\frac{L_a}{2} - |x|)) e^{jkx' \sin(\theta)\cos(\phi)} dx' \tag{A.13}$$

Using the variable substitutions of

$$g = k \sin(\theta)\sin(\phi) \tag{A.14}$$

and

$$w = k \sin(\theta)\cos(\phi) \tag{A.15}$$

then L_θ and L_ϕ simplify to the following equations:

$$L_\theta = -2V_0 \frac{\cos(\theta)\cos(\phi)}{w_a \sinh(\gamma\frac{L_a}{2})} \frac{\sin(\frac{w_a}{2}g)w_a}{\frac{w_a}{2}g} \int_{-\frac{L_a}{2}}^{\frac{L_a}{2}} \sinh(\gamma(\frac{L_a}{2} - |x|))e^{jx'w}dx' \quad \text{(A.16)}$$

$$L_\phi = 2V_0 \frac{\sin(\phi)}{w_a \sinh(\gamma\frac{L_a}{2})} \frac{\sin(\frac{w_a}{2}g)w_a}{\frac{w_a}{2}g} \int_{-\frac{L_a}{2}}^{\frac{L_a}{2}} \sinh(\gamma(\frac{L_a}{2} - |x|))e^{jx'w}dx' \quad \text{(A.17)}$$

To evaluate the integral of the absolute value of x, the integral must be broken up into two parts as shown below:

$$\begin{aligned}\int_{-\frac{L_a}{2}}^{\frac{L_a}{2}} \sinh(\gamma(\frac{L_a}{2} - |x|))e^{jx'w}dx' = &\int_{-\frac{L_a}{2}}^{0} \sinh(\gamma(\frac{L_a}{2} + x'))e^{jx'w}dx' \\ &+ \int_{0}^{\frac{L_a}{2}} \sinh(\gamma(\frac{L_a}{2} - x'))e^{jx'w}dx'\end{aligned} \quad \text{(A.18)}$$

To evaluate the integral for x' less than zero, the hyperbolic sine function must be expanded as

$$\sinh\Big(\gamma\big(\frac{L_a}{2} + x'\big)\Big) = \frac{e^{\gamma(\frac{L_a}{2}+x')} - e^{-\gamma(\frac{L_a}{2}+x')}}{2} \quad \text{(A.19)}$$

Multiplying by $e^{jx'w}$,

$$\sinh\Big(\gamma\big(\frac{L_a}{2} + x'\big)\Big)e^{jx'w} = \frac{e^{\gamma(\frac{L_a}{2}+x')}e^{jx'w}}{2} - \frac{e^{-\gamma(\frac{L_a}{2}+x')}e^{jx'w}}{2} \quad \text{(A.20)}$$

Expanding the previous equation,

$$\sinh\Big(\gamma\big(\frac{L_a}{2} + x'\big)\Big)e^{jx'w} = \frac{e^{\gamma\frac{L_a}{2}}e^{\gamma x'}e^{jx'w}}{2} - \frac{e^{-\gamma\frac{L_a}{2}}e^{-\gamma x'}e^{jx'w}}{2} \quad \text{(A.21)}$$

Factoring out x',

$$\sinh\Big(\gamma\big(\frac{L_a}{2} + x'\big)\Big)e^{jx'w} = \frac{e^{\gamma\frac{L_a}{2}}e^{x'(\gamma+jw)}}{2} - \frac{e^{-\gamma\frac{L_a}{2}}e^{x'(jw-\gamma)}}{2} \quad \text{(A.22)}$$

Putting the expanded hyperbolic sine function into the integral,

$$\int_{-\frac{L_a}{2}}^{0} \sinh(\gamma(\frac{L_a}{2}+x'))e^{jx'w}dx' = \int_{-\frac{L_a}{2}}^{0} \frac{e^{\gamma\frac{L_a}{2}}e^{x'(\gamma+jw)}}{2} - \int_{-\frac{L_a}{2}}^{0} \frac{e^{-\gamma\frac{L_a}{2}}e^{x'(jw-\gamma)}}{2} \tag{A.23}$$

Evaluating the integral,

$$\int_{-\frac{L_a}{2}}^{0} \sinh(\gamma(\frac{L_a}{2}+x'))e^{jx'w}dx' = \frac{e^{\gamma\frac{L_a}{2}}}{2}\Big[\frac{e^{x'(\gamma+jw)}}{\gamma+jw}\Big]_{-\frac{L_a}{2}}^{0} - \frac{e^{-\gamma\frac{L_a}{2}}}{2}\Big[\frac{e^{x'(jw-\gamma)}}{jw-\gamma}\Big]_{-\frac{L_a}{2}}^{0} \tag{A.24}$$

Evaluating the bounds of the integral,

$$\begin{aligned}\int_{-\frac{L_a}{2}}^{0} \sinh(\gamma(\frac{L_a}{2}+x'))e^{jx'w}dx' =& \frac{e^{\gamma\frac{L_a}{2}}}{2}\Big[\frac{1-e^{-\frac{L_a}{2}(\gamma+jw)}}{\gamma+jw}\Big] \\ &- \frac{e^{-\gamma\frac{L_a}{2}}}{2}\Big[\frac{1-e^{-\frac{L_a}{2}(jw-\gamma)}}{jw-\gamma}\Big]\end{aligned} \tag{A.25}$$

Expanding the exponentials,

$$\begin{aligned}\int_{-\frac{L_a}{2}}^{0} \sinh(\gamma(\frac{L_a}{2}+x'))e^{jx'w}dx' =& \frac{e^{\gamma\frac{L_a}{2}}}{2(\gamma+jw)}\Big[1-e^{-\frac{L_a}{2}\gamma}e^{-\frac{L_a}{2}jw)}\Big] \\ &- \frac{e^{-\gamma\frac{L_a}{2}}}{2(jw-\gamma)}\Big[1-e^{-\frac{L_a}{2}jw}e^{+\frac{L_a}{2}\gamma}\Big]\end{aligned} \tag{A.26}$$

Multiplying through by $e^{\gamma\frac{L_a}{2}}$,

$$\begin{aligned}\int_{-\frac{L_a}{2}}^{0} \sinh(\gamma(\frac{L_a}{2}+x'))e^{jx'w}dx' =& \frac{1}{2(\gamma+jw)}\Big[e^{\gamma\frac{L_a}{2}} - e^{-\frac{L_a}{2}jw}\Big] \\ &- \frac{1}{2(jw-\gamma)}\Big[e^{-\gamma\frac{L_a}{2}} - e^{-\frac{L_a}{2}jw}\Big]\end{aligned} \tag{A.27}$$

Expanding,

$$\int_{-\frac{L_a}{2}}^{0} \sinh(\gamma(\frac{L_a}{2}+x'))e^{jx'w}dx' = \frac{e^{\gamma\frac{L_a}{2}}}{2(\gamma+jw)} - \frac{e^{-\gamma\frac{L_a}{2}}}{2(jw-\gamma)} - \frac{e^{-\frac{L_a}{2}jw}}{2(\gamma+jw)} + \frac{e^{-\frac{L_a}{2}jw}}{2(jw-\gamma)} \tag{A.28}$$

Expanding further,

$$\int_{-\frac{L_a}{2}}^{0} \sinh(\gamma(\frac{L_a}{2}+x'))e^{jx'w}dx' = \frac{e^{\gamma\frac{L_a}{2}}(jw-\gamma)}{-2(\gamma^2+w^2)} - \frac{e^{-\gamma\frac{L_a}{2}}(\gamma+jw)}{-2(\gamma^2+w^2)} - \frac{e^{-\frac{L_a}{2}jw}(jw-\gamma)}{-2(\gamma^2+w^2)} + \frac{e^{-\frac{L_a}{2}jw}(\gamma+jw)}{-2(\gamma^2+w^2)} \tag{A.29}$$

Canceling terms,

$$\int_{-\frac{L_a}{2}}^{0} \sinh(\gamma(\frac{L_a}{2}+x'))e^{jx'w}dx' = \frac{-1}{2(\gamma^2+w^2)}\Big[-\gamma e^{\gamma\frac{L_a}{2}} - \gamma e^{-\gamma\frac{L_a}{2}} + \gamma e^{-\frac{L_a}{2}jw} + \gamma e^{-\frac{L_a}{2}jw}\Big] \tag{A.30}$$

Combining exponentials to form hyperbolic cosine,

$$\int_{-\frac{L_a}{2}}^{0} \sinh(\gamma(\frac{L_a}{2}+x'))e^{jx'w}dx' = \frac{-1}{2(\gamma^2+w^2)}\Big[-2\gamma\cosh(\gamma\frac{L_a}{2}) + 2\gamma e^{-\frac{L_a}{2}jw}\Big] \tag{A.31}$$

Factoring -2γ out,

$$\int_{-\frac{L_a}{2}}^{0} \sinh(\gamma(\frac{L_a}{2}+x'))e^{jx'w}dx' = \frac{\gamma}{(\gamma^2+w^2)}\Big[\cosh(\gamma\frac{L_a}{2}) - e^{-\frac{L_a}{2}jw}\Big] \tag{A.32}$$

The same operations as above now need to be performed to evaluate the integral for x' greater than zero. Expanding hyperbolic sine into exponentials,

$$\sinh\Big(\gamma\big(\frac{L_a}{2}-x'\big)\Big) = \frac{e^{\gamma(\frac{L_a}{2}-x')} - e^{-\gamma(\frac{L_a}{2}-x')}}{2} \tag{A.33}$$

Multiplying by $e^{jx'w}$,

$$\sinh(\gamma(\frac{L_a}{2}-x'))e^{jx'w} = \frac{e^{\gamma(\frac{L_a}{2}-x')}e^{jx'w}}{2} - \frac{e^{-\gamma(\frac{L_a}{2}-x')}e^{jx'w}}{2} \tag{A.34}$$

Expanding the previous equation,

$$\sinh(\gamma(\frac{L_a}{2}-x'))e^{jx'w} = \frac{e^{\gamma\frac{L_a}{2}}e^{-\gamma x'}e^{jx'w}}{2} - \frac{e^{-\gamma\frac{L_a}{2}}e^{+\gamma x'}e^{jx'w}}{2} \tag{A.35}$$

Factoring out x',

$$\sinh(\gamma(\frac{L_a}{2}-x'))e^{jx'w} = \frac{e^{\gamma\frac{L_a}{2}}e^{x'(jw-\gamma)}}{2} - \frac{e^{-\gamma\frac{L_a}{2}}e^{x'(jw+\gamma)}}{2} \tag{A.36}$$

Putting the expanded hyperbolic sine function into the integral,

$$\int_0^{\frac{L_a}{2}} \sinh(\gamma(\frac{L_a}{2}-x'))e^{jx'w}dx' = \int_0^{\frac{L_a}{2}} \frac{e^{\gamma\frac{L_a}{2}}e^{x'(jw-\gamma)}}{2} - \int_0^{\frac{L_a}{2}} \frac{e^{-\gamma\frac{L_a}{2}}e^{x'(jw+\gamma)}}{2} \tag{A.37}$$

Evaluating the integral,

$$\int_0^{\frac{L_a}{2}} \sinh(\gamma(\frac{L_a}{2}-x'))e^{jx'w}dx' = \frac{e^{\gamma\frac{L_a}{2}}}{2}\Big[\frac{e^{x'(jw-\gamma)}}{jw-\gamma}\Big]_0^{\frac{L_a}{2}} - \frac{e^{-\gamma\frac{L_a}{2}}}{2}\Big[\frac{e^{x'(jw+\gamma)}}{jw+\gamma}\Big]_0^{\frac{L_a}{2}} \tag{A.38}$$

Evaluating the bounds of the integral,

$$\begin{aligned}\int_0^{\frac{L_a}{2}} \sinh(\gamma(\frac{L_a}{2}-x'))e^{jx'w}dx' =& \frac{e^{\gamma\frac{L_a}{2}}}{2}\Big[\frac{e^{\frac{L_a}{2}(jw-\gamma)}-1}{jw-\gamma}\Big] \\ &- \frac{e^{-\gamma\frac{L_a}{2}}}{2}\Big[\frac{e^{\frac{L_a}{2}(jw+\gamma)}-1}{jw+\gamma}\Big]\end{aligned} \tag{A.39}$$

Expanding the exponentials,

$$\begin{aligned}\int_0^{\frac{L_a}{2}} \sinh(\gamma(\frac{L_a}{2}-x'))e^{jx'w}dx' =& \frac{e^{\gamma\frac{L_a}{2}}}{2(jw-\gamma)}\Big[e^{-\frac{L_a}{2}\gamma}e^{-\frac{L_a}{2}jw}-1\Big] \\ &-\frac{e^{-\gamma\frac{L_a}{2}}}{2(jw+\gamma)}\Big[e^{\frac{L_a}{2}jw}e^{+\frac{L_a}{2}\gamma}-1\Big]\end{aligned} \tag{A.40}$$

Multiplying through by $e^{\gamma\frac{L_a}{2}}$,

$$\int_0^{\frac{L_a}{2}} \sinh(\gamma(\frac{L_a}{2}-x'))e^{jx'w}dx' = \frac{1}{2(jw-\gamma)}\Big[e^{-\frac{L_a}{2}jw} - e^{\gamma\frac{L_a}{2}}\Big] - \frac{1}{2(jw+\gamma)}\Big[e^{\frac{L_a}{2}jw} - e^{-\gamma\frac{L_a}{2}}\Big] \tag{A.41}$$

Expanding,

$$\int_0^{\frac{L_a}{2}} \sinh(\gamma(\frac{L_a}{2}+x))e^{jx'w}dx' = \frac{e^{\gamma\frac{L_a}{2}}}{2(jw-\gamma)} + \frac{e^{-\gamma\frac{L_a}{2}}}{2(jw+\gamma)} + \frac{e^{-\frac{L_a}{2}jw}}{2(jw-\gamma)} + \frac{e^{-\frac{L_a}{2}jw}}{2(jw+\gamma)} \tag{A.42}$$

Expanding further,

$$\int_0^{\frac{L_a}{2}} \sinh(\gamma(\frac{L_a}{2}-x'))e^{jx'w}dx' = \frac{e^{\gamma\frac{L_a}{2}}(\gamma+jw)}{-2(\gamma^2+w^2)} - \frac{e^{-\gamma\frac{L_a}{2}}(\gamma+jw)}{-2(\gamma^2+w^2)} - \frac{e^{-\frac{L_a}{2}jw}(jw-\gamma)}{-2(\gamma^2+w^2)} + \frac{e^{-\frac{L_a}{2}jw}(\gamma+jw)}{-2(\gamma^2+w^2)} \tag{A.43}$$

Canceling terms,

$$\int_0^{\frac{L_a}{2}} \sinh(\gamma(\frac{L_a}{2}-x'))e^{jx'w}dx' = \frac{-1}{2(\gamma^2+w^2)}\Big[-\gamma e^{\gamma\frac{L_a}{2}} - \gamma e^{-\gamma\frac{L_a}{2}} + \gamma e^{\frac{L_a}{2}jw} + \gamma e^{\frac{L_a}{2}jw}\Big] \tag{A.44}$$

Combining exponentials to form hyperbolic cosine,

$$\int_0^{\frac{L_a}{2}} \sinh(\gamma(\frac{L_a}{2}-x'))e^{jx'w}dx' = \frac{-1}{2(\gamma^2+w^2)}\Big[-2\gamma\cosh(\gamma\frac{L_a}{2}) + 2\gamma e^{\frac{L_a}{2}jw}\Big] \tag{A.45}$$

Factoring -2γ out,

$$\int_0^{\frac{L_a}{2}} \sinh(\gamma(\frac{L_a}{2}-x'))e^{jx'w}dx' = \frac{\gamma}{(\gamma^2+w^2)}\Big[\cosh(\gamma\frac{L_a}{2}) - e^{\gamma\frac{L_a}{2}jw}\Big] \tag{A.46}$$

The original integral can be evaluated as

$$\int_{-\frac{L_a}{2}}^{\frac{L_a}{2}} \sinh(\gamma(\frac{L_a}{2}-|x|))e^{jx'w}dx' = \frac{\gamma}{(\gamma^2+w^2)}\Big[\cosh(\gamma\frac{L_a}{2}) - e^{\frac{L_a}{2}jw}\Big] + \frac{\gamma}{(\gamma^2+w^2)}\Big[\cosh(\gamma\frac{L_a}{2}) - e^{-\frac{L_a}{2}jw}\Big] \quad \text{(A.47)}$$

Combining,

$$\int_{-\frac{L_a}{2}}^{\frac{L_a}{2}} \sinh(\gamma(\frac{L_a}{2}-|x|))e^{jx'w}dx' = \frac{\gamma}{(\gamma^2+w^2)}\Big[2\cosh(\gamma\frac{L_a}{2}) - e^{\frac{L_a}{2}jw} - e^{-\frac{L_a}{2}jw}\Big] \quad \text{(A.48)}$$

The exponentials combine to form a cosine as

$$\int_{-\frac{L_a}{2}}^{\frac{L_a}{2}} \sinh(\gamma(\frac{L_a}{2}-|x|))e^{jx'w}dx' = \frac{2\gamma}{(\gamma^2+w^2)}\Big[\cosh(\gamma\frac{L_a}{2}) - \cos(w\frac{L_a}{2})\Big] \quad \text{(A.49)}$$

L_θ and L_ϕ are then evaluated as

$$L_\theta = -2V_0\frac{\cos(\theta)\cos(\phi)}{w_a\sinh(\gamma\frac{L_a}{2})}\frac{\sin(\frac{w_a}{2}g)w_a}{\frac{w_a}{2}g}\frac{2\gamma}{(\gamma^2+w^2)}\Big[\cosh(\gamma\frac{L_a}{2}) - \cos(w\frac{L_a}{2})\Big] \quad \text{(A.50)}$$

$$L_\phi = 2V_0\frac{\sin(\phi)}{w_a\sinh(\gamma\frac{L_a}{2})}\frac{\sin(\frac{w_a}{2}g)w_a}{\frac{w_a}{2}g}\frac{2\gamma}{(\gamma^2+w^2)}\Big[\cosh(\gamma\frac{L_a}{2}) - \cos(w\frac{L_a}{2})\Big] \quad \text{(A.51)}$$

If we assume that w_a is small relative to a wavelength, then the sinc function dependent on w_a is approximately 1, then L_θ and L_ϕ can be simplified to

$$L_\theta = -2V_0\frac{\cos(\theta)\cos(\phi)}{\sinh(\gamma\frac{L_a}{2})}\frac{2\gamma}{(\gamma^2+w^2)}\Big[\cosh(\gamma\frac{L_a}{2}) - \cos(w\frac{L_a}{2})\Big] \quad \text{(A.52)}$$

$$L_\phi = 2V_0\frac{\sin(\phi)}{\sinh(\gamma\frac{L_a}{2})}\frac{2\gamma}{(\gamma^2+w^2)}\Big[\cosh(\gamma\frac{L_a}{2}) - \cos(w\frac{L_a}{2})\Big] \quad \text{(A.53)}$$

The total power radiated by the slot antenna will be the surface integral of

the Poynting vector as shown below:

$$P_r = \frac{1}{2}\int\int_S \Re(\vec{E} \times \vec{H}^*)dS \tag{A.54}$$

The integrand can be evaluated as

$$\vec{E} \times \vec{H}^* = \frac{|E_\theta|^2}{\eta} + \frac{|E_\phi|^2}{\eta} \tag{A.55}$$

The power radiated is then

$$P_r = \frac{1}{2\eta}\int\int_S \Re(|E_\theta|^2 + |E_\phi|^2)dS \tag{A.56}$$

As defined in Equations A.3 and A.4 the magnitude squared of E_θ and E_ϕ can be approximated as

$$|E_\theta|^2 \approx \frac{|k|^2}{(4\pi r)^2}|L_\phi|^2 \tag{A.57}$$

and

$$|E_\phi|^2 \approx \frac{|k|^2}{(4\pi r)^2}|L_\theta|^2 \tag{A.58}$$

Using the results of L_ϕ and L_θ as defined earlier, the magnitude squared of E_θ and E_ϕ are

$$|E_\theta|^2 = \frac{|k|^2}{(4\pi r)^2}4|V_0|^2\frac{\sin^2(\phi)}{|\sinh(\gamma\frac{L_a}{2})|^2}\frac{4|\gamma|^2}{|\gamma^2+w^2|^2}\left|\cosh(\gamma\frac{L_a}{2}) - \cos(w\frac{L_a}{2})\right|^2 \tag{A.59}$$

and

$$|E_\phi|^2 = \frac{|k|^2}{(4\pi r)^2}4|V_0|^2\frac{\cos^2(\theta)\cos^2(\phi)}{|w_a\sinh(\gamma\frac{L_a}{2})|}\frac{4|\gamma|^2}{|\gamma^2+w^2|^2}\left|\cosh(\gamma\frac{L_a}{2}) - \cos(w\frac{L_a}{2})\right|^2 \tag{A.60}$$

Adding the square magnitudes of E_θ and E_ϕ,

$$|E_\theta|^2 + |E_\phi|^2 = \frac{|k|^2}{(\pi r)^2} \frac{|V_0|^2}{|\sinh(\gamma \frac{L_a}{2})|} [\sin^2(\phi) + \cos^2(\theta)\cos^2(\phi)] \\ * \frac{|\gamma|^2}{|\gamma^2 + w^2|^2} \left| \cosh(\gamma \frac{L_a}{2}) - \cos(w \frac{L_a}{2}) \right|^2 \tag{A.61}$$

The power radiated is

$$P_r = \frac{1}{2\eta} \iint_S \Re(|E_\theta|^2 + |E_\phi|^2) r^2 \sin(\theta) d\theta d\phi \tag{A.62}$$

Putting the expressions for E_θ and E_ϕ into the power radiated integral,

$$P_r = \frac{1}{2\eta} \iint_S \frac{|k|^2}{(\pi)^2} \frac{|V_0|^2}{|\sinh(\gamma \frac{L_a}{2})|} [\sin^2(\phi) + \cos^2(\theta)\cos^2(\phi)] \frac{|\gamma|^2}{|\gamma^2 + w^2|^2} \\ * \left| \cosh(\gamma \frac{L_a}{2}) - \cos(w \frac{L_a}{2}) \right|^2 \sin(\theta) d\theta d\phi \tag{A.63}$$

Canceling terms and placing limits on the integral,

$$P_r = \frac{\zeta}{\eta} \int_0^{\pi} \int_0^{\frac{\pi}{2}} \frac{|k|^2}{(\pi)^2} \frac{|V_0|^2}{|\sinh(\gamma \frac{L_a}{2})|} [\sin^2(\phi) + \cos^2(\theta)\cos^2(\phi)] \\ * \frac{|\gamma|^2}{|\gamma^2 + w^2|^2} \left| \cosh\left(\gamma \frac{L_a}{2}\right) - \cos\left(w \frac{L_a}{2}\right) \right|^2 \sin(\theta) d\theta d\phi \tag{A.64}$$

An extra factor of ζ was added to the front of the integral [12]. This factor is to account for the fact that the slot antenna is radiating into both half-spaces and the derivation assumes it only radiates into the upper half-space. If the slot is placed on a substrate of air, then ζ will be equal to 2. Otherwise,

$$\zeta = 1 + \frac{1}{\sqrt{\epsilon_r}} \tag{A.65}$$

REFERENCES

[1] J. Prothro, G. Durgin, and J. Griffin, "The effects of a metal ground plane on RFID tag antennas," in *IEEE Antennas Propag. Soc. Int. Symp.*, 2006, pp. 3241–3244.

[2] J. Griffin, G. Durgin, A. Haldi, and B. Kippelen, "RF tag antenna performance on various materials using radio link budgets," *IEEE Antennas Wireless Propag. Lett.*, vol. 5, p. 247, 2006.

[3] S. Best, "Improving the performance properties of a dipole element closely spaced to a PEC ground plane," *IEEE Antennas Wireless Prop. Lett.*, vol. 3, pp. 359–363, 2004.

[4] C. Cho, H. Choo, and I. Park, "Design of planar RFID tag antenna for metallic objects," *Electron. Lett.*, vol. 44, no. 3, pp. 175–177, 2008.

[5] H. Son, J. Yeo, G. Choi, and C. Pyo, "A low-cost, wideband antenna for passive RFID tags mountable on metallic surfaces," in *IEEE Antennas Propag. Soc. Int. Symp.*, 2006, pp. 1019–1022.

[6] Ansys, "High Frequency Structure Simulator," Canonsburg, PA, ver. 12.

[7] T. Lee and W. Burnside, "Performance trade-off between serrated edge and blended rolled edge compact range reflectors," *IEEE Trans. Antennas Propag.*, vol. 44, no. 1, pp. 87–96, 1996.

[8] G. Huff and J. Bernhard, "Improvements in the performance of microstrip antennas on finite ground planes through ground plane edge serrations," *IEEE Microw. Wireless Compon. Lett.*, vol. 12, no. 8, pp. 308–310, 2002.

[9] D. Pozar, *Microwave Engineering*, 3rd ed. Hoboken, NJ: John Wiley & Sons, 2005.

[10] R. Jackson, "Simple analytic formulas for the nonlocal field generated by circuit elements in multilayer structures," *IEEE Trans. Microw. Theory Tech.*, vol. 48, no. 11, pp. 1967–1971, 2000.

[11] R. Abhari, G. Eleftheriades, and E. van Deventer-Perkins, "Physics-based CAD models for the analysis of vias in parallel-plate environments," *IEEE Trans. Microw. Theory Tech.*, vol. 49, no. 10, pp. 1697–1707, 2001.

[12] M. Himdi and J. Daniel, "Analysis of printed linear slot antenna using lossy transmission line model," *Electronics Lett.*, vol. 28, no. 6, pp. 598–601, 1992.

[13] C. Balanis, *Antenna Theory: Analysis and Design*, 3rd ed. Hoboken, NJ: John Wiley & Sons, 2005.

[14] S. Cohn, "Slot line on a dielectric substrate," *IEEE Trans. Microw. Theory Tech.*, vol. 17, no. 10, pp. 768–778, 1969.

[15] R. Garg, P. Bhartia, I. Bahl, and A. Ittipiboon, *Microstrip Antenna Design Handbook*. Boston, MA: Artech House, 2001.

[16] J. Dyson, "The equiangular spiral antenna," *IRE Trans. Antennas Prop.*, vol. 7, no. 2, pp. 181–187, 1959.

[17] P. Shepherd, "Analysis of square-spiral inductors for use in MMICs," *IEEE Trans. Microw. Theory Tech.*, vol. 34, no. 4, pp. 467–471, 1986.

[18] R. Simons and R. Arora, "Double-slot fin-line structure for millimeter wave applications," in *IEEE Proc.*, vol. 67, 1979, p. 1159.

[19] R. Simons, "Studies on microwave slot-line and integrated fin-line," Ph.D. dissertation, Department of Electrical Engineering, Indian Institute of Technology, New Delhi, 1981.

[20] J. Knorr, "Slot-line transitions," *IEEE Trans. Microw. Theory Tech*, vol. 22, no. 5, pp. 548–554, 1974.

[21] S. Remillard, P. Radzikowski, S. Cordone, D. Applegate, A. Mehrotra, J. Kokales, and A. Abdelmonem, "A closed slot-line resonator filter," *IEEE Microw. Wireless Compon. Letters*, vol. 14, no. 5, pp. 234–236, 2004.

[22] T. Ozdemir, J. Volakis, and M. Nurnberger, "Analysis of thin multioctave cavity-backed slot spiral antennas," *IEE Proc. Microw., Antennas, and Prop.*, vol. 146, no. 6, pp. 447–454, 2002.

[23] R. Mongia, I. Bahl, and P. Bhartia, *RF and Microwave Coupled-Line Circuits.* Boston, MA: Artech House, 1999.

[24] A. Tripathi and V. Tripathi, "A configuration-oriented SPICE model for multiconductor transmission lines in an inhomogeneous medium," *IEEE Trans. Microw. Theory Tech.*, vol. 46, no. 12, pp. 1997–2005, 1998.

[25] S. Franke, *Radio Communication Circuits and Systems.* Class notes for ECE 453, Department of Electrical and Computer Engineering, University of Illinois at Urbana-Champaign, 2008.

[26] J. Bryant, "The first century of microwaves - 1886 to 1986," *IEEE Trans. Microw. Theory Tech.*, vol. 36, no. 5, pp. 830–858, 1988.

[27] R. Azadegan and K. Sarabandi, "A novel approach for miniaturization of slot antennas," *IEEE Trans. Antennas Propag.*, vol. 51, no. 3, pp. 421–429, 2003.

[28] M. Qiu and G. Eleftheriades, "Highly efficient unidirectional twin arc-slot antennas on electrically thin substrates," *IEEE Trans. Antennas Propag.*, vol. 52, no. 1, pp. 53–58, 2004.

[29] J. Kim and J. Yook, "A parallel-plate-mode suppressed meander slot antenna with plated-through-holes," *IEEE Antennas Wireless Propag. Lett.*, vol. 4, pp. 118–120, 2005.

[30] C. Locker, T. Vaupel, and T. Eibert, "Radiation efficient unidirectional low-profile slot antenna elements for X-band application," *IEEE Trans. Antennas Propag.*, vol. 53, no. 8, pp. 2765–2768, 2005.

[31] M. J. Slater, C. M. Schmitz, D. L. Jones, and J. T. Bernhard, "Common mode current effects in electrically small direction of arrival systems," in *Gov. Microcircuit Applications Critical Tech. Conf.*, 2011.